Convection in Stellar Atmospheres

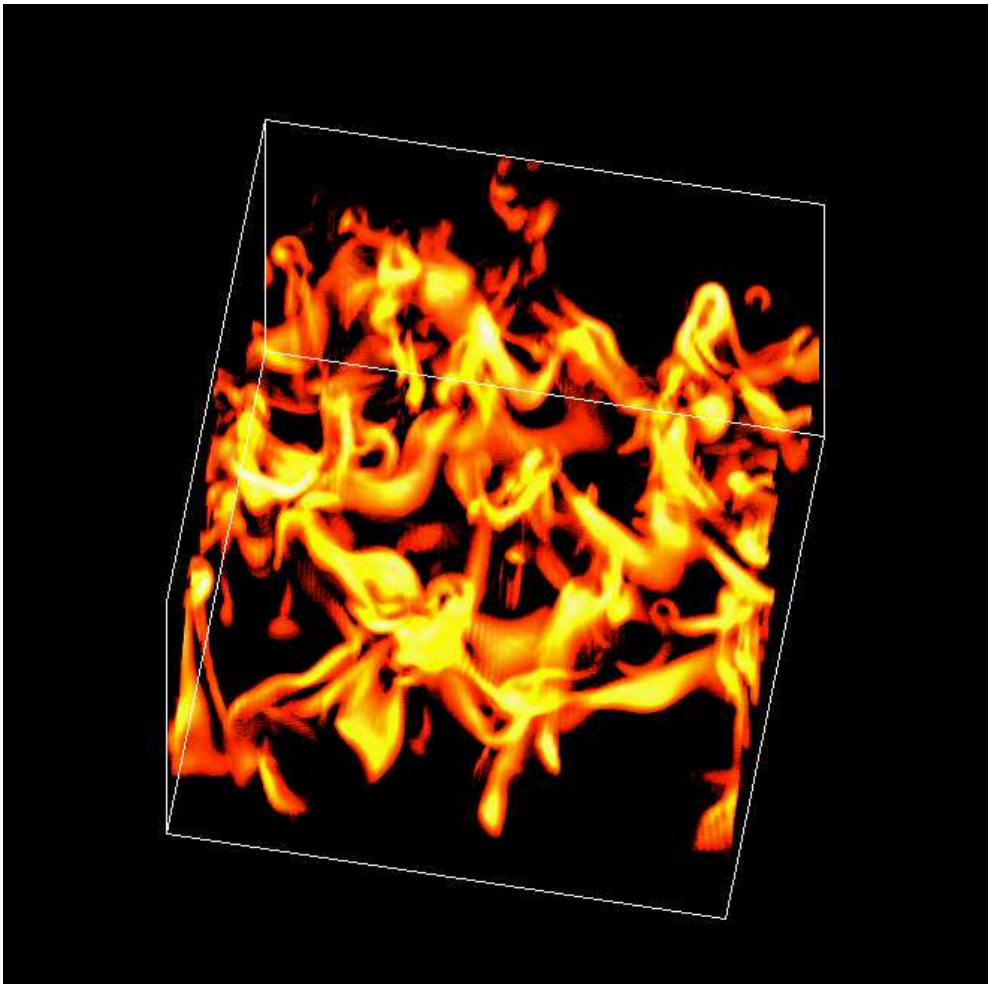

by

Regner Trampedach

Master Thesis in Astrophysics, August 1997
Institute of Physics and Astronomy
Aarhus University

Second edition

Preface

Being an astronomy student, I have frequently encountered questions like how big is the universe, - is it endless, how many stars are there, how old is the universe, does it go on for ever... All those big questions about "life, the universe and everything" (Adams 1989b).

Sitting in the office at the computer, where the most common problem is to understand some computer code written by a guy in the seventies, or to figure out why changing and changing back again do not return your code to its previous state, I do feel pretty far from the above questions, - but there is a connection anyway.

One of the most fundamental tasks of astronomy has always been the determination of distances in the universe — rather important if we want to know what we talk about.

We have now received precise measurements of parallaxes for about 120 000 of the nearest stars, obtained by the HIPPARCOS satellite (Perryman et al. 1997). The parallax method is the only direct method for measuring distances to objects outside the solar system, and this method only works for stars within about 100 pc or 300 light years of the Sun. Going further out, we have to rely on various indirect techniques, most of which depend crucially on knowledge about stellar surfaces and evolution. When observing stars far away, it gets increasingly difficult to obtain spectra with any reasonably resolution, and normally one takes recourse to broad band photometry, observing in 2-5 spectral bands, to get enough photons. From the magnitudes in these colours, one then infers information on the star's physical parameters like effective temperature, $T_{\rm eff}$, surface gravity, g and metallicity Z. The transformation from the observed magnitudes to these physical parameters does, however, depend strongly on our detailed understanding of stellar atmospheres. The latter is addressed in this thesis. More precisely the subject is

> *"Effects of near-surface convection on solar and stellar structure with special emphasis on realistic treatment of the input physics"*

The last line refers to my desire to produce results that can be compared directly with observations.

So even if stars were not interesting in themselves (and I can assure the reader that they are), the cosmologists would at least want to know a few things about stars to answer these questions about — well, in particular "...the universe and everything".

This thesis would not be in your hands if it was not for the assistance of a great number of very helpful people, to whom I am very grateful. I would in particular like to thank Friedrich Kupka for supplying me with copies of Kurucz' line opacities and for discussions on continuous opacities, Edward Gustafsson for sending me a copy of his line opacities, Martin Asplund for sending me his version of some OP-opacities, Colin Rosenthal for reminding me that stars tend to oscillate, Werner Däppen for invaluable help with the MHD-EOS code and fruitful discussions on the EOS and a pleasant stay in L.A., Bob (Robert F.) Stein for discussions, introduction to American folk dancing and a very pleasant stay in Lansing, Michigan, Jesper Schou for taking me to Quandary Peak during my stay in Boulder, Colorado, Thebe Medupe for producing 1D atmosphere models for me, and Sarbani Basu for Moral support during Convex downs. I would also like to thank Poul Erik Nissen, Søren Frandsen, Hans Kjeldsen, Frank Grundahl and Jesper G. Hansen for inspiring discussions on what can actually be observed.

As this thesis work survived two generations of office mates, I'll first thank the old staff: Peter K. Bjørnholt for inventing "The for Long and Impatiently Anticipating Alien IV Resurrection Movieclub", Thomas H. Dall for liking the eminent composer Mike Oldfield and Tina Christensen for donating the invaluable office coffee machine. This work could never have been carried out without coffee. The current crew consist of Jacob F. Pedersen and Jakob J. Larsen who are phycisists and therefore introduced the concept of PC's to the office as well as opened my eyes for the experimental world, and Anders T. Hansen working with Trans-Neptunian objects who showed me that the Ole Römer Observatory (ORO) can actually be used for scientific purposes. And also a warm thanks to the librarians Liv Vego and Dorte H. Flindt, for conjuring up articles based on the most hopeless and ancient references, and to our secretary Anette for always knowing just what you need to know (if it is not about convection!).

I acknowledge UNI-C for the excessive amounts of computer time, without which this thesis would barely consist of this preface, and I acknowledge financial support by the Danish National Research Foundation through its establishment of the Theoretical Astrophysics Center.

And last but not least, I am grateful to my two supervisors: Jørgen Christensen-Dalsgaard and Åke Nordlund, for introducing me to the scientific method and thinking, as well as for the astrophysical community.

My friends and family also deserves a warm thanks for the cheering.

Regner Trampedach

Aarhus, March 18, 2000.

Front cover: The picture is a 3D volume rendering of the amplitude of vorticity of a snapshot of the high resolution solar simulation (*cf.* Sect. 8). The vorticity is scaled to highlight the structure of the motions in the whole depth of the simulation box.

Contents

Preface **I**

Contents **V**

1 Introduction **1**

2 The hydrodynamical foundation **5**
2.1 Hydrodynamics 6
2.2 Diffusion 7
2.2.1 Mixed second- and fourth-order diffusion 8
2.2.2 Quenched diffusion 9
2.3 Boundary Conditions 10
2.3.1 The horizontal boundaries 10
2.3.2 The top boundary 11
2.3.3 The bottom boundary 12
2.4 Solving the Difference Equations 13
2.4.1 Spatial interpolation 13
2.4.2 Spatial derivatives 14
2.4.3 Spatial integration 14
2.4.4 Time stepping 14
2.5 The z-grid 15
2.6 Damping of p-modes 16

3 The atomic physics foundation **19**
3.1 Chemical Mixture 20
3.2 The Equation of State 22
3.2.1 The original EOS 25
3.2.2 The MHD EOS 27
3.2.3 Discussion 29
3.3 The Opacity 31
3.3.1 The bf- and ff-opacity 32
3.3.2 Scattering by Electrons 34
3.3.3 Line opacity 35

3.3.4 The total opacity 42
3.4 The table program 46
3.5 Thermodynamics 48

4 The radiative transfer **51**
4.1 The effect of lines 52
4.2 3D radiative transfer 53
4.3 1D radiative transfer 57
4.4 The Feautrier technique 57

5 Six different stars **59**
5.1 The asteroseismic motivation 61
5.1.1 The Sun 62
5.1.2 The α Cen system 62
5.1.3 η Boo 63
5.1.4 Procyon 64

6 Mean models **65**
6.1 The effect of non-linear fluctuations 65
6.2 Matching with 1-D envelopes 65
6.2.1 The MLT formulation 67
6.2.2 The Sun 69
6.2.3 α Cen A 71
6.2.4 α Cen B 72
6.2.5 η Boo 73
6.2.6 Procyon 74
6.2.7 Star B 75

7 Morphology of convection as observed in the simulations **77**
7.1 Below the surface 77
7.2 Granulation 81
7.2.1 Spectral line asymmetries 81
7.2.2 Granular patterns 81
7.3 Convective overshooting 85
7.4 Comparison with the mixing-length formalism 88
7.5 Comparison with the theory of Lydon, Fox and Sofia 90

8 High-precision solar simulation **95**
8.1 The surface flux 95
8.2 The 1D envelope match 97

9 Future prospects **101**
9.1 Atomic physics 101
9.2 Other stars 101
9.3 Confronting observations 102

10 Conclusion **103**

Bibliography **105**

A Opacity updates **115**

B Scattering by atomic hydrogen **125**

C An IDL[1] interface to the averaged models **129**

D Calibrating the mixing-length with 3D RHD simulations **135**

E On using T-τ relations as outer boundary condition for stellar models **141**

[1] IDL® is a registered trademark of Research Systems Inc., Boulder, Colorado, USA.

Chapter 1

Introduction

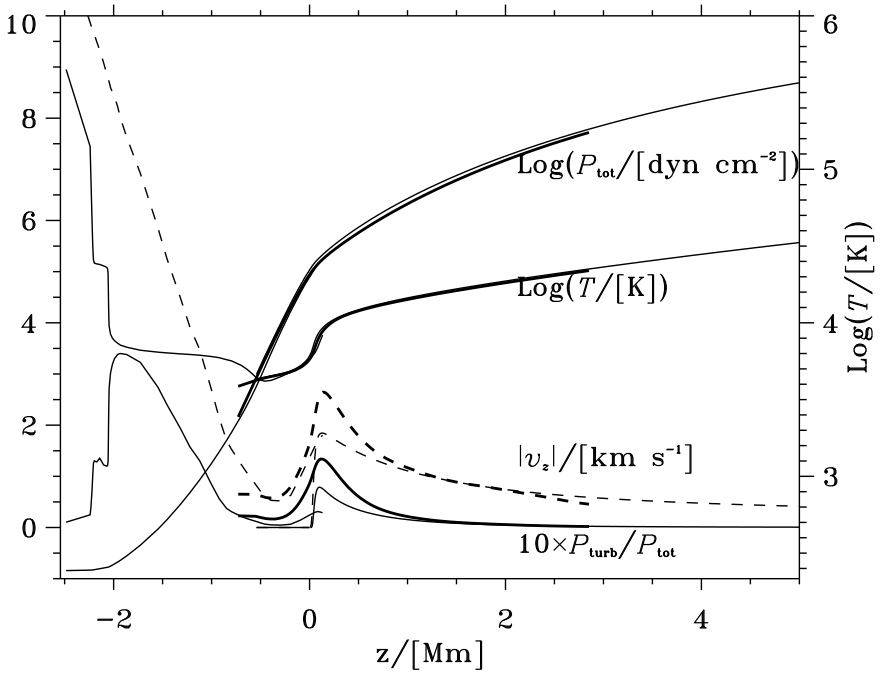

Fig. 1.1: This plot serves to give an overview of the region around the solar atmosphere. It combines a semi empirical chromospheric model (Vernezza et al. 1981) (VAL) with my convection simulations and a conventional 1D-envelope model (Christensen-Dalsgaard & Däppen 1992). The abscissa is a depth scale, so z increases inward in the models. The curves above $z = 0.1$Mm shows the VAL-model, the curves below $z = -0.5$Mm are from the 1D-envelope model, and the thick curves overlapping both, are temporal and horizontal averages of my 3D convection simulation of the Sun.

In Fig. 1.1 I show the region around the photosphere, which I will investigate in this thesis. The investigation is observational in a fairly new sense, in that this thesis is centered around observations of numerical simulations of the coupled thermo-, radiation- and hydro-dynamics around stellar photospheres.

Fig. 1.1 is a combination of three angles of view: The chromospheric model based on observations and extending *down* to the photosphere. The stellar structure model extending *up* to the photosphere, and finally the simulations presented here, that sit right in the photosphere, experiencing the complications from both regions. The agreement between the three different ways of viewing the Sun is surprisingly good. The main difference is that dynamic quantities, such as velocities and turbulent pressure, are underestimated (or missing) in the photospheres of the 1-D models.

The good agreement is very reassuring — we know quite a bit about the Sun, but the disagreement in the photosphere, (fortunately) tells us that there is still work to do. Mainly in the field of 3D and dynamical analysis of photospheres, as addressed with this thesis.

The turbulent motions of gases in the convective parts of stars have always been a problem. And the complications arise in the transition from convective to radiative transport of the energy. In this transition zone, convection gets less efficient and more vigorous gas flows are needed to carry the flux. This affects the hydrostatic equilibrium, by contributing to the vertical momentum balance. It is also the region where the radiation experiences the transition from optically thick to optically thin (diffusion approximation breaks down), resulting in very steep temperature gradients. Combining this with inhomogeneities between warm upflows and cool downdrafts renders this region very hard to treat in 1D models.

My thesis is organized as follows:

- Chapter 2 explains the basic hydrodynamics, as well as gives a rather detailed description of the numerical methods that goes into the hydrodynamical part of the convection code.

- Chapter 3 is a full description of the atomic physics used in the simulations, *i.e.* the thermodynamic part described by the *equation of state* (EOS), and the opaqueness of the plasma — the *opacity*. The high quality atomic physics, is one of the major reasons that we can talk about realistic simulations, and an appreciable amount of my work is spent here.

- Chapter 4 describes the computation of the radiative transfer in the simulations, and this is the other major contributor to the realism of the simulations.

- Chapter 5 is a presentation of the 6 stars I have chosen to make simulations of, as well as reasons for this choice.

- Chapter 7 is the observational part. I show and explain some of the many features of the convection, compare the six stars and compare with other ways of treating convection in stellar model calculations.

- Chapter 6 shows how the simulations can be combined with conventional 1D stellar models to tell something about the whole outer convection zone of the star, rather than just a thin layer at the surface.
- Chapter 8 is a short presentation of a high-resolution simulation of the Sun, intended for future analysis.
- Chapter 9 tells about all the projects that I did not have time to include in this thesis.
- Chapter 10 provides a short summary and conclusions.

Chapter 2

The hydrodynamical foundation

One of the key quantities for describing a hydrodynamical system is the *Reynolds number* (Rott 1990). The Reynolds number, $\mathcal{R} = \mathcal{UL}/\nu$, is the ratio of advective to viscous transport of momentum in a system with kinematic viscosity, ν, a characteristic length scale, $\mathcal{L}$, and typical flow speeds, $\mathcal{U}$. The viscosity of a plasma is approximately $\nu = v_{\rm th}d$, where $v_{\rm th}$ is the thermal speed and d is the average interparticle distance (Kippenhahn & Weigert 1990, chapter 43). From this we see that the Reynolds number for a plasma is just the ratio of macroscopic to microscopic speed$\times$distance-scales. For stellar atmospheres the pressure scale height, H_P is a natural choice for $\mathcal{L}$ (but note that the characteristic horizontal scale, the granular scale of motion is about an order of magnitude larger than the pressure scale height).

A large $\mathcal{R}$ implies that viscosity only influence the the flow directly on a much smaller scale, and that turbulence can develop. Turbulence transports kinetic energy from the macroscopic scales and down to the dissipation scale through a turbulent cascade, whereby large-scale fluctuations break up and form ever smaller turbulent eddies right down to the dissipation scale where the energy is dissipated. Turbulence is, however, not a one way phenomena, from large to small scales, as the amount of energy dissipated on the small scale most likely will influence the large-scale behaviour of the flow. A large gap between the macroscopic and the dissipation scales indicates a potential for turbulence, but whether the granular flow will appear turbulent is also a question of stratification of the flow, as discussed in Sect. 7.2 and Nordlund et al. (1997).

The convection simulations are performed in a plane-parallel geometry, without magnetic fields and with a resolution that corresponds to Reynolds numbers of about, $\mathcal{R} \simeq 40$, which is rather far from the $\mathcal{R} \simeq 10^{13}$ prevailing in stellar atmospheres. This means that these simulations do not resolve all of the possible small-scale structure of the actual stellar atmospheres. If the convection is appreciable turbulent this might be a serious shortcoming of the simulations and this is also the most critical point of the kind of simulations presented here. These low $\mathcal{R}$ simulations do however seem to describe the high $\mathcal{R}$ reality rather well, as will be discussed further in Sect. 7.2.

The rest of this chapter contains a detailed description of the hydrodynamics part of the convection code, and is based largely on Nordlund & Stein (1990), Nordlund (1982), Stein (1989) and a close inspection of the code.

2.1 Hydrodynamics

The basic equations solved in this work are: the equation of mass conservation, often referred to as the continuity equation,

$$\frac{\partial \varrho}{\partial t} = -\boldsymbol{u} \cdot \nabla \varrho - \varrho \nabla \cdot \boldsymbol{u}, \tag{2.1}$$

the equation of momentum conservation, also called the equation of motion,

$$\varrho \frac{\partial \boldsymbol{u}}{\partial t} = -\varrho \boldsymbol{u} \cdot \nabla \boldsymbol{u} + \varrho \boldsymbol{g} - \nabla P_{\rm g}, \tag{2.2}$$

and the equation of energy conservation,

$$\frac{\partial E}{\partial t} = -\nabla \cdot (\boldsymbol{u} E) - P \nabla \cdot \boldsymbol{u} + \varrho (Q_{\rm rad} + Q_{\rm visc}), \tag{2.3}$$

where ϱ is the density, $P_{\rm g}$ the gas pressure, E the internal energy per volume, $\boldsymbol{u}$ the velocity field and $\boldsymbol{g}$ is the gravity, assumed to be constant with depth.

Because the densities and pressures change by 4-5 orders of magnitude from the top to the bottom of the simulations, it is advantageous to precondition the equations for use in the highly stratified case of stellar atmospheres. This is done by rewriting (2.1) - (2.3) in terms of logarithmic density, $\ln\varrho$, velocity, $\boldsymbol{u}$, and internal energy per unit mass, ε:

$$\frac{\partial \ln\varrho}{\partial t} = -\boldsymbol{u} \cdot \nabla \ln\varrho - \nabla \cdot \boldsymbol{u}, \tag{2.4}$$

$$\frac{\partial \boldsymbol{u}}{\partial t} = -\boldsymbol{u} \cdot \nabla \boldsymbol{u} + \boldsymbol{g} - \frac{P_{\rm g}}{\varrho} \nabla \ln P \tag{2.5}$$

and

$$\frac{\partial \varepsilon}{\partial t} = -\boldsymbol{u} \cdot \nabla \varepsilon - \frac{P}{\varrho} \nabla \cdot \boldsymbol{u} + Q_{\rm rad} + Q_{\rm visc}. \tag{2.6}$$

These equations are much more well behaved than (2.1) - (2.3) and the various derivatives are also smoother.

The radiative energy exchange rate is

$$Q_{\rm rad} = \varrho \int_\lambda \int_\Omega \kappa_\lambda (I_{\lambda,\Omega} - S_\lambda) {\rm d}\Omega {\rm d}\lambda, \tag{2.7}$$

and will be discussed further in Sect. 4. The viscous dissipation is

$$Q_{\rm visc} = \sum_{i,j} \nu_j \left(\frac{\partial u_i}{\partial x_j} \right)^2, \tag{2.8}$$

where the ν_j's are the direction-dependent diffusion coefficients, discussed in Sect. 2.2.

Let us return to the per-volume version of the mass- and momentum equations. Adding $\boldsymbol{u}$ times mass conservation (2.1) to the momentum equation (2.2) we get

$$\frac{\partial \varrho \boldsymbol{u}}{\partial t} = -\nabla \cdot (\boldsymbol{u}\boldsymbol{u}\varrho) - \nabla P_{\rm g} + \boldsymbol{g}\varrho \tag{2.9}$$

and taking the horizontal average of this

$$\frac{\partial \langle \varrho u_z \rangle}{\partial t} = -\frac{\partial}{\partial z}(\langle \varrho u_z^2 \rangle + \langle P_{\rm g} \rangle) + g\langle \varrho \rangle, \tag{2.10}$$

which naturally leads us to the definition

$$P_{\rm turb} = \langle \varrho u_z^2 \rangle \tag{2.11}$$

of the turbulent pressure — a quantity I will return to frequently.

2.2 Diffusion

The numerical time stepping (see Sect. 2.4) is stable, but the numerical evaluation of spatial derivatives introduces some anti-diffusion that needs to be counteracted with the artificial diffusion described here. The artificial diffusion is *not* an attempt to mimic molecular-type diffusion, nor does it attempt to model subgrid-scale motions. Rather, the various contributions to the artificial diffusion are instrumented so that they stabilize the numerical behaviour at scales comparable to the mesh size, in various regimes of fluid motions (advection, sound waves, shocks, ...), while leaving larger-scale, well-resolved motions as unaffected as possible.

For a per-unit-mass quantity f, second-order diffusion gives a contribution of the form

$$\frac{\partial f}{\partial t} = \cdots + \frac{1}{\rho}\sum_j \frac{\partial}{\partial x_j}\left[\nu_j \rho \frac{\partial f}{\partial x_j}\right]. \tag{2.12}$$

Numerically, it is an advantage to expand this into

$$\frac{\partial f}{\partial t} = \cdots + \sum_j \left[\nu_j \frac{\partial^2 f}{\partial x_j^2} + \left(\frac{\partial \nu_j}{\partial x_j} + \nu_j \frac{\partial \ln \varrho}{\partial x_j}\right)\frac{\partial f}{\partial x_j}\right]. \tag{2.13}$$

At constant ρ and ν_j, a "saw-tooth" f-variation (with wavelength $\lambda = 2\Delta x$) has a vanishing first derivative (when evaluated with a second- or higher-order difference scheme), and hence Eq. (2.12) does not give rise to any diffusion, in the very case where it is most needed. Equation (2.13), on the other hand, damps such a saw-tooth effectively. Since its first derivative vanishes, a saw-tooth cannot be advected and it is indeed desirable to damp it out.

Notice that the diffusion coefficients ν_j are direction-dependent, which has two immediate advantages: the diffusion gets proportional to the grid spacing, which is rather important as the z-scale is irregular and the aspect ratios of the simulations typically are about 2:1. Also shocks and waves are stabilized without affecting the directions parallel to them.

For $f = \ln\varrho$ or $f = \varepsilon$, the diffusion in the z-direction is only applied to the fluctuations, *e.g.* $f = \ln\varrho - \langle\ln\varrho\rangle$, to prevent diffusion of the mean stratification.

During my work with the code, the diffusion has undergone quite a few improvements (Stein et al. 1997), increasing its efficiency while minimizing the overall diffusion. Following Nordlund & Galsgaard (1997) I will refer to the new type of diffusion as *quenched diffusion* and is described below in Sect. 2.2.2, while the original scheme is referred to as *mixed second- and fourth-order diffusion.*

2.2.1 Mixed second- and fourth-order diffusion

The diffusion is separated into two parts: a second-order diffusion that has a coefficient with two different contributions

$$\nu_{2j} = (a_1|u_j| + a_2\Delta_4^+ u_j)\frac{\Delta x_j}{12}, \tag{2.14}$$

and a fourth-order diffusion,

$$\frac{\partial f}{\partial t} = \cdots - \frac{1}{\rho}\sum_j \frac{\partial^2}{\partial x_j^2}\left[\nu_j\rho\frac{\partial^2 f}{\partial x_j^2}\right], \tag{2.15}$$

that has a coefficient with the two contributions

$$\nu_{4j} = (4a_1|u_j| + a_3\tilde{c}_{\rm s})\frac{\Delta x_j}{12^2}. \tag{2.16}$$

The numbering of the terms a_1-a_3 is chosen to be consistent with the notation in the source code of the program. The terms in a_1 are proportional to the fluid speed, and prevent ringing at sharp changes in advected quantities. The term in a_3 is proportional to the (fiducial) sound speed $\tilde{c}_{\rm s}$, stabilizes weak waves, numerical differentiation and the time stepping. The term in a_2 is proportional to a velocity divergence spread out over 4 grid points:

$$\Delta_4^+ u_j(k) = \sum_{\Delta k=-1}^{2} \Delta^+ u_j(k - \tfrac{1}{2} + \Delta k), \tag{2.17}$$

where k enumerates the grid-points in the j-direction, and

$$\Delta^+ u_j(k - \tfrac{1}{2}) = [u_j(k-1) - u_j(k)]_+ \tag{2.18}$$

is the positive part of the upstream – downstream velocity difference, centered on $k - \frac{1}{2}$. Note that $\Delta_4^+ u_j$, with the above definitions, is in fact centered on k. This last term in the diffusion coefficient stabilizes shock fronts.

The fiducial soundspeed used in (2.16) is just

$$\tilde{c}_{\rm s}^2 = 1.67 \times \frac{\langle P_g \rangle}{\langle \varrho \rangle} \tag{2.19}$$

calculated from horizontally averaged pressure and density, rather than the exact adiabatic soundspeed

$$c_{\rm s}^2 = \frac{\Gamma_1 P_g}{\varrho}. \tag{2.20}$$

The difference, due to the variation of Γ_1 with ionization, is just 15–20% and only below the photosphere, and it should not affect the properties of the diffusion.

The corresponding dissipation is

$$Q_{\rm visc} = \sum_{i,j} \left[\nu_{2j} \left(\frac{\partial u_i}{\partial x_j} \right)^2 + \nu_{4j} \left(\frac{\partial^2 u_i}{\partial x_j^2} \right)^2 \right] \tag{2.21}$$

where ν_{2j} and ν_{4j} are the coefficients for the second- and fourth-order diffusion respectively.

2.2.2 Quenched diffusion

With the quenched diffusion, only the shock capturing a_2 term remains in the second-order part of the diffusion.

$$\nu_{2j} = a_2 f_\varrho \Delta_4^+ u_j \frac{\Delta x_j}{12}. \tag{2.22}$$

The ν_{4j} coefficient is similar to the mixed second- and fourth-order case, and

$$\nu_{4j} = (a_1 |u_j| + a_2 f_\varrho \Delta_3 u_j + a_3 \tilde{c}_{\rm s}) \frac{\Delta x_j}{12}. \tag{2.23}$$

One of the improvements consists of including the ϱ-scaling

$$f_\varrho^{-1} = 1 + \langle \varrho \rangle / \varrho_{\rm ref} \tag{2.24}$$

where $\varrho_{\rm ref}$ is a reference density, chosen to be the horizontal mean density just below the photosphere. This scaling reduces the shock capturing diffusion in the dense layers, where the motions are gentle.

The main improvement consists of using an expression for ν_{4j} that involves a (signed) first-order difference, scaled with the ratio of (unsigned) third-order differences to (unsigned) first-order differences,

$$\frac{\Delta_3 f}{\Delta x_j} = \frac{\Delta f}{\Delta x_j} \frac{\max_3 |\Delta^3 f|}{\max_3 |\Delta f|}, \tag{2.25}$$

centered on $k-\frac{1}{2}$. The $\max_3$-operator takes the maximum value in a three-point neighbourhood of k, *i.e.* $k-1, k, k+1$. The third-order difference is defined by

$$\begin{aligned} \Delta f(k-\tfrac{1}{2}) &= f(k) - f(k-1), && (2.26)\\ \Delta^2 f(k) &= \Delta f(k+\tfrac{1}{2}) - \Delta f(k-\tfrac{1}{2}) \quad \text{and} && (2.27)\\ \Delta^3 f(k-\tfrac{1}{2}) &= \Delta^2 f(k) - \Delta^2 f(k-1). && (2.28) \end{aligned}$$

By scaling the first-order difference in this way one obtains a diffusive flux that has the sign of the first-order difference, but the order of magnitude of the third-order difference. In smooth parts of the solution the diffusive flux will thus be quenched (hence the denomination), and the effect of the diffusion operator will be of similar magnitude as that of a fourth-order diffusion operator. In steep parts of the solution, on the other hand, the ratio of the third- to first-order difference will be of the order unity or larger, and the diffusion will be similar to normal second-order diffusion.

The diffusion contributions are combined into

$$\frac{\partial f}{\partial t} = \cdots + \frac{1}{\varrho}\sum_j \frac{\partial}{\partial x_j}\left[\varrho\left(\nu_{2j}\frac{\partial f}{\partial x_j} + \nu_{4j}\frac{\Delta_3 f}{\Delta x_j}\right)\right], \tag{2.29}$$

where the first part is a second-order diffusion that is active mainly in shocks. The second part is qualitatively similar to a fourth-order diffusion, but has the advantage that sharp edges and localized peaks do not give rise to the ringing that tends to develop with a normal fourth-order operator. In the combined second- and fourth-order diffusion, enough second-order diffusion must be present to counteract the tendency for ringing from the fourth-order operator. Since this tendency is not present when (2.29) is used, one can remove the second-order diffusion altogether, except in shocks, where significant local diffusion is always needed.

The dissipation that corresponds to (2.29) is

$$Q_{\text{visc}} = \sum_{i,j}\left[\frac{\partial u_i}{\partial x_j}\left(\nu_{2j}\frac{\partial u_i}{\partial x_j} + \nu_{4j}\Delta_3 u_i\right)\right]. \tag{2.30}$$

The diffusion at the top and the bottom are set to zero in both diffusion schemes to avoid boundary effects. All of the non-local operators take advantage of the periodic properties in the horizontal directions and are skewed at the top and bottom boundary.

2.3 Boundary Conditions

2.3.1 The horizontal boundaries

The horizontal boundaries are by far the easiest to handle. There are no prefered directions, so a periodic boundary, expressed for a discrete variable f as

$$f(0) = f(N_i + 1) \qquad \text{for} \quad i = x, y, \tag{2.31}$$

where N_i is the number of points in direction i, is a very reasonable choice. This of course only works if the size of the simulation box is large enough to contain a few of the largest structures we want to investigate. These structures are in this case granules, and each of the simulations are ensured to contain 6-8 granules on average (See Fig. 7.4). This choice of scale means that we cannot investigate rotation [Brummell et al. (1996) has produced some nice simulations, including the effects of rotation] or meso/super granulation. Then it also means that we do not have to worry about these effects.

2.3.2 The top boundary

The uppermost plane in the simulation box, $i = 1$, is a fiducial layer, which is not treated as part of the simulation but just serves to guide the actual boundary layer at $i = 2$. This fiducial layer is placed three times further apart from the $i = 2$ layer than the next point inward, *i.e.* $z_2 - z_1 = 3(z_3 - z_2)$. This is also more than one pressure scaleheight,

$$H_P = \frac{\langle P_g \rangle}{g\langle \varrho \rangle}, \tag{2.32}$$

above the $i = 2$ layer, helping to minimize the influence of the fiducial layer. The density fluctuations at $i = 2$ are just copied to the fiducial layer and scaled as

$$\varrho_1 = \varrho_2 \frac{\langle \varrho \rangle_1^*}{\langle \varrho \rangle_2}. \tag{2.33}$$

The horizontally averaged density at $i = 1$ is advanced with the horizontally averaged mass flux, to keep it close to hydrostatic equilibrium,

$$\langle \varrho \rangle_1^* = \langle \varrho \rangle_1 - \Delta t H_{P,1} \langle \varrho u_z \rangle_1. \tag{2.34}$$

The velocities are copied directly from the boundary layer

$$\boldsymbol{u}_1 = \boldsymbol{u}_2, \tag{2.35}$$

and the energy is set to a constant, $\varepsilon = \bar{\varepsilon}_1$, for the whole plane. $\bar{\varepsilon}$ is a vertically smoothed, horizontal average, which is not evaluated at each timestep, but at about 10 s intervals. Originally, $\bar{\varepsilon}$ at $i = 1$ was kept constant in time, and just set by the initial state of the simulation. I changed this to a damped, linear extrapolation:

$$\bar{\varepsilon}_1 = \bar{\varepsilon}_1 d + (1 - d) \left[\langle \varepsilon \rangle_2 - \frac{\langle \varepsilon \rangle_3 - \langle \varepsilon \rangle_2}{z_3 - z_2} (z_2 - z_1) \right], \tag{2.36}$$

where the damping consists of using the fractions d of the previous $\bar{\varepsilon}_1$ and $d - 1$ of the extrapolation. I have chosen $d = 0.7$, which prevents the uppermost layers from fluctuating wildly after having kicked the model, by *e.g.* changing input physics, the z-scale, or the mean structure to adjust $T_{\rm eff}$. This choice of the top energy does

not affect the simulation when it is relaxed, but ensures that the simulation is able to relax to whatever state it wants to.

The purpose of the fiducial layer is to make it possible to implement a transmitting boundary at $i = 2$. The presence of the fiducial layer at $i = 1$ makes a spline derivative at $i = 2$ more well behaved than a one-sided derivative. Because of the larger $z_2 - z_1$ interval, the derivative is still mostly determined by the shape of the function inside the boundary (at $i = 2$), and works more or less as a one-sided derivative. The presence of the fiducial layer "ties down" the function at $i = 1$ and thus prevents the boundary instabilities that otherwise result from using one-sided derivatives at a boundary. The excellent transmitting properties of the top boundary have been investigated by Nordlund & Stein (1990).

2.3.3 The bottom boundary

The bottom boundary is constructed to be a node in pressure waves (p-modes), to transmit (convective) flows freely and to do no work on its own. This is accomplished by controlling the entropy of the in-flowing gas, and let the out-flowing gas pass undisturbed. The value of the entropy of the in-flowing gas also, ultimately, determines the effective temperature, $T_{\rm eff}$, of the simulation.

The variables are first advanced in time using

$$f \leftarrow f + \Delta t \frac{\partial f}{\partial t} \quad \text{for} \qquad f = \ln\varrho, \boldsymbol{u}, \varepsilon, \tag{2.37}$$

except for the pressure which is advanced using

$$P_{\rm b} \leftarrow P_{\rm b} + \Delta t \left[\frac{\partial \varepsilon}{\partial t} \left(\frac{\partial P}{\partial \varepsilon} \right)_{\varrho} + \frac{\partial \varrho}{\partial t} \left(\frac{\partial P}{\partial \varrho} \right)_{\varepsilon} \right], \tag{2.38}$$

instead of evaluating the pressure from an EOS call with the new ϱ and ε. This is all right for the Sun, but maybe not for stars with more violent convection where the fluctuations, even at the bottom boundary, are so large that the EOS, *e.g.* pressure, is no longer linear in the fluctuations of ϱ and ε.

The pressure is then set to $P_{\rm b} = \langle P_{\rm b} \rangle$ for the whole bottom plane. The entropy of the in-flowing plasma, $S_{\rm in}$, is controlled by specifying the density and energy of the in-flowing plasma, $\varrho_{\rm in}$ and $\varepsilon_{\rm in}$, and the deviation in entropy is

$$\Delta S = [\varepsilon - \varepsilon_{\rm in}] \left(\frac{\partial S}{\partial \varepsilon} \right)_{\varrho} + [\varrho - \varrho_{\rm in}] \left(\frac{\partial S}{\partial \varrho} \right)_{\varepsilon}. \tag{2.39}$$

Consequently the energy is changed according to

$$\Delta\varepsilon = \begin{cases} \dfrac{-\Delta t}{t_{\rm in}} \Delta S \left(\dfrac{\partial \varepsilon}{\partial S} \right)_P & \text{in} \\ 0 & \text{out.} \end{cases} \tag{2.40}$$

The timescale for changing the properties of in-flowing plasma is

$$t_{\rm in} = \tfrac{1}{2}\left|\frac{\Delta z_{\rm b}}{\max_{\rm in} u_z}\right|, \tag{2.41}$$

i.e. half the shortest time it takes in-coming plasma to cross the first vertical grid spacing. The five dependent quantities are changed according to

$$\varepsilon = \varepsilon + \Delta\varepsilon \tag{2.42}$$

$$\ln\varrho = \ln\varrho + \Delta\varepsilon\left(\frac{\partial \ln\varrho}{\partial\varepsilon}\right)_P \tag{2.43}$$

$$u_{x,y} = u_{x,y}(1 - \frac{\Delta t}{t_{\rm in}}) \qquad \text{in} \tag{2.44}$$

$$u_z = u_z + \frac{\Delta t}{t_{\rm in}}(\langle u_z\rangle_{\rm in} - u_z) \qquad \text{in,} \tag{2.45}$$

$$\tag{2.46}$$

where only the velocities of in-flowing plasma is altered. As a technical point, the bottom boundary layer is then changed back to its previous condition and the differences are turned into time derivatives and stored in the boundary layer of $\partial f/\partial t$, to allow for normal time stepping in this layer too (*cf.* Sect. 2.4.4).

2.4 Solving the Difference Equations

Due to the digital nature of computers, we have to discretize all the differentiations and integrations encountered, and this also leads to the need for interpolation. A function can only be evaluated at a finite and discrete set of points (in space or time), but to calculate derivatives and integrals, we have to decide on what we think happens between grid-points.

2.4.1 Spatial interpolation

Spatial interpolation is done by *cubic spline* interpolation as described in de Boor (1978). The most important property of cubic splines is their smoothness. Each interval is interpolated by a third-order polynomial

$$f(x) = f_i + \Delta x f' + \tfrac{1}{2}\Delta x^2 f'' + \tfrac{1}{6}\Delta x^3 f''', \qquad \Delta x = x - x_i, \tag{2.47}$$

constrained by the requirement that the total interpolating function is twice differentiable (having piecewise linear second derivatives).

This all sounds like excellent properties, but everyone having dealt with polynomial interpolation of real-world data knows that sharp edges are disastrous for

the interpolation, causing the interpolating function to oscillate wildly on both sides of the edge. An optimization of the grid can prevent (or at least minimize) such oscillations, by increasing the resolution around the edge giving better guidelines for the interpolation, as described in Sect. 2.5.

2.4.2 Spatial derivatives

As cubic spline interpolation is twice differentiable, the derivatives from the interpolating functions are used. This ensures consistency and smoothness. Between grid-points we have

$$f'(x) = f'_i + \Delta x f'' + \tfrac{1}{2}\Delta x^2 f'''. \tag{2.48}$$

2.4.3 Spatial integration

Together with the spline interpolation and differentiation, one can of course also derive the corresponding integral. Integrating Eq. (2.47) and combining with Eq. (2.48) result in the following compact and easy-to-evaluate expression

$$\int_{x_i}^{x_{i+1}} f(x)dx = \Delta x_i \left[\tfrac{1}{2}(f_i + f_{i+1}) + \frac{\Delta x_i}{12}(f'_i - f'_{i+1})\right]. \tag{2.49}$$

2.4.4 Time stepping

The time is advanced using the *Hyman third-order leap-frog* method, with variable time step (Strikwerda 1989, chapter 8). It is a two-step method, with odd steps being leap-frog predictor steps, and even steps acting as third-order corrector steps. Odd steps are advanced using

$$f(n{+}1) = af(n{-}1) + [1-a]f(n) + bf'(n), \tag{2.50}$$

where the time derivatives, $f'(n)$ are given by Eqs. (2.4)-(2.6). The coefficients a and b are found from inserting in (2.50) the Taylor expansion of $f(n{-}1)$ around $f(n)$

$$f(n{+}1) = f(n) + [b - a\Delta t_{\rm old}]f'(n) + \tfrac{1}{2}a\Delta t_{\rm old}^2 f''(n) + \mathcal{O}(3) \tag{2.51}$$

and comparing with a Taylor expansion of $f(n{+}1)$ around $f(n)$

$$f(n{+}1) = f(n) + \Delta t f'(n) + \tfrac{1}{2}\Delta t^2 f''(n) + \mathcal{O}(3), \tag{2.52}$$

yielding

$$a = r^2, \qquad b = \Delta t[1+r] \quad \text{with} \qquad r = \Delta t/\Delta t_{\rm old}. \tag{2.53}$$

Here the time steps are $\Delta t_{\rm old} = t(n) - t(n{-}1)$ and $\Delta t = t(n{+}1) - t(n)$.

The even step does not advance in time, but serves to evaluate the time derivative at the new time step, $f'(n{+}1)$, which can then be used to improve the estimate of $f(n{+}1)$ as found in the odd step. At the even step we have

$$f(n{+}1) = cf(n{-}1) + [1-c]f(n) + df'(n)\Delta t + ef'(n+1)\Delta t, \tag{2.54}$$

with n being the same as in (2.50) for the odd step. The coefficients c–e (and the motivation for the expression) can be found by inserting the Taylor expansions of $f(n-1)$ and $f'(n+1)$ around $f(n)$

$$f(n+1) = f(n) + [d\Delta t - c\Delta t_{\rm old} + e\Delta t]f'(n) \qquad (2.55)$$
$$+ [\tfrac{1}{2}c\Delta t_{\rm old}^2 + e\Delta t^2]f''(n) + [-\tfrac{1}{6}c\Delta t_{\rm old}^3 + \tfrac{1}{2}e\Delta t^3]f'''(n) + \mathcal{O}(4),$$

this time including up to third-order terms. Again comparing with the Taylor expansion of $f(n+1)$ (2.52), but now retaining also the third-order term, $\frac{1}{6}\Delta t^3 f'''(n)$, gives

$$c = \frac{r^3}{2+3r}, \qquad d = \frac{(1+r)^2}{2+3r} \quad \text{and} \qquad e = \frac{1+r}{2+3r}. \qquad (2.56)$$

So even though either (2.50) nor (2.54) contains derivatives of order higher than one, the scheme is in fact a third-order scheme.

2.5 The z-grid

The cubic splines used for both interpolation, differentiation and integration as described above are rather sensitive to abrupt changes in the quantity to be interpolated. If there are too few points on each side of the transition to guide the splines, they will tend to develop oscillations in this region. As we have some very sharp transitions in the photosphere above granules, we have to make sure that these transitions are resolved well enough to avoid such oscillations.

It can be shown that the optimum mesh for resolving a function f is defined by

$$\int_{x_1}^{x_i} \sqrt{|f''|}\mathrm{d}x = \frac{i-1}{N-1}\int_{x_1}^{x_N} \sqrt{|f''|}\mathrm{d}x \qquad \text{for} \quad i = 1, \ldots, N \qquad (2.57)$$

(de Boor 1978, pp. 44). Equation (2.57) states that the mesh, x_i, should be equidistant in the square root of the second derivative. The interpretation of this is rather simple: As straight lines, no matter the slope, are fully described by just two points, we are interested in the deviation from straight lines, that is f''. The reason for the $|\ldots|$ is obvious and the square root distributes changes evenly between the function and the mesh.

For f'' I use

$$f'' = \max_h \frac{\mathrm{d}^2 T}{\mathrm{d}z^2}, \qquad (2.58)$$

where $\max_h$ is the maximum for each horizontal plane. But we want a z-scale constant in time, so instead of (2.58), which is rather "noisy" and time dependent, I use a loose fit to (2.58) at a single time step, to a function of the form

$$f'' = \left[|z - z_0| + a e^{-\left(\frac{z-z_0}{b}\right)^4}\right]^{-1} \qquad (2.59)$$

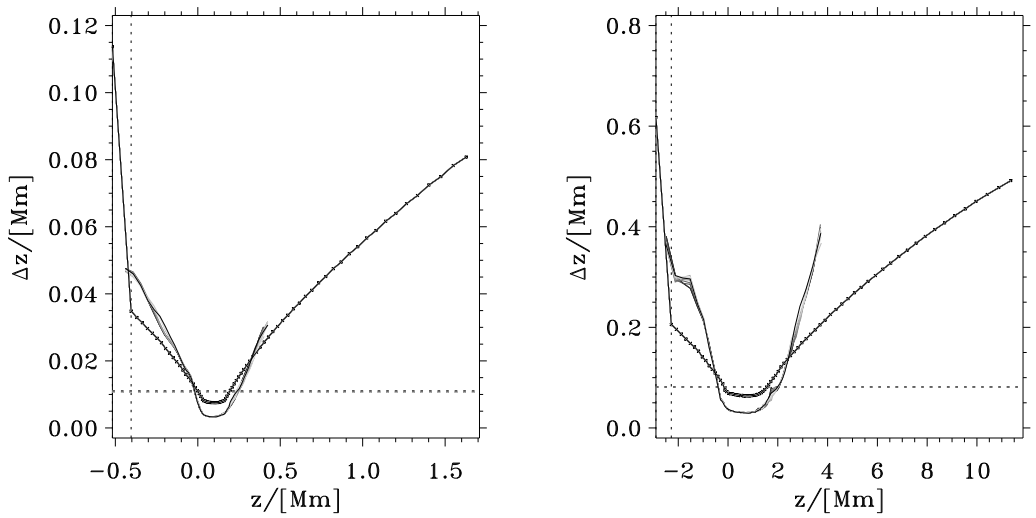

Fig. 2.1: These two plots illustrates the z-scales for the simulation of α Cen B to the left, and of η Boo to the right. The z-scales are shown with solid lines and each z-point is marked by a small cross. The $z_{\rm rad}$-scale is plotted for 10 timesteps from each of the simulations to demonstrate the stability of the method. The horizontal dotted lines shows $\langle \Delta z \rangle$ and the vertical dotted line marks the upper boundary of the simulation (the uppermost plane is the fiducial layer, (*cf.* Sect. 2.3.2).

giving a nice and smooth z-scale (See Fig. 2.1). As the simulation evolves, this z-scale is routinely checked for consistency with (2.58) and renewed if necessary.

The detailed radiative transfer is solved on its own grid, $z_{\rm rad}$, as only part of the simulation box is involved ($\tau < 300$) and as we need all the resolution we can get. For this grid I use

$$f'' = \max_h \frac{\mathrm{d}\ln \varrho\kappa_{\rm c}}{\mathrm{d}z}, \tag{2.60}$$

which is chosen to give a good optical depth scale, τ. This expression does not follow the idea of (2.57) strictly, but as τ is the vertical integral of $\varrho\kappa$ [*cf.* Eq. (4.24)], (2.60) can be seen as a smoothed version of $\mathrm{d}^2\tau/\mathrm{d}z^2$.

The grid in the horizontal directions is regular, and is not optimized in any way. Instead the horizontal extent of the simulations is chosen to contain a certain number of granules, to make the simulation box a representative part of the stellar surface. The horizontal variation of any quantity is anyway rather modest, making the spline interpolation safe, even with a poor resolution.

2.6 Damping of p-modes

Initial configurations of the simulation box will most likely not be in exact vertical pressure balance. If the starting configuration is constructed to have a horizontally

averaged thermodynamic structure in hydrostatic equilibrium, but with a fairly random velocity field, there will be surplus energy either in the form of kinetic energy because of too high velocities, or in the form of potential energy because of too low velocities. In either case, this energy will go into excitation of p-modes that can have rather high amplitudes (because of the small mass contained in the box), depending on how far the initial configuration were from the statistical steady state

The only way for the p-modes to loose energy is through dissipation, but the dissipation is negligible on the scale of the p-mode wavelength so we need to help it a little by artificially extracting energy from the modes. This is done by adding a damping term to the time derivative of the vertical velocity. The velocity fluctuation associated with the mode is

$$v_{\rm mode} = \frac{\langle \varrho u_z \rangle}{\langle \varrho \rangle}, \tag{2.61}$$

where the $\langle \ldots \rangle$ denotes a horizontal (not temporal) average. We only observe radial (or vertical as the simulation is plane parallel) modes in the simulations, justifying that (2.61) only includes the z-component.

If we want this p-mode component of the velocity field to decrease exponentially with time,

$$v_{\rm mode} = v_{\rm mode,0} e^{-t/t_{\rm damp}}, \tag{2.62}$$

with a damping time $t_{\rm damp}$, it will obey the differential equation:

$$\frac{{\rm d}v_{\rm mode}}{{\rm d}t} = -\frac{v_{\rm mode}}{t_{\rm damp}}. \tag{2.63}$$

This term is now added to the time derivative of the vertical velocities

$$\frac{{\rm d}u_z}{{\rm d}t} = \left(\frac{{\rm d}u_z}{{\rm d}t}\right)_0 - \frac{v_{\rm mode}}{t_{\rm damp}} \tag{2.64}$$

efficiently damping any p-modes.

The damping time, $t_{\rm damp}$, should be chosen similar to the p-mode periods, to obtain near-critical damping. If the damping time is too long, the p-mode is damped too slowly, while if the damping time is too short it takes a too long time for the model to reach vertical pressure equilibrium. I have found that a $t_{\rm damp}$ 1.3 times larger than the dominant p-mode period is a good choice for efficient damping.

In some of the simulations I find two p-modes with a small separation in frequency and similar amplitudes interfering with each other, resulting in the well-known beat phenomena. The modulation of the amplitude can easily be mistaken for damping and complicates the analysis of the damping quite a bit.

After having damped the oscillations as much as possible in this way, the damping is turned off before the simulations are used for further analysis. This damping does not destroy the p-modes alltogether, but brings the amplitude down to a level which is the natural amplitude for the simulation, determined by the convective forcing

and damping, as well as the mass contained in the box. The remaining oscillations can thus surely tell us a lot about convection as an excitation mechanism for p-mode oscillations (Stein 1989; Stein & Nordlund 1990; Musielak et al. 1994), but I will leave that subject for another project.

Chapter 3

The atomic physics foundation

The ongoing work of expanding our basic knowledge about atoms, ions and molecules, is a cornerstone for both equation of state (EOS) and opacity calculations, and in 1984 the biggest coordinated effort ever was initiated to make extensive compilations of such data of all atoms and ions of astrophysical interest. This is the Opacity Project, abbreviated OP. Some 30 of the constituent articles have been collected in the OP books (Seaton 1995; Berrington 1997), covering both the EOS, the opacity and the atomic data calculations. If one does not feel like reading the more than 500 pages, I can at least recommend browsing the books, to get a feeling for the current state of atomic physics. It is very instructive, and the level of sophistication in the modelling and analysis is really impressive. At the same time though, one also realizes that all these issues still are very open. It seems as if we know even less than 20 years ago, when the astrophysical community used the LAOL-opacities (Los Alamos Astrophysical Opacity Library) (Huebner et al. 1977). It was a common belief at that time that any refinements in the atomic physics would only result in a marginal change in the opacity and an even smaller change in the EOS. At that time we seemed very close to the truth.

By now (after browsing the OP books) we have learned that very many effects are in play at the same time and that each discarded approximation has meant a significant alteration of the EOS and the opacity. That these changes really are improvements has been confirmed by much better agreement with observations in a variety of astrophysical problems, *e.g.* helioseismology (Christensen-Dalsgaard & Däppen 1992; Dziembowski et al. 1992) and modelling of variable stars (Petersen 1990; Moskalik & Dziembowski 1992). Detailed comparisons with experiment, ion for ion, state for state (as can be seen throughout the OP book) are very reassuring, clearly indicating that the right tracks are followed and that we are closer to the real world than ever. But it is also evident that there still remains a good deal of work before the chapter can be closed.

3.1 Chemical Mixture

As one often realizes, the world is far from ideal, which is also the case here. I have to use different chemical mixtures for different parts of the atomic physics. The MHD EOS program is numerically heavy, and including more than the adopted 6

Table 3.1: Abundances for various relevant mixtures.

	A	Gust.	AGN92	solar	MHD[a]	MHD[b]	χ_1	χ_2	χ_3
H	1.008	12.00	12.00	12.00	12.00	12.00	13.60[c]		
He	4.003	11.00	11.00	10.92	10.92	11.00	24.59[c]	54.42	
C	12.01	8.55	8.55	8.53	8.56	8.58	11.26[c]	24.38	47.89
N	14.01	7.93	7.97	7.91	7.88	7.90	14.53[c]	29.60	47.45
O	16.00	8.77	8.87	8.75	8.78	8.80	13.62[c]	35.12	54.93
Ne	20.18	8.51	8.07	8.49	—	—	21.56	40.96	63.45
Na	23.00	6.18	6.33	6.16	—	—	5.14[c]	47.29	71.64
Mg	24.32	7.48	7.58	7.46	—	—	7.65[c]	15.04[c]	80.14
Al	26.97	6.40	6.47	6.38	—	—	5.99[c]	18.83	28.45
Si	28.06	7.55	7.55	7.53	—	—	8.15[c]	16.35	33.49
S	32.06	7.21	7.21	7.19	—	—	10.36	23.33	34.83
K	39.10	5.05	5.13	5.03	—	—	4.34	31.63	45.72
Ca	40.08	6.33	6.36	6.31	—	—	6.11[c]	11.87[c]	50.91
Cr	52.01	5.47	5.67	5.45	—	—	6.77	16.50	30.96
Fe	55.85	7.50	7.51	7.48	8.23	8.25	7.87[c]	16.16	30.65
Ni	58.69	5.08	6.25	5.06	—	—	7.64	18.17	35.17
X/[%]		70.296	70.350	73.694	73.694	70.296			
Y/[%]		27.916	27.937	24.500	24.500	27.916			
Z/[%]		1.788	1.713	1.806	1.806	1.788			
μ(no ioni)		1.3018	1.3009	1.2605	1.2606	1.3018			
μ(full ioni)		0.6196	0.6193	0.6039	0.6040	0.6196			

[a] The six element mixture mimicking the "solar" composition

[b] The six element mixture mimicking the "Gust." composition

[c] The atom/ion is included as a source of opacity

elements, would make it prohibitively slow, even though it only has to be run once. The ODFs (see Sect. 3.3.3) taking care of the line opacity, have been calculated for a much more realistic mixture (Anders & Grevesse 1989, will be referred to as AG89), including all elements from hydrogen through uranium. As I need more elements to calculate continuous opacities than provided with the MHD EOS, I use the original EOS by Gustafsson (1973) as a basis for these opacity calculations. Fortunately I can change the mixture used for the latter, to for example the one used for the ODFs, although only using 16 most abundant elements out of the 92 elements included in the ODF calculation (Kurucz 1992a).

Table 3.1 displays the different mixtures used for this work, and a few fundamental data for the elements. The second column in the table contains the atomic weights adopted for the `tabcmp`-program. The MHD EOS uses one more digit, but are consistent with the values listed here. The last three columns contain the ionization potentials in eV for the first few ionization stages, which are included in this table to give a feeling for at what temperatures the various ions are important. For the solar mean stratification, half of the hydrogen will be ionized at a temperature of around 22 900K and half of the helium will be single ionized at 41 700K. Potassium, the element included with the lowest ionization potential, is ionized throughout the solar atmosphere, as it ionizes at a temperature well below the temperature minimum (see Fig. 1.1).

The abundances tabulated in Tab. 3.1 are all logarithmic abundances by numbers, normalized to 12.00 for hydrogen. Below the element listing, I also give the corresponding "global" parameters; the fractions by mass, X, Y and Z and the mean molecular weights, μ, for the non-ionized and the fully ionized mixture respectively.

The third column, labelled "Gust." contains the original abundances (Gustafsson et al. 1975, Tab. 1). This is the mixture I have used for the low-res simulations and its global parameters are fairly close to the mixture adopted by Kurucz (1992c) for his ODF calculations, although he uses the full AG89 mixture, from hydrogen to uranium. In order to compare EOS-effects on the simulations, I have also calculated a 6-element mixture with exactly the same global parameters as for the Gust. mixture, for use with the MHD EOS.

The fourth column lists the newest and most often cited solar abundance which is AG89 updated by Grevesse & Noels (1992) (AGN92), most noticeable resulting in a lowering of the solar photospheric iron abundance, bringing it into agreement with meteoritic abundances. AGN92 is not used in the present work, but is merely included for comparison.

The fifth column is the mixture I adopt for the best solar. The heavy element mixture is taken from AG89 (to agree with Kurucz) for the 14 metals I include. These abundances are then scaled in accordance with the meteoritic and solar photospheric metal to hydrogen ratio; $Z_\odot/X_\odot = 0.0245$ (AGN92) and with helioseismology (Basu & Antia 1995) which yields $Y_\odot = 0.245$.

The sixth and seventh column list the truncated mixture used for the MHD EOS calculations. The heavy-element mixture has been adjusted to give X, Y, Z and μ's that agree with the Gust and solar mixtures respectively. These five global quantities for the solar and the Gust. mixtures, are seen to agree very well with the corresponding 6-element mixtures for the MHD EOS calculations, with only small deviations on the sixth significant digit.

3.2 The Equation of State

In this section I will outline the ideas behind the original EOS, and compare this with my update, which consists in employing the so-called MHD EOS (Hummer & Mihalas 1988; Mihalas et al. 1988; Däppen et al. 1988; Mihalas et al. 1990). This MHD is an acronym for the authors; Mihalas, Hummer and Däppen (in order not to get confused with magneto-hydro-dynamics I will always refer to this EOS as the MHD EOS) and it is the EOS which is part of the Opacity Project.

An EOS deals with the problem of determining the occupation of the possible states of a plasma. Among these states we have (going from high energies toward lower energies) the continuum of states of free electrons and free nuclei, bound electronic states (electrons around nuclei forming ions and atoms) and bound states of nuclei forming molecules and molecular ions.

The EOS is calculated under the assumption of local thermodynamic equilibrium (LTE) reducing the problem to only involving the local state of the environs, and the EOS can then be expressed as a function of only two independent parameters, say (ϱ, T),$(P_{\rm e}, T)$ or $(N_{\rm e}, T)$, with ϱ being the mass density, $P_{\rm e}$ the electron pressure, $N_{\rm e}$ the number of electrons per volume and T the temperature. Assuming LTE there is no ambiguity regarding temperature, as the radiation temperature and the kinetic temperatures of the constituent particles all are the same.

We now express the relative numbers of mutually reacting particles

$$X_1 \Longleftrightarrow X_2 + X_3, \tag{3.1}$$

as a chemical equilibrium via a stoichiometric equation:

$$\mu_1 = \mu_2 + \mu_3 \quad \text{or} \quad \psi_1 = \psi_2 + \psi_3 \tag{3.2}$$

where the μ's are the chemical potentials of the respective particles, and the $\psi_i = \mu_i/kT$ are the degeneracy parameters. The second equation is only valid if all the reacting particles have the same temperature, which is the case in LTE. The energies of the three particles are now related through

$$\epsilon_1 = E_1 \tag{3.3}$$

$$\epsilon_2 = E_2 + \chi \frac{m_2}{m_2 + m_3} \tag{3.4}$$

$$\epsilon_3 = E_3 + \chi \frac{m_3}{m_2 + m_3}, \tag{3.5}$$

where χ is the difference in internal energy between the left- and the right-hand side of (3.1), that is $\chi = E_{\rm int}(X_2 + X_3) - E_{\rm int}(X_1)$. The E_i's are the kinetic energies associated with the *Fermi-Dirac* distribution of the respective particles, and m_i are their masses. Equation (3.3)-(3.5) do not describe a single reaction, but are just statistical considerations.

Statistical mechanics tells us that the total number per volume of fermions having degeneracy parameter ψ, is obtained by integrating the distribution function over momentum p:

$$n = g\int_0^\infty \frac{4\pi p^2 dp}{h^3}\frac{1}{e^{-\psi+\epsilon/kT}+1}, \tag{3.6}$$

where g is the statistical weight or degeneracy of the state represented by the particle. Degeneracy of a state is normally due to the spin and/or rotational angular momentum of the particle, in which case $g = (2S+1)(2J+1)$. For a non-degenerate gas ($\psi \ll -1$) (3.6) reduces to

$$n = ge^{\psi}\int_0^\infty \frac{4\pi p^2 dp}{h^3}e^{-\epsilon/kT}. \tag{3.7}$$

Equation (3.2) can also be expressed as $e^{-\psi_1} = e^{-\psi_2}e^{-\psi_3}$, which, combined with (3.7) solved for $e^{-\psi}$ gives

$$\frac{n_2 n_3}{n_1} = \frac{g_2 g_3}{g_1}\frac{(2\pi kT m_2 m_3/m_1)^{3/2}}{h^3}e^{-\chi/kT}. \tag{3.8}$$

This version of the equilibrium equation is most applicable for molecular dissociation balances and ionization balances in stellar atmospheres, as all the particles are assumed non-degenerate. In stellar interiors an ionization process might involve a partially degenerate electron, so choosing particle 3 to be the electron we get

$$\frac{n_2}{n_1} = \frac{g_2}{g_1}\left(\frac{m_2}{m_1}\right)^{3/2}e^{-\chi/kT-\psi_e}, \tag{3.9}$$

where I have just left the $e^{-\psi_3}$-term unaltered. As m_1 and m_2 only differ by the very small mass of the electron, it is costumary to assume $m_1 = m_2$. The same is of course also applicable to (3.8) when used for ionization equilibria.

If each of the particles can exist in a number of states with different energies, (3.7) should be summed over these states to get the total number of particles regardless of their state of excitation

$$n = e^{\psi}\sum_k g_k\int_0^\infty \frac{4\pi p^2 dp}{h^3}e^{-\epsilon_k/kT}, \tag{3.10}$$

where subscript k numbers the states with $k = 0$ being the ground state. The energy is now $\epsilon_k = \epsilon + \chi_k$ where χ_k is the energy of the excited state relative to the ground state (*i.e.* $\chi_0 = 0$). The definition of ϵ in Eq. (3.3)-(3.5) still applies though χ, the energy difference between the left- and right-hand side of the reaction equation (3.1), should now be defined more precisely as this energy difference for the case where all the reacting particles are in their ground state. The kinetic properties of the particle are unaltered by excitation, and the summing over states can therefore be done outside the integral

$$n = e^{\psi}u\int_0^\infty \frac{4\pi p^2 dp}{h^3}e^{-\epsilon_k/kT}, \tag{3.11}$$

effectively defining the partition function

$$u = \sum_k g_k e^{-\chi_k/kT}. \tag{3.12}$$

This form can be used directly for atoms and ions, but if there are several kinds of independent excitations, as is the case for molecules, the various contributions are multiplied to get a final partition function. For a diatomic molecule (which is the only molecules considered in this work), it amounts to

$$u_{\rm mol} = \sum_k g_k e^{-\chi_k/kT} \sum_v \sum_J (2J+1) e^{-[\epsilon_v + \epsilon_J(v)]/kT}, \tag{3.13}$$

i.e. each bound electronic state k possesses a number of vibrational states v which again harbour a large number of closely spaced rotational states J. This is beautifully visualized in Fig. 3.6 of the line opacity, where the bands of rotational states for the first two vibrational states of the CO molecule are clearly seen (see the accompanying text for more detail). In Eq. (3.13) the degeneracy of electronic states is taken care of by the statistical weight g_k and degeneracy of vibrational states is included in the $(2J+1)$-factor. The sum is split in two, for the case of homonuclear molecules (H_2, C_2, N_2 and O_2): a *para*-part for even J and an *ortho*-part for odd J, weighted with a factor of 2 and 6 respectively.

Combining (3.11) with the stoichiometric equation (3.2), we can now write down the equivalents to (3.8) and (3.9)

$$\frac{n_2 n_3}{n_1} = \frac{u_2 u_3}{u_1} \frac{(2\pi kT m_2 m_3/m_1)^{3/2}}{h^3} e^{-\chi/kT} \tag{3.14}$$

and

$$\frac{n_2}{n_1} = \frac{u_2}{u_1} \left(\frac{m_2}{m_1}\right)^{3/2} e^{-\chi/kT - \psi_{\rm e}}. \tag{3.15}$$

These are the so-called *Saha equations*, describing dissociation and ionization equilibria, regardless of the reacting particles' internal states. We notice that the population of excited states can be expressed as

$$\frac{n_k}{n} = \frac{g_k}{u} e^{-\chi_k/kT}, \tag{3.16}$$

known as the *Boltzmann equation*.

Everything looks very nice till now, except that we haven't specified any upper limits for the summing over excited states. From elementary atomic physics we know that there is an infinite number of bound states in any atom and that the energy of these states converge to the ionization energy. Returning to the partition function (3.12) with this in mind, we see that the sum is divergent!

The divergence is of course not physical, nor is the infinity of states. The above-mentioned elementary atomic physics also tells us that the radii of hydrogenic or

highly excited atoms, as function of principal quantum number n, increase as n^2. So if the atom only has a limited amount of space to its disposal, it can only have a limited number of bound states. We therefore know that the partition function is finite, but how the sum should be truncated is far from trivial and is one of the main problems in EOS research.

In both the EOS considered here, the Stark effect is assumed to destroy otherwise bound states, and on basis of that, a probability for the existence of each state w_k is calculated — this is the so-called *occupation probability formalism*. In this picture the partition function (3.12) is changed to

$$u = \sum_{k=0} w_k g_k e^{-\chi_k/kT}, \tag{3.17}$$

making the sum convergent. Also a dependency of density enters, as w_k depends on the frequency of close encounters between atoms and ions in the plasma.

The Boltzmann formula (3.16) is of course changed accordingly, by adding a w_k in the numerator.

The next two sections describe two different ways of evaluating these weights, as well as two different ways of deriving thermodynamic quantities from the occupation numbers obtained.

3.2.1 The original EOS

The EOS, as used by Gustafsson (1973), follows the almost classical interpretation of the Debye & Hückel (1923) theory of electrolytes. This theory takes into account the presence of other atoms, ions and especially electrons, which according to the classical interpretation reduces the ionization potential by

$$\Delta\chi = 4.98 \cdot 10^{-4}(1+Z)\theta\sqrt{P_{\rm e}}/[\text{eV}], \tag{3.18}$$

where Z is the net charge of the atom/ion (Griem 1964, p. 139). He suggests to use $\Delta\chi = 0$ for H^-, but Gustafsson adopt $2\Delta\chi$ according to Tarafdar & Vardya (1969), *i.e.* changing to $(1+|Z|)$. The partition functions are separated into three terms:

$$u = g_0 + \sum_1^s [u' + u_{\rm as}], \tag{3.19}$$

where g_0 is the groundstate statistical weight and $u_{\rm as}$ is an asymptotic part which can be treated as hydrogenic. The intermediate 5-15 states going into u' are approximated by a small number (2-5) of substitute states, as evaluated by Traving et al. (1966), based on the measured energy levels as published in the first compilation by Moore (1949; 1952a; 1958). The summing over s in Eq. (3.19), is a summing over various doubly excited states, where the ionization will leave the ion in an excited state.

The asymptotic part of the partition function, $u_{\rm as}$, corresponding to states of principal quantum number p and higher, is evaluated using Eq. (3.17), summing from p, and the weights are

$$\ln w_k = 33.83 - \tfrac{2}{3}\ln(\sum_{ij} N_{ij} Z_{ij}^{3/2} + N_{\rm e}) + 4\ln\frac{Z'_k}{n_k}. \tag{3.20}$$

as first evaluated by Pannekoek (1938) and later refined by de Jager & Neven (1960) based on a static *Holtsmark* (Inglis & Teller 1939) distributed E-field.

The elements are numbered i, with $i = 1$ corresponding to hydrogen, and the ions are numbered with j, and $j = 0$ corresponds to a neutral atom. The total charge of the ion is therefore $Z_{ij} = j$. For ease of notation, I have suppressed the element and ion indexing of the left-hand side, and they are only included in summations over elements and ions. Z'_k and n_k are the effective charge and the principal quantum number of the kth state, respectively.

Defining p, as the effective principal quantum number for which $w_k = 1$, we get

$$p = 4.2 \cdot 10^3 Z'_k N_{\rm e}^{1/6}, \tag{3.21}$$

under the assumption that only single-ionizing atoms are present, *i.e.* taking the summation in Eq. (3.20) to be equal to $N_{\rm e}$.

Expanding the exponential in Eq. (3.17), and inserting the weights (3.20) yields

$$u_{\rm as} = p^4 m e^{-\chi/kT} \sum_{k=p}^{\infty} \frac{p^4}{n_k^4} n_k^2 \left(1 + \frac{D}{n_k^2} + \frac{D^2}{2n_k^4}\right), \tag{3.22}$$

where $D = (\chi - \chi_k)/kT$, and assuming that the asymptotic states are hydrogenic: $g_k = n_k^2$ and $n_k = k$. This sum is a *Hurwitz* or *generalized ζ-function* (Spanier & Oldham 1987), which can be approximated by integrals, yielding

$$Q_{\rm as} = \tfrac{4}{3}p^3 + \tfrac{1}{2}p^2 + \tfrac{1}{6}p + \tfrac{3}{4}Dp - \tfrac{2}{5}\frac{D^2}{p} - \tfrac{1}{3}(l-1)^2 - \tfrac{1}{6}(l-1) - D(l-1) + \tfrac{1}{2}\frac{D^2}{l}, \tag{3.23}$$

where finally

$$u_{\rm as} = 2 g_{\rm pr} Q_{\rm as} e^{-\chi/kT}. \tag{3.24}$$

The hydrogen molecule and its ion are treated according to Vardya (1965) and Mihalas (1967). Dissociation data for the molecules H_2O, OH, CH, CO, CN, C_2, O_2, N_2, NH and NO are taken from Tsuji (1973).

The gas pressure is just evaluated as the sum of the partial pressures

$$P_{\rm g} = P_{\rm e} + \frac{\varrho kT}{M_{\rm u}} \sum_i \frac{X_i}{A_i}, \tag{3.25}$$

where $M_{\rm u}$ is the atomic mass unit (a.m.u.), and the summing extends over all heavy species, *i.e.* atoms, ions and molecules, and $P_{\rm e}$ is the electron pressure. A_i is

the mass (in a.m.u.), and X_i is the abundance by mass fraction of the particle in question.

The internal energy per unit mass is evaluated from

$$\varepsilon = \tfrac{3}{2}\frac{P_{\rm g}}{\varrho} + \sum_i \frac{X_i}{A_i}\sum_j x_{ij}(\chi_{ij} - \Delta\chi_{ij}) + \sum_m \frac{X_m}{A_m}(D_m - \Delta E_m), \tag{3.26}$$

where the first term is the translational energy, the second term is the energy gained by ionization, summed over element i and ion j, and the last term is the energy gained by dissociation of molecules, m. D_m is the dissociation energy and ΔE_m is the sum of vibrational and rotational energies of the molecule. ΔE_m is neglected for all molecules except H_2 and H_2^+.

3.2.2 The MHD EOS

In the MHD EOS the destruction of states proceeds in a qualitatively different manner (Hummer & Mihalas 1988), as it takes into account the fluctuating behaviour of the perturbing field. The presence of an E-field splits the line into a Stark manifold of lines. As the field increase, the Stark manifolds of two adjacent principal states n and $n+1$, will eventually overlap and undergo avoided crossings. As the field decreases again, the electron can make a Landau-Zener transition, and be left in the $n+1$ Stark manifold. As the field changes sign and increase in amplitude, the electron will be lifted up towards the $n+2$ Stark manifold and the process repeats itself (Pillet et al. 1984).

It does not matter that the electron do not traverse the avoided crossing every time, as it gets plenty of new chances at subsequent traversals. The radiative lifetime for excited states is of the order 10^{-8} s, whereas the duration of collisions, as estimated by Hummer & Mihalas, is less than 10^{-12}s, so the atom will experience many encounters during the lifetime of a particular state. This picture of the field ionization is substantiated by experimental results (van Linden van den Heuvell & Gallagher 1985; Pillet et al. 1984).

The states having $|m| \leq 1$ are the easiest to ionize, and if these states govern the overall ionization of a principal state, n_k, the weight will be

$$\ln w_k = -\left(\frac{4\pi}{3V}\right)\left\{\sum_{ik'} N_{i0k'}(r_k + r_{i0k'})^3 + 16\left[\frac{(Z+1)^{1/2}e^2}{K_k^{1/2}\chi_k}\right]^3 \sum_{\alpha\neq \rm e} N_\alpha Z_\alpha^{3/2}\right\}, \tag{3.27}$$

where the quantal Stark-ionization correction factor K_k is

$$K_k = \frac{16}{3}\left(\frac{n_k}{n_k+1}\right)^2 \frac{n_k + 7/6}{n_k^2 + n_k + 1/2}. \tag{3.28}$$

The various m-states are assumed fully mixed by the fluctuations in the direction of the E-field. This means that there always will be $|m| \leq 1$ states to take from.

It is worth noticing that the MHD EOS accounts *explicitly* for houndreds of bound states in each molecule/atom/ion, and does not assume an integrable continuum of hydrogenic states near the ionization energy.

The dissociation of hydrogen molecules is evaluated using the molecular constants found by Herzberg & Howe (1959) and for the H_2^+-ion by use of the data from Vardya (1966). One of the drawbacks of the MHD EOS in connection with this work, is that only these two molecular species are considered.

In contrast to the original EOS (*cf.* Sect. 3.2.1), the MHD EOS is solved by use of the technique known as *free energy minimization* (Graboske et al. 1969; Däppen 1980). The Free energy is the sum of four contributions

$$F(T, V, N_s) = F_{\text{trans}} + F_{\text{int}} + F_{\text{e}} + F_{\text{Coulumb}}, \tag{3.29}$$

the translational free energy assuming that all particles are point particles, the free energy from internal excited states, the free energy of electrons of arbitrary degeneracy and the free energy of Coulumb interactions respectively. The EOS is then solved by minimizing F with respect to the number densities of particles. For ionization of hydrogen for example, we get the stochiometric equation

$$\frac{\partial F}{\partial N_{\text{H}}} - \frac{\partial F}{\partial N_{\text{p}}} - \frac{\partial F}{\partial N_{\text{e}}} = 0 \tag{3.30}$$

and likewise for other ionizations/dissociations. Combining such stochiometric equations with number conservation and charge conservation closes the system.

An outstanding feature of the MHD EOS is the analytical derivatives. First they are used in the Newton-Raphson scheme for solving the EOS, then they are used for evaluating thermodynamical quantities and finally to evaluate thermodynamic derivatives. The basic thermodynamic quantities can be found from the equilibrium free energy, *e.g.* gas pressure

$$P_{\text{g}} = -\left(\frac{\partial F}{\partial V}\right)_{\{N_s\},T}, \tag{3.31}$$

internal energy per unit mass

$$\varepsilon = -T^2 \left(\frac{\partial F/T}{\partial T}\right)_{\{N_s\},V} \tag{3.32}$$

and entropy

$$S = -\left(\frac{\partial F}{\partial T}\right)_{\{N_s\},V} \tag{3.33}$$

(Cox & Guili 1968, Sect. 9.12). This method ensures that the EOS is thermodynamically self-consistent, and satisfies all thermodynamic relations.

The MHD EOS does very well in comparison (Trampedach et al. 1997) with the other leading astrophysical EOS project, the OPAL EOS (Rogers et al. 1996), indicating that the remaining uncertainties regarding the EOS are very small indeed, in particular in the physical regime investigated here.

3.2.3 Discussion

The occupation fractions, as derived from the above two formulations are presented in Fig. 3.1. The first thing to notice is that the atoms typically occupy much less space than is available (indicated with the vertical dotted lines). This result is rather reassuring, as we want the atoms to have room enough for thermal motions. We also note the rather unphysical kink in the curves of de Jager & Neven (1960) as they reach 1, as their theory fails to predict the behaviour of intermediate states.

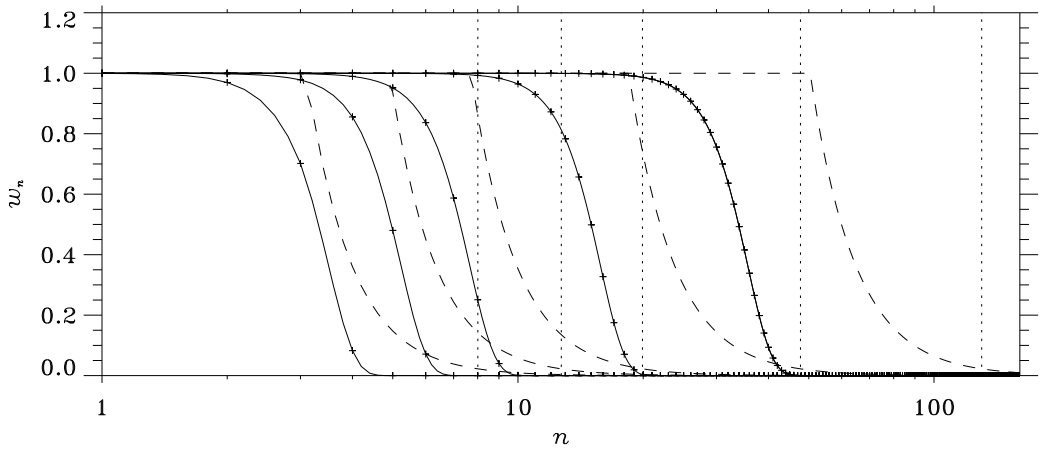

Fig. 3.1: Comparison of the occupation probabilities, as calculated for a hydrogen atom using the MHD EOS formulation (solid line) and the Fischel-Sparks formulation (dashed line). The vertical dotted lines shows n corresponding to the state having a radius equal to the average inter-particle distance. Each of the three curves are plotted for five (T, $\log\varrho$) pairs from the solar simulation: (4427,-8.03), (6891,-6.62), (11520,-6.31), (15240,-5.54), (21920,-4.60), from right to left.

But Gustafsson also used the substitute states of Traving et al. (1966) for the first 10 or so states, implying $w_k = 1$ for $k < 10$ which is clearly not fulfilled for the three inner points in the solar simulation. So Gustafsson's combination of contributions to the partition function is actually self-contradictory — even for the solar case. There is also a counting problem, as u' includes a constant number of states and p, the lowest state included in $u_{\rm as}$, varies with electron density, Eq. (3.21).

Hummer & Mihalas argue that the few percent chance of finding one of de Jager & Neven's atoms to be as large as the average inter-particle distance is very unlikely. Also I find the very long tail, extending far beyond this limit, very worrisome. For comparison, the MHD EOS predicts the chance for encountering an atom this large, to be less than 1 in 10^{200}! Furthermore, Hummer & Mihalas (1988) have recalculated the work of de Jager & Neven in a more direct way, and they get a n^{-12} dependency of the critical field strength, instead of the n^{-4}.

The depression of the continuum, $\Delta\chi$, is not supported by experiments (Wiese

et al. 1972). The observed $\Delta\chi$ is more than an order of magnitude smaller than predicted from Eq. (3.18). The idea of a continuum depression is based on the *static screened Coulumb potential* (SSCP) model of atoms in a plasma, as described by the Debye & Hückel (1923) theory, but Hummer & Mihalas (1988) point out quite a few weak points in employing the Debye & Hückel theory in this way. So both theoretical and experimental results suggest abandoning this concept, which is hereby done.

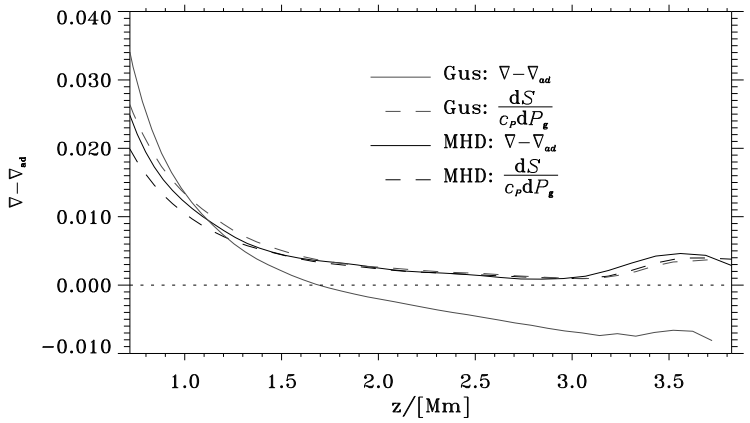

Fig. 3.2: The superadiabatic gradient ∇_s, as calculated from two different expressions and with Gustafssons EOS and the MHD EOS respectively. This plot is for simulations of α Cen A, but is representative for the other simulations too.

The original motivation for changing the EOS, was an observed discrepancy between superadiabatic gradients, as evaluated from two different expressions as shown in Fig. 3.2. The straightforward difference $\nabla - \nabla_{\rm ad}$ gets negative with depth when using Gustafssons EOS, indicating an inconsistency in this EOS. A negative $\nabla_{\rm s}$ would normally mean stability against convection, in marked contradiction with what is observed in the simulations. The $\nabla_{\rm s}$ as evaluated from the entropy gradient, on the other hand, looks more reasonable.

The reason for this thermodynamical inconsistency is the evaluation of pressures and internal energies by Eqs. (3.25) and (3.26). These expressions do not have any contributions from the processes that truncate the partition functions. In the MHD EOS these are automatically and consistently included, as $P_{\rm g}$ and ε are evaluated from the free energy which contains these contributions. The superadiabatic gradients calculated with the MHD EOS are both positive in the convection zone, and are very close to each other. The remaining discrepancy is probably due to both the numerical evaluation of derivative and integrals, and the effect of averaging non-linear fluctuations at different stages (*cf.* Sect. 6 for more details).

The evolution from Gustafssons EOS to the MHD EOS is of course closely linked to the evolution of computer power during the past 20 years, as many approximations

of the former was necessary to obtain reasonable calculation times. Gustafsson's EOS was also developed for *in situ* calculations in the `marcs` stellar atmosphere code (Gustafsson et al. 1975), and furthermore requires a realistic elemental mixture and many molecules, to be suitable as a base for opacity calculations. All this of course put high demands on the calculation speeds. The MHD EOS, on the other hand, was developed for making tables of an high precision EOS and execution time has therefore not been a high priority-issue.

3.3 The Opacity

The interaction between matter and radiation, can proceed in one of two profoundly different ways: absorption or scattering. Absorption is a process which includes energy exchange between photons and particles, thereby permitting the emitted photon to have an energy different from the incoming photon. The energy of the emitted photon therefore depends on the reshuffling by the other particles. Because of this coupling between matter and radiation, absorption processes acts to thermalize the plasma — *i.e.* restore *local thermodynamical equilibrium* LTE, and keep the kinetic temperatures of all the particles equal, and equal to the radiation temperature. The reshuffling is also the statistical process that ensures a Boltzmann distribution of particles and Planck distribution of radiation. There are two types of real absorption processes:

The *bound-free* process is the ionization or dissociation process, where a compound particle (*e.g.* a hydrogen atom being a bound state of a proton and an electron, or a bound state of two hydrogen atoms, forming a hydrogen molecule) absorbs a photon and its energy goes into breaking up the particle, and supplying the debris with kinetic energy. The *free-free* process is a three particle interaction, where a photon exchanging energy with an ion, interacts with an electron in order to conserve momentum. The ff-process can also be understood as photo ionization of an electron in a free, continuum state in the potential of an atom.

The fact that absorption processes involve at least one continuum of states per interaction, is also the reason that absorption processes are thermalizing.

Scattering is a process without energy exchange. A photon excites an electron to an oscillatory state, and is reemitted with exactly the same energy, but in a random direction[1]. If at some wavelength, there is a higher probability for the photon to be scattered than absorbed, the photon can suffer many encounters without being destroyed (thermalized) and it can consequently travel to areas significantly different from where it was created. The scattering process therefore works to decouple the radiation field from the matter. The radiation field no longer follows a Planck distribution, and this will also affect the distribution functions for particles and

[1]Unless situated in a strong magnetic field, in which case the atoms (and therefore also the emission) can get more or less aligned. This might be of some importance for radiative transport in the flux tubes of the solar chromosphere.

alter the ionization or dissociation equilibria. All these effects are known as non-LTE effects.

Non-LTE effects becomes important in the chromosphere and they are responsible for the temperature minimum at 3500 K. This region is in fact covered by the simulations, but we neglect non-LTE effects anyway, in order to render the problem tractable. This is probably the main reason that my simulations do not display any temperature minima. All of the atomic physics in this chapter is done under the assumption of LTE. We have though, allowed for a non thermal contribution to the source function in the radiative transfer. This will be described in more detail in chapter 4.

3.3.1 The bf- and ff-opacity

I use the program by Bengt Gustafsson (1973) to calculate the monochromatic and Rosseland mean opacities. This program is based on a large input file with tabulated absorption coefficients for most of the considered sources and the rest are treated with analytical expressions in the program. As all this was made more than 20 years ago, quite some work has been done on opacities since then and I have therefore updated most of the data tables and added some more metallic sources. The program is very flexible, so it is not a problem to change and expand the data tables, nor is it difficult to add new analytical expressions. All of my changes are included and commented in the list below.

For helium and most of the metallic absorption I use analytical expressions in the form of polynomials in wavelength plus wavelength thresholds for each of the levels considered. For these opacity sources, the listing below only states the number of levels, the excitation- to ionization-potential ratio of the highest level, and the wavelength of its absorption edge. Temperature dependency only enters in the population of the levels, which is evaluated using the classical Boltzmann formula (3.16). As mentioned in Sect. 3.2, the partition function (3.12) contained in the Boltzmann equation, involves a divergent sum over states. As I include only a very limited number of levels, I just take the sum over these levels. The correct thing to do is of course to include the calculation of the level population in the EOS calculation and evaluate the partition function in a physically meaningful *and* consistent manner. A consistency between EOS and opacity calculations is clearly desirable, but it is not within the scope of this thesis, so I will stick to using (3.16) and (3.12) using the numbers of levels stated in the list below.

Most of the updates are based on the compilation by Mathisen (1984), hereafter referred to as Mat1.

H^- Bound-free absorption by the negative hydrogen ion H^-, is updated to the data of Wishart (1979) which are better wavelength sampled, have overall slightly higher values, and are shifted a little to the blue, as compared to the previous data (Doughty et al. 1966). For wavelengths shorter than

1750Å I use the Mat1 compilation of data from Broad & Reinhardt (1976), including the resonance at 1130.5Å.
The free-free absorption by Doughty & Fraser (1966) is replaced by the results of Bell & Berrington (1987) (see Fig. A.1).

HI Absorption by neutral hydrogen is left unchanged (Gustafsson 1973, Eq. (10)) and uses the bf- and ff-gaunt factors calculated by Karzas & Latter (1961). 15 levels are treated explicitly and the rest are treated as a continuum of levels (Unsöld 1955).

HeI 10 levels, $\chi_{\rm max}/I = 0.94$ and $\lambda_{\rm max} =$ 8260Å, from Mat1 p. 20–22.

CI 3 levels, $\chi_{\rm max}/I = 0.24$ and $\lambda_{\rm max} =$ 1445Å, from Mat1 p. 23–24. The analytical expressions are supplied with tables for $\lambda > \lambda_{\rm max}$ (Peach 1967).

NI 3 levels, $\chi_{\rm max}/I = 0.42$ and $\lambda_{\rm max} =$ 1131Å, from Mat1 p. 25–26.

OI Bound-free absorption by oxygen is based on the tables by Hofsaess (1979). From the three pages of tables I just extracted the absorption edges and a few additional guiding points.

NaI 2 levels, $\chi_{\rm max}/I = 0.41$ and $\lambda_{\rm max} =$ 4084Å, from Mat1 p. 28.

MgI 8 levels, $\chi_{\rm max}/I = 0.78$ and $\lambda_{\rm max} =$ 7292Å, from Mat1 p. 29–30.
The ground level bf-absorption is taken from the theoretical work of Mendoza & Zeippen (1987). The analytical expressions are supplied with tables for $\lambda > \lambda_{\rm max}$ (Peach 1967).

MgII 13 levels, $\chi_{\rm max}/I = 0.86$ and $\lambda_{\rm max} =$ 5694Å, from Mat1 p. 31.

AlI 8 levels, $\chi_{\rm max}/I = 0.83$ and $\lambda_{\rm max} =$ 12496Å, from Mat1 p. 32–33.

SiI 9 levels, $\chi_{\rm max}/I = 0.74$ and $\lambda_{\rm max} =$ 5839Å, from Mat1 p. 33–34.
The analytical expressions are supplied with tables for $\lambda > \lambda_{\rm max}$ (Peach 1967).

CaI 3 levels, $\chi_{\rm max}/I = 0.42$ and $\lambda_{\rm max} =$ 3500Å, from Mat1 p. 38–39.

CaII 12 levels, $\chi_{\rm max}/I = 0.82$ and $\lambda_{\rm max} =$ 5686Å, from Mat1 p. 39–40.

FeI 26 levels, $\chi_{\rm max}/I = 0.60$ and $\lambda_{\rm max} =$ 4004Å, from Mat1 p. 40–41 and Sawey & Berrington (1992) blue-wards of 1 150Å.

H+H The bf-absorption by the quasi-hydrogen molecule is left unchanged (Doyle 1968) (see Fig. A.4). This absorption corresponds to the process

$$\mathrm{H} + \mathrm{H} \rightarrow \mathrm{H}_2(^3\Sigma_u^+) + h\nu \rightarrow \mathrm{H}_2^*(^3\Sigma_g^+),$$

where the ungerade state is a repulsive unbound state, and the end product is a hydrogen molecule in the lowest, bound gerade triplet state. The * means that the molecule is excited with respect to the singlet $^1\Sigma_g^+$ ground state.

H_2^+ The bf-absorption by the H_2^+ molecular ion from the photo-dissociation reaction

$$H_2^+ + h\nu \rightarrow H^+ + H,$$

is changed from Mihalas' interpolation (Mihalas 1965) of Bates' semi-classical results (Bates 1952) (extended by Bogges III (1959) and Buckingham et al. (1952)) to the quantum mechanical treatment by Stancil (1994). The absorption by the corresponding ff-process

$$H^+ + H + h\nu \rightarrow H^+ + H,$$

is also taken from Stancil (1994) but this is treated in the semi-classical picture as in (Bates 1952). Stancil's tables generally cover our range of interest better than Bates' (see Fig. A.3).

H_2^- The photo-ionization ff-absorption by the H_2^- molecular ion

$$H_2 + e^- + h\nu \rightarrow H_2 + e^-,$$

was treated using the data of John (1978), but has been changed to those of Bell (1980) which display a larger absorption, particular for low temperatures, and has a somewhat different wavelength dependency (see Fig. A.2). The corresponding bf-absorption from H_2^- is neglible.

OH/CH The photo-dissociation bf-absorption by OH and CH molecules (Kurucz et al. 1987) is included (see Fig. A.5).

H_2O The bf-absorption by water vapour where taken from Mat1's combination of several data sets (see Fig. A.5).

The absorption by H_2 molecules have not been included even though it is the most abundant molecule, as H_2 only absorbs at very short wavelengths. The threshold for photo ionization occurs at 804 Å (Ford et al. 1975), which is below the 860 Å I use for the lower wavelength limit. The absorption due to photo dissociation only occurs in a very small wavelength region and the ground vibrational state, $\nu = 0$ falls below the 860 Å. Only $\nu \geq 1$ states have thresholds above this and only $\nu \geq 3$ states have thresholds above the Lyman limit. Even the $\nu = 10$ state has its threshold at a short 1147 Å. The absorption coefficient for each state is about $1\text{-}8{\cdot}10^{-18}$ cm^2 per molecule, but has a three orders of magnitude dip around 980 Å (Allison & Dalgarno 1969).

3.3.2 Scattering by Electrons

The scattering of photons by free electrons is (unchanged)

$$\sigma_{\mathrm{T}} = \frac{8\pi}{3}\left(\frac{e^2}{m_{\mathrm{e}}c^2}\right)^2, \tag{3.34}$$

the *Thomson scattering*. This is a purely classical expression, and one could of course include the relativistic and quantum-mechanical corrections, but it can hardly be of any importance what so ever.

The scattering by bound electrons — the *Rayleigh scattering*, is changed to

$$\sigma_{\rm Ray} = \sigma_{\rm T} z^2 \max\left(1, \left(\frac{A}{\lambda}\right)^4 \left[1 + \left(\frac{B}{\lambda}\right)^2 + \left(\frac{C}{\lambda}\right)^4 + \left(\frac{D}{\lambda}\right)^8\right]\right) \qquad (3.35)$$

where z is the number of electrons in the scattering system. At small wavelengths the energy of the incident light is much larger than that of the electrons, and the electrons respond as if they were free. The max-operator in (3.35) makes sure that the short-wavelength behaviour is right, though it cuts out all the resonances. The red-ward wings of the resonances are taken care of by the terms in the square

Table 3.2: Parameters for Rayleigh-scattering.

name	A	B	C	D	z
He	379	678	674	735	2
H_2	756	1380	35	1422	2

brackets of (3.35) and the remaining part of the resonances are just ignored with this formula.

Equation (3.35) is used for Rayleigh scattering by H_2 and He, whereas atomic hydrogen, the strongest and most abundant scatterer, is treated in somewhat more detail, as described in App. B. The parameters for He and H_2 are listed in Tab. 3.2 and are derived from Mat1. For He the parameters are fit to calculations by Langhoff et al. (1974) and for H_2 a fit to experiments (Victor & Dalgarno 1969). Both fits work over the entire range of wavelengths given in the references — rather better than the fits stated in Mat1 (Fig. B.2).

3.3.3 Line opacity

For a long time the line opacities have been neglected or at most treated very rudimentary in calculations of Rosseland mean opacities, assuming that the lines are so thin that they only contribute neglible to this harmonic mean. The lines do nevertheless contribute significantly, due to a variety of effects not appreciated in earlier opacity work. The term splitting due to internal Stark and Zeeman effects in the atoms/ions, and pressure (Stark) broadening by fields from passing ions/electrons, are very efficient in increasing the accumulated width of the lines (Iglesias et al. 1992; Rogers & Iglesias 1994). In this way, the lines can actually fill out wavelength regions, especially if the continuum opacity is low. As the lowest opacity is decisive for a Rosseland mean, this can be rather important.

This of course only pertains to modelling of stellar interiors, where radiation transport can be evaluated in the diffusion approximation fully described by a Rosseland average. For atmosphere calculations, on the other hand, the effect of lines has been taken account of for the last 30 years or so by various approximate methods. The presence of millions of lines, especially in the UV, will block the flux in these wavelength regions. This is referred to as *line blocking* or *line blanketing*, and forces the flux to redistribute to less blocked wavelengths (See Sect. 4.1 for a more detailed description). The temperature structure in a stellar atmosphere can be severely affected by line absorption.

Opacity distribution functions.

The sheer number of lines needed to reproduce the radiative transfer in stellar atmospheres adequately, forces a statistical approach to the treatment of lines. There

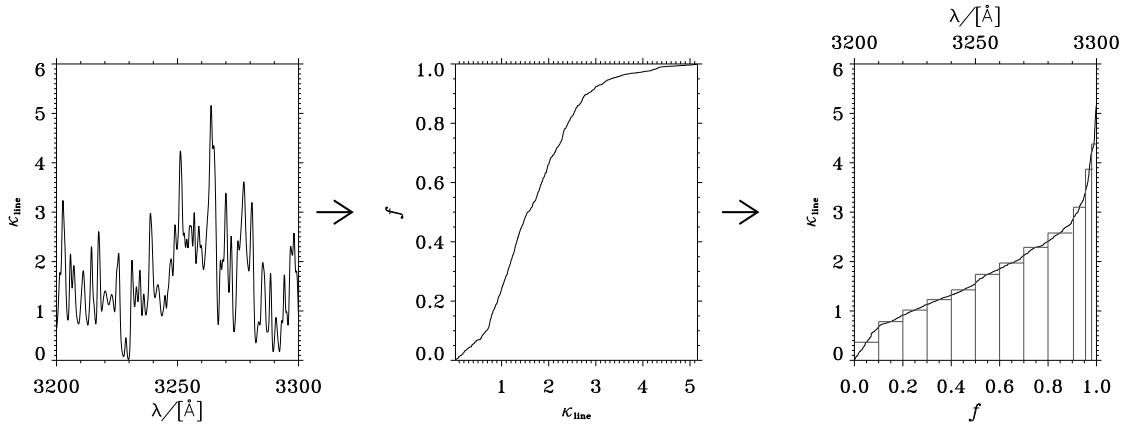

Fig. 3.3: This figure shows the idea behind the ODF method. First the distribution of opacities in the selected wavelength interval, is translated into a distribution function, f, and then f is inverted and mapped on the wavelength interval and sampled at the triangulation points, to obtain the giant line.

are now two methods in widespread use; The opacity distribution function (ODF) adopted here, and the opacity sampling (OS).

The ODF method is based on the full monochromatic opacity. The wavelengths are divided into a number of intervals, and for each interval, is then calculated the distribution of line opacities, $f(\kappa_{\rm line})$. The method is illustrated for a single such wavelength interval in Fig. 3.3. The distribution function (being monotonic) is then inverted, and a number of f-points is chosen for sampling $\kappa_{\rm line}(f)$, the so-called triangulation points. By ascribing wavelengths to the triangulation points, the ODFs can now simply be added to the rest of the opacity and treated accordingly in the radiative transfer. ODFs are also, quite naturally, referred to as *giant lines*.

The usage of ODFs rests on the assumption that the source function is constant

over each wavelength interval. This assumption is easily satisfied by choosing sufficiently small wavelength intervals. The distinction between continuous- and line-opacity also introduces the assumption of constant continuous-opacity over each of the wavelength intervals. An bf-absorption edge in the middle of a giant line, of course breaks this assumption, which is one of the reasons for me to suggest the calculation of total ODFs including all kinds of absorption (See p. 41) and then just calculate the scattering separately.

There is also a more serious limitation on the validity of the ODF approach. The wavelength dependency of the ODFs are always roughly the same, independently of depth in the model. High opacity and low opacity will always be at the same wavelengths, which is not always the case in the real world. A wavelength of a molecular line will have large absorption in the outer parts of the model, whereas wavelengths corresponding to atomic and ionic lines will have high absorption at increasing depth. Radiation at the former wavelength will be severely impeded at great heights, contributing to the heating here, whereas radiation at the latter wavelengths will escape freely from lower in the atmosphere. If within a given giant line, there is a mixture of atomic and molecular lines, the ODF method will therefore overestimates the line-blocking, and can lead to a wrong temperature stratification.

The OS method is the Monte-Carlo approach to the problem (Petreymann 1974; Sneden et al. 1976). The opacity is evaluated at a number of random, but fixed wavelength points. In this way, the problem of the position of the high opacity regions is circumvented. The variation of the opacity with depth in the model, will be the true and physical variation, contrary to the ODF approach.

Another nice feature of the OS method, is the linearity with opacity sources. The OS can be tabulated for each element and then added together for any desired compositions, and new opacity sources can be added without recalculating everything. The most precise and computationally cost efficient method would be to use pre-tabulated total OS, including all opacity sources, and then calculate the scattering separately. A change to the OS method in this way is desirable, but not within the scope of this work.

In Fig. 15 and 16 of their article, Gustafsson et al. (1975) compares their ODF atmospheres with the OS atmospheres of Petreymann (1974).

Gustafssons ODFs

The original ODFs Gustafsson (1973), consist of 42^2 giant lines in the wavelength region 3 000–7 200Å, each 100Å wide and with four quadrature points. These ODF-data are given for 9 temperatures between 3 000 and 9 000K and 15 electron pressures: $P_e = 10^{-3}$–10^4dyn cm^{-2}. The ODF-data are interpolated linearly in equidistant logarithmic temperatures and electron pressures, and are given as logarithmic relative opacity, normalized to the 5 200Å continuum opacity.

[2]See (Adams 1989a, chapter 27) for a discussion of the significance of this particular number.

The giant lines are turned back-to-back in order to prevent an artificial bluening of the model. By this procedure the pairs of giant lines in fact resembles some very large lines, instead of the normal sawtooth function. Due to the lack of line-data for wavelengths shorter than 3 000Å and as there is still an appreciable amount of flux coming from this UV region, the two bluest giant lines, have somewhat arbitrarily been copied to the 2 076–3 000Å region.

The ODF-data are based on some 50 000 atomic lines and a somewhat larger number of molecular lines from MgH, CH, OH, NH and CN molecules. To obtain better agreement with observed spectra of the Sun and Arcturus, it was found necessary to add some lines in the UV.

For $\lambda > 7\,200$Å only line absorption from CN and CO molecules are considered (including isotopic shifts due to the presence of both C^{12} and C^{13}). These line data are summed up into 23 giant lines for CN and CO separately and are given as logarithmic relative line opacity per molecule. In this way the ODF-data need only be a function of temperature and the number densities of the molecules can be supplied at run-time. The two sets of giant lines are combined by turning the giant lines of CN one way and those of CO the other way, assuming a minimum of correlation between the actual CN and CO lines. The line blanketing is of course overestimated in this way, but the CN lines are fairly weak anyway, so it cannot be that far off. These ODFs cover the wavelength range from 7 200 to 125 000Å and are given for 6 temperatures from 2 000K to 7 000K.

Kurucz' ODFs

My update of opacities include a change of ODFs, to the ones of Kurucz (1992c) (*cf.* Fig. 3.4). They are available in two resolutions, and I have chosen the coarse set with 328 giant lines, of which I only use the 230 between 860 and 200 000Å. Each line has 12 triangulation points so the lines are much better resolved than with Gustafssons ODFs. The ODFs are given on a grid of 56 temperatures and 21 gas pressures with linear interpolation between logarithmic quantities. Kurucz' ODFs give absolute line opacities, as opposed to Gustafssons which are given relative to the continuum. I use the ODFs with microturbulent velocities of $2\,\mathrm{km\,s^{-1}}$.

Changes in abundances can only be done in one dimension, by changing the metal to hydrogen ratio [Fe/H], as Kurucz assumes the solar helium to hydrogen ratio [He/H] to be fixed (and known?). Fortunately I have found an ODF-file for solar metallicity, but without any helium, making it possible to interpolate in two dimensions: $X, Z, Y = 1 - X - Z$, as described in Sect. 3.3.4. This does not give many points to interpolate between in Y, but He has a few features that makes this interpolation less unsafe. First of all, the opacity contribution from He is insignificant in the stellar atmospheres considered here, as can be seen from Fig. A.7. Second, He is a very poor electron donator due to the high ionization potential, and the influence on the H^-–ion balance is therefore very small. Helium is a very inactive element, and its main effect is to displace some hydrogen and metals.

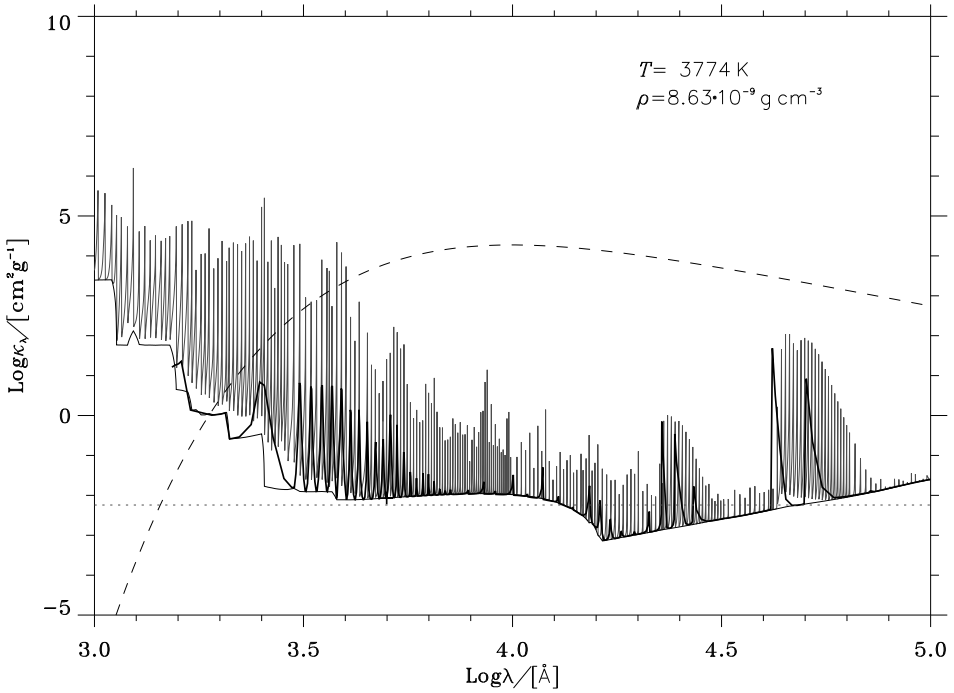

Fig. 3.4: The monochromatic opacity at a point in the solar simulation. The thin solid line is the continuum, and the thick solid line shows Gustafssons ODFs, whereas the grey line depicts Kurucz' ODFs. There is clearly much more line blocking with Kurucz' ODFs.

Kurucz' ODFs are the result of including 58 000 000 lines from atomic and molecular transitions (Kurucz 1992a). The latter from both electronic, rotational and vibrational transitions of a wealth of diatomic molecules. No triatomic molecules are included, but that should not matter, as I am only dealing with F and G stars. For K and M stars (Alexander et al. 1997) also tri- and polyatomic molecules as well as dust formation, starts to play a significant role for the opacity (Alexander & Ferguson 1994).

The atomic lines include 66 800 lines from atoms lighter than Ca, 38 500 lines of atoms heavier than Ni and 42 000 000 lines from the first nine ions of the iron group elements, Ca through Ni. Many of the iron group lines are predicted lines and Kurucz has in this way been able to extrapolate to the hundreds of thousands of weak lines, predominantly from transitions between highly excited states, supposed to add up to an efficient source of line-blocking in the UV. This, however, turns out not to be the case. These weak lines have a neglible influence on the flux distribution according to Bell et al. (1994), and the missing UV opacity is more likely to come from bf-processes — a suggestion also advocated by Lester (1996). Most of Kurucz gf-values are theoretical because of the quite limited experimental data available, but some of these extrapolated lines, especially in the UV, have oscillator strengths

that are too large to explain any lines in the solar spectrum (Bell et al. 1994). On a coarse wavelength scale though (as used for his ODFs) the emergent flux from his `atlas9` atmosphere models, do very well in comparison with observations (Kurucz 1992b; Castelli & Kurucz 1994). In view of the above discussion, this agreement is probably due to the right combination of underestimated continuum opacity and overestimated line opacity.

One can argue that this is just another fudging of *physical* opacities to obtain *astrophysical* opacities. The previous version of `tabcmp`, using Gustafssons ODFs, in fact used an ad hoc enhancement of the UV opacity (Magain 1983; and below) to agree with the observed solar flux, as well as with UBV colours of other stars of luminosity class V, with temperatures in the range $5\,250\,\mathrm{K} < T_{\mathrm{eff}} < 7\,000\,\mathrm{K}$.

I better like using the slightly doubtful ODFs of Kurucz, than the combination of Magain's opacity enhancement and Gustafssons ODFs, as the latter are rather arbitrary and unconstrained by observations for wavelengths shorter than 3 000 Å. Also Kurucz' exaggerated lines are at least due to a broad range of physical ions, and just add normally to the rest of the opacity, independently of what this rest looks like. Finally my personal taste also plays a role here, as I find that using Kurucz' ODFs is more in the *ab initio* spirit of this thesis, as is the usage of Magain's opacity enhancement.

Magain's UV-opacity enhancement

The idea of Magain's prescription (Magain 1983) is to model the missing UV-opacity, as stemming from an excited state ($\sim 3\,\mathrm{eV}$) of neutral iron. The emerging flux difference between a solar model using Gustafssons ODFs, and observations, is translated into an opacity difference, to infer the wavelength dependency, $k(\lambda)$. This $k(\lambda)$, is then multiplied with the number of iron atoms in the fictious, 3 eV, average-excited state. It is worth mentioning, that $k(\lambda)$ is rather continuous, but can just as well be a veil of weak metal lines, as it can be bf-absorption from various metals. It is though, not coming from a number of strong lines.

The $k(\lambda)$ actually used in the previous `tabcmp`, is just linear in λ (below λ=5 000 Å), and in fact misses a lot of opacity in the 3 300-4 000 Å region, compared to Magain's original version. Below 3 300 Å, $k(\lambda)$ is undefined due to lack of observations at that time, so $k(\lambda)$ was just extrapolated to shorter wavelengths. As Gustafssons lines in this region was also just an extrapolation (See above), the combination of Gustafssons ODFs and Magain's opacity enhancement is rather dubious in the extreme UV (EUV).

One of the assumptions behind the temperature dependency, is that the continuous opacity is predominantly due to the H^--ion. For wavelengths short ward of about 4 000 Å, this is not the case for any temperatures in the Sun (*cf.* Fig. 3.6-3.8). Whether this is important or not, is not easily judged, and agreement with observations is of course more important than agreement with this simple assumption. Magain compares his results with observations in various colour-colour diagrams of

UBV colours, but as the U band only goes down to 3 000 Å, discrepancies in the EUV will not show up on such diagrams. Only a colour-magnitude diagram will show the difference, as an erroneous flux in the EUV will be compensated equally in both U, B and V.

bf versus bb

A lot of the lines included in Kurucz' ODFs are actually resonances from bf-transitions, apparently autoionizing lines, but this is not described very well by Kurucz and does deserve a few comments. Looking at various bf-absorption coefficients from the Opacity Project, one soon realizes that the notion that continuous- and line opacity, distinguishes between bb- and bf-absorption is rather malplaced, and it is important to distinguish between bf- and continuous absorption. The bf-absorption namely turns out to have numerous resonances of all thinkable shapes and sizes (See Fig. 3.5). The widths of these resonances span from normal line widths to hundreds of Ångstrøms, and their heights can easily be orders of magnitude higher (or lower) than a somehow smoothed background absorption, making it very hard to come up with a reasonable choice for a continuum opacity. This is of course mostly the

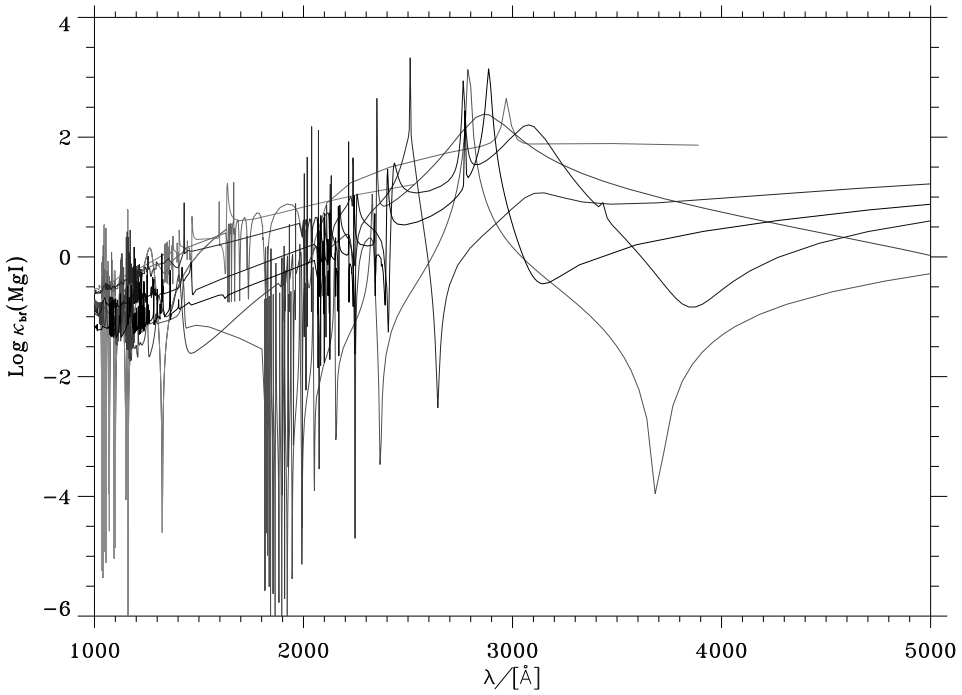

Fig. 3.5: An example of bf-absorption, as calculated by the OP team. These data have been retrieved from the electronic OP data-archive (Cunto & Mendoza 1993). The plot shows the bf-absorption for the first 8 levels of MgI, having excitation energies below 6 eV (Butler et al. 1993).

case for ionization from lower states in many-electron atoms and ions, and these resonances are therefore most common in the UV. This situation makes it very easy to mix up bf- and bb-opacity in the UV, and though broad band fluxes might turn out right, a detailed spectrum will certainly look wrong with a wrong weighting between continuum and lines (Lester 1996). To solve the problem consistently, I would like to suggest the calculation of total ODFs (or OS-data), including both bb- and bf-absorption, on an equal footing and with the same wavelength resolution and including Doppler broadening by micro turbulence. If then a continuous opacity is needed, it can be found (observed) as the low opacity triangulation point of each giant line.

The complexity and remaining uncertainty regarding line-data, can be illustrated by a recently published multiplet table for FeI (Nave et al. 1994). In this article, 28 new energy levels are added to previous work, making a total of 846 levels. The extensive and widely used tables of Moore (1952b; 1959) contains identification of about 5 500 lines. With the work of Nave et al. this has increased to 9501 lines covering the 1 700 Å to 5μm region, with the biggest increase occuring in the ultraviolet ($\sim$ 1200 new lines) and the infrared ($\sim$ 3000 new lines). Only a few of the lines in these regions (below 3 000Å and beyond 1μm) have measured oscillator strengths. Brown et al. (1988) investigated the 1 550–3 215Å region and found 800 lines below 1 700 Å and many of the lines above were not in common with Nave et al.'s findings due to different types of experiments and therefore different populations of highly excited levels.

In view of this, the iron line opacity is still a very unsettled matter, and a lot of work remains on both line identification and measurements of oscillator strengths. Many fairly strong lines observed in both solar spectra and in the laboratory are still unidentified.

3.3.4 The total opacity

Adding it all together

The continuous opacity is evaluated once for each giant line, and is interpolated linearly in wavelength and absolute opacity within a giant line. Each giant line then samples this linearly interpolated continuous opacity at the 4, 8 or 12 quadrature points. Some of my new sources of continuous opacity, have some very sharp resonances and wavelength resolution then becomes a significant issue. For that reason the resonant features in the H^- and MgI bf-absorption has been truncated or left out (*cf.* Fig. A.1 and A.6).

The ODFs used together with Gustafssons opacities, are calculated for exactly the same abundances as they have been used for, as my first simulations was with the abundances suggested by Gustafsson (*cf.* Tab. 3.1). Kurucz's ODFs on the other hand, have slightly different abundances so I therefore had to decide on an interpolation scheme. I use a log-log interpolation assuming that a power-law is a

good approximation locally. As a measure of abundances I do not use the normal weight-fractions or number fractions, but the hybrid: numbers per mass, as that is what determines an opacity per mass. The interpolation is performed between three tables; Kurucz's [Fe/H] = 0.0, [Fe/H] = −0.1 and [Fe/H] = 0.0 without He. For Gustafssons mixture this results in the linear combination (65%, 37%, -2%) of the three tables respectively, and for the mixture I have chosen as solar: (38%, 49%, 13%).

Results

The result of summing all the opacity sources is presented in the figures 3.6–3.8, for various parameters T and ϱ corresponding to three points in a typical averaged snapshot of the solar simulation. In the two first figures, corresponding to the temperature minimum and the photosphere respectively, we see a very characteristic round bump, centered just below Logλ = 4.0. This feature is the bound-free absorption from the H^--ion (cf. Fig. A.1), and it is a dominant source to the Rosseland mean opacity in the atmospheres of all F, G and K stars. To the red of this we see the combination of free-free absorption by the H^--ion, and as temperature rises, also the bound-free absorption from the higher levels of neutral hydrogen as well as some free-free absorption by hydrogen. To the blue of the H^--bump, we see a lot of bf absorption edges from various metals. In Fig. 3.6, going from blue to red, we have first the large Balmer jump, arising from ionization from the ground state of hydrogen. Then comes the ground state carbon absorption edge. On the next plateau we see a small peak, which is the first resonance in the Rayleigh scattering by hydrogen (cf. Fig. B.2). The next two absorption edges comes from the ground state and first excited state of silicium and also the ground states of iron and magnesium contributes here, as well as the two peaks from the calcium ground state. The large edge at the end of this rugged plateau is supplied by the ground state of aluminium and after that we have an even larger edge from the first excited state of magnesium. Also the next edge is from magnesium; the second excited state with its resonance (truncated, see Fig. A.6) showing up, as the small bump in the middle.

In Fig. 3.6 it is also evident how the huge amount (tens of millions) of thin metallic lines seriously can alter the opacity. Between 1 500 and 4 000Å the lines define a effective continuum that is up to an order of magnitude larger than the real continuum. The two prominent line features in the infrared, are the absorption bands of CO molecules, where the reddest band with bandhead at 41 832Å is the fundamental mode, the first overtone has its bandhead at 22 760Å and the second overtone at 15 331Å, well hidden in the H^- bf-absorption. The band of lines arises from the closely spaced rotational levels, and the different bands and the tones mentioned above, refer to different vibrational levels.

In Fig. 3.7 we have moved inward to a point in the solar photosphere and we clearly see the effect of increasing the temperature; the ff-absorption and bf-absorption from highly excited states have increased considerably and the molecular

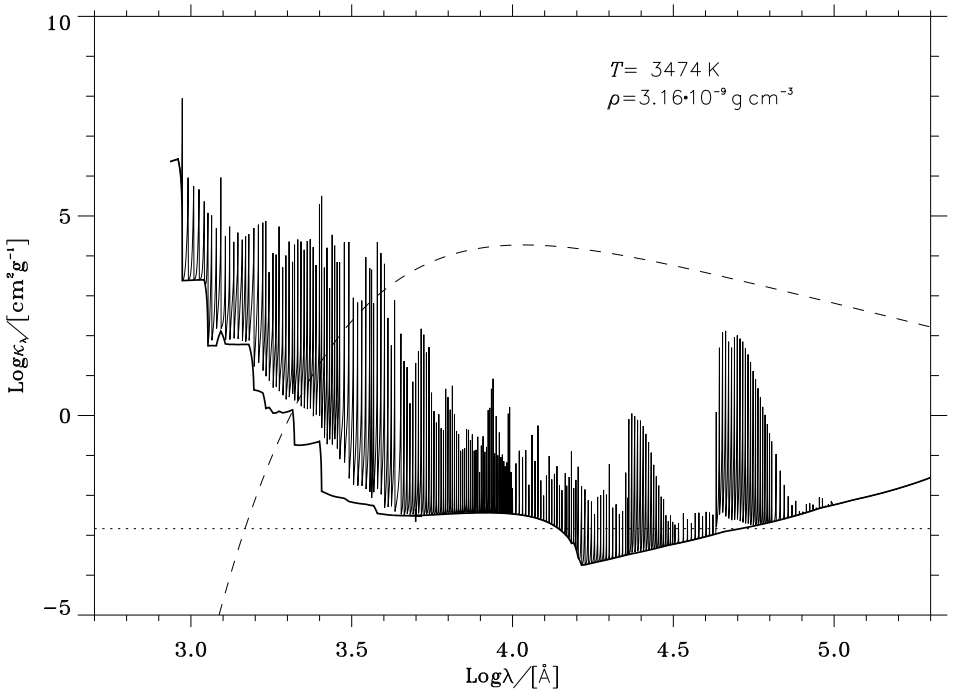

Fig. 3.6: The calculated opacity for $T = 3474$K and $\varrho = 3.16 \times 10^{-9}$gcm^{-2}. The thick solid line is the continuum opacity, as commented on above, the thin solid line is the full opacity including the line opacity from the ODFs. The dashed line is the Rosseland weighting function and the dotted line is the Rosseland mean value. I have also marked the 5000 Å continuum opacity with a thick cross (at Log$\lambda \simeq 3.7$).

bands from CO have disappeared. Apart from what can be seen in Fig. 3.6, we also see the first two excited states of carbon, on either side of the Rayleigh scattering resonance, emerging from the receding aluminium ground state absorption. We also see the Balmer limit at 3 647Å although it almost coincides with the MgI second excited state absorption edge at 3 757Å.

Fig. 3.8 is, in many respects, very different from the two preceding ones. First of all, we notice the total lack of H^- bf-absorption and the dominance of bf-absorption by highly excited states of hydrogen. The little hump, just to the red of the Lyman limit, is ground state carbon absorption, but apart from that, no metals can be seen. A very obvious reason for this, is of course that I have only included two ions in my continuous opacity calculations, the MgII and the CaII ions. At temperatures above 10 000K all elements except He and Ne, are at least partly ionized. It is therefore a bad approximation to neglect these ions. The reason I do it anyway, is that at these temperatures we are deep down in the convection zones of the stars I investigate in this work, hence the opacity do not have any effect on the models.

Another peculiar thing is the behaviour of the lines. There are almost no lines left, and those left, are almost exclusively hydrogen lines. The very large line widths

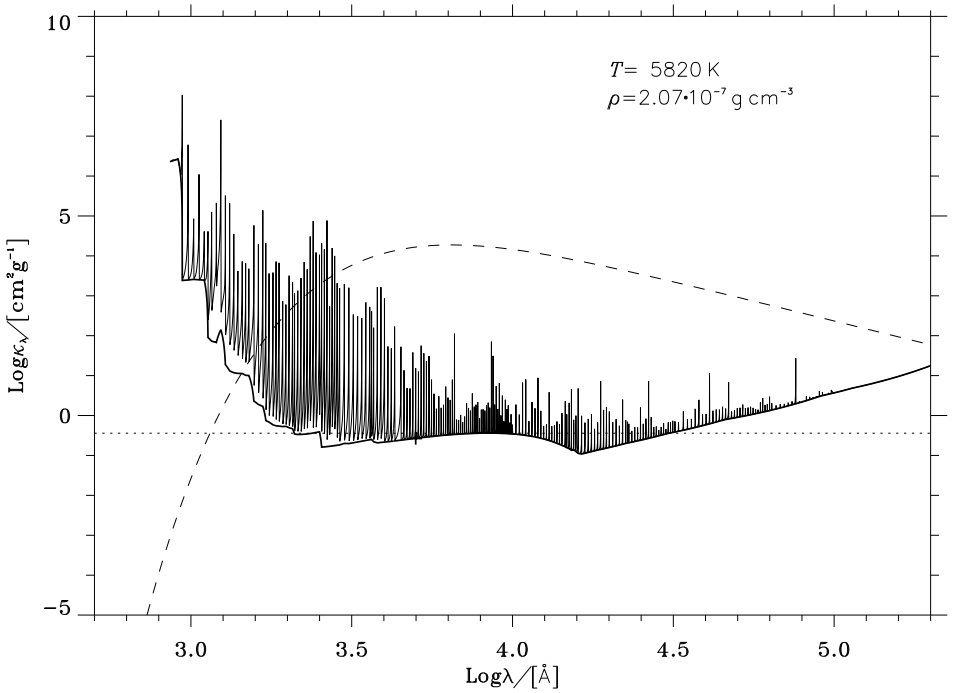

Fig. 3.7: The same as in Fig. 3.7, but this time for $T = 5820$K and $\varrho = 2.07 \times 10^{-7}$, corresponding to a point in the photosphere.

are due to pressure broadening or collisional broadening, which is much more efficient in broadening the line wings than the core. As we, going through these three figures, have increased the temperature with one order of magnitude, and the density with more than 4 orders of magnitude, the dominant line-broadening agent has shifted from Doppler-broadening to pressure broadening. As Doppler broadening consists of folding the line with a Gaussian, the linewings are not enhanced by this process, whereas pressure broadening contributes directly to the width of the Lorentzian (the combination of the two being the well-known *Voigt-profile*).

The orientation of the ODFs, gives these broadened lines a strange look, but reversing the ODF-lines to the red of a line centre, results in some smooth linewings. A thing worth noticing in this figure, is the merging of lines near an absorption edge. This is most clearly seen for the Lyman lines, whose wings form a smooth continuous transition to the otherwise sharp absorption edge.

Fig. 3.9 summarizes the effect of all the above changes I have made to the opacities. As the need for an update of the opacities was noticed, in a comparison with Kurucz' opacities (Kurucz 1992b), I'll stick to this and also compare my updates with Kurucz. The figure presents ratios between Kurucz Rosseland mean opacities and different levels of updates on the opacities I use, along a ϱ/T-track typical for horizontally averaged simulation of the Sun.

In order to separate the different effects, I have first calculated a version with

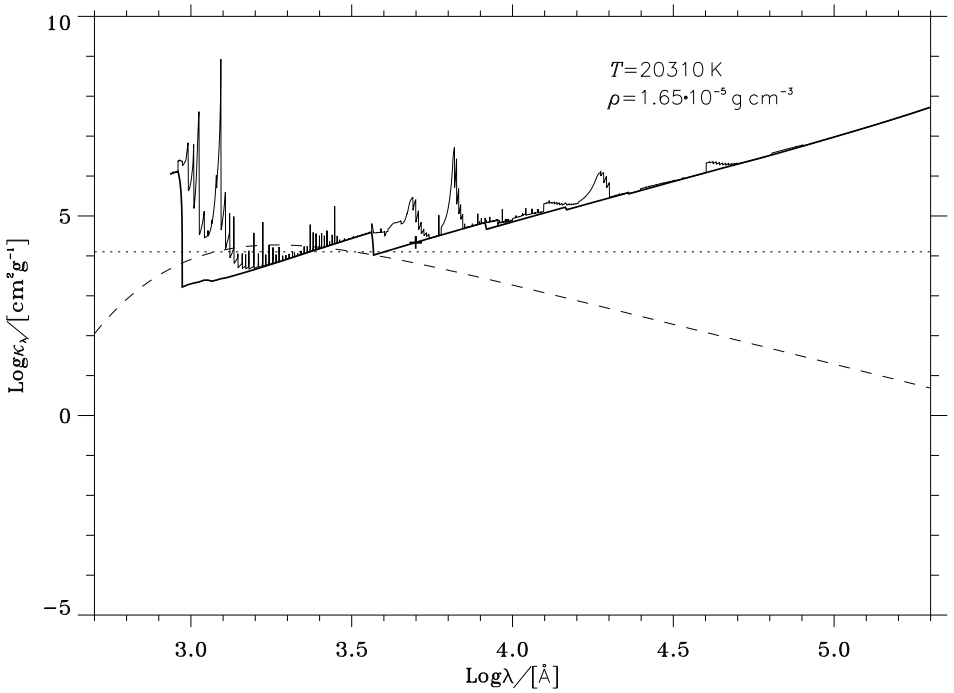

Fig. 3.8: The same as in Fig. 3.7, but this time for $T = 20\,310$K and $\varrho = 1.65 \times 10^{-5}$, close to the deepest point in my simulation of the Sun.

the full update, that is, the current version of the opacities. This is represented by the upper solid curve that wiggles nicely around 1, for Log$T \lesssim 4.1$. Then I have calculated opacities with each of the updates changed back to the old version – always one at a time, to single out the effects.

The discrepancy above Log$T \lesssim 4.1$, is due to the lack of ions in my continuous opacity calculations. The strongest absorber missing in my calculations, is the C^+-ion which just starts to dominate over atomic carbon at 10 000K.

The lowermost solid curve shows the effect of totally ignoring line opacity, so it is actually not illustrating an update. I included it to show the large impact that line absorption has on a Rosseland mean. For this ϱ/T-track, we find the smallest impact at Log$T \simeq 3.6$ where the opacity is "only" raised by a factor of 1.25, and we can see that the lines adds up to 50% to the Rosseland mean.

3.4 The table program

The convection code is completely decoupled from the EOS and opacity issues, in that it calls a autonomous program (`tabcmp`) for making tables of the EOS and opacity, suitable for the convection code. This table just spans the ϱ/T-area covered by a snapshot of the simulation plus margins in both parameters. Such a table

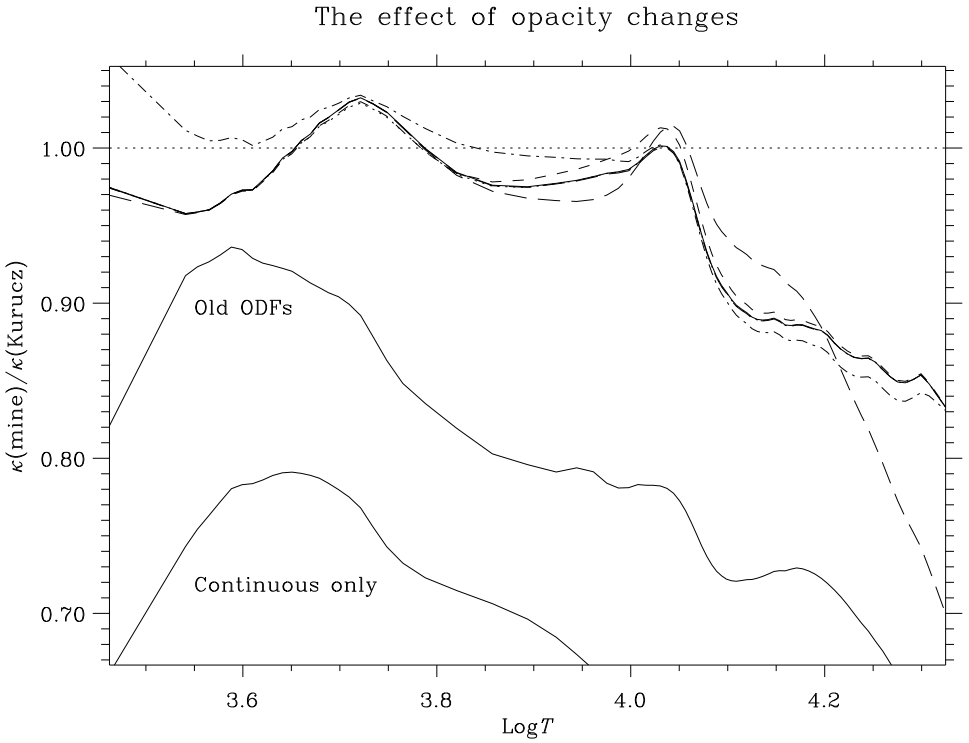

Fig. 3.9: This figure shows the effect of the various changes I have made to the opacity. The ratio between my opacity and Kurucz' are plotted against logarithmic temperature through a typical mean model of the Sun. The lower solid curve shows this ratio if only the continuous opacity is included (to show the large impact of line opacity). The solid curve in the middle is calculated with the old ODFs and therefore also the old wavelength interval. The upper solid line is for my opacity calculations including all the changes mentioned above. I also plot ratios using the old hydrogen (H, H^-, (H+H), H_2^- and H_2^+) opacity (dot-dash), old heavy element opacity (short dashed), and without CH-, OH-, and H_2O-molecules (dotted). The latter can only be seen around the peak at Log$T \simeq 3.72$, where it merges with the dashed "old heavy element opacity"-curve to give a dot-dashed line. Running short of linestyles, I have used long-dashed lines for two types of changes; Below Log$T \simeq 3.6$, the long-dashed line is the result of using the old version of Rayleigh scattering and at higher temperatures, the long-dashed line comes from using the old (shorter) wavelength interval.

is of course far from rectangular but it is very efficient for obtaining the highest resolution at the least memory expenditure. When the simulation occasionally makes excursions outside the table boundaries, the convection code automatically makes `tabcmp` expand the table.

`tabcmp` is developed specially for the convection code and is just an interface between the convection code and the EOS and opacity routines. The latter have till now, been supplied by Gustafsson (1973), but I have for several reasons decided to

update both the EOS and the opacities, as described below.

The tables are first calculated as functions of T and ϱ, but as T is not contained explicitly in any of the Navier Stokes equations, (2.4)-(2.6), whereas internal energy per mass, ε is, the tables are inverted into tables containing variables as functions of ε and ϱ. The final tables contain the quantities, $P_{\rm g}$, $\ln\kappa\varrho$, T and the four binned pseudo Planck functions (*cf.* Sect. 4.2, Eq. (4.23)), as well as their derivatives with respect to ε and ϱ. The differentiation with respect to ε is evaluated with cubic splines (Sect. 2.4.1), whereas the ϱ derivatives are just linear derivatives, assuming that the ϱ dependency of any of the tabulated quantities is much more moderate than the ε dependency. This means that I do not exploit the analytical derivatives of the MHD EOS. This is rather unfortunate and a change to interpolation routines which makes use of both the absolute quantities and their derivatives in a consistent way, is desirable — not only for this work.

3.5 Thermodynamics

After having calculated a table as described in Sect. 3.4, the various thermodynamic quantities can be evaluated via the derivatives contained in the table (See *e.g.* Cox & Guili (1968), Kippenhahn & Weigert (1990) or Christensen-Dalsgaard (1991)).

I use two of the adiabatic exponents:

$$\Gamma_1 \equiv \left(\frac{\partial \ln P_{\rm g}}{\partial \ln \varrho}\right)_S = \left(\frac{\partial \ln P_{\rm g}}{\partial \ln \varrho}\right)_\varepsilon + \frac{P_{\rm g}}{\varrho}\left(\frac{\partial \ln P_{\rm g}}{\partial \varepsilon}\right)_\varrho, \tag{3.36}$$

which goes into calculating the adiabatic soundspeed

$$c_{\rm s} \equiv \sqrt{\Gamma_1 \frac{P_{\rm g}}{\varrho}}, \tag{3.37}$$

and

$$\Gamma_3 = \frac{P_{\rm g}}{\varrho}\left(\frac{\partial \ln P_{\rm g}}{\partial \varepsilon}\right)_\varrho + 1, \tag{3.38}$$

used in the calculation of the adiabatic temperature gradient

$$\nabla_{\rm ad} \equiv \left(\frac{\partial \ln T}{\partial \ln P_{\rm g}}\right)_S = \frac{\Gamma_3 - 1}{\Gamma_1}. \tag{3.39}$$

Whether the turbulent pressure should be included in some way in $\nabla_{\rm ad}$ is unsettled, and I will therefore just use this purely thermodynamic definition. The specific heat at constant pressure is

$$c_{P_{\rm g}} \equiv \left(\frac{\partial H}{\partial T}\right)_{P_{\rm g}} = \left[1 - \frac{P_{\rm g}}{\varrho}\left(\frac{\partial \ln \varrho}{\partial \varepsilon}\right)_{P_{\rm g}}\right]\left(\frac{\partial T}{\partial \varepsilon}\right)^{-1}_{P_{\rm g}}, \tag{3.40}$$

where

$$\left(\frac{\partial \ln \varrho}{\partial \varepsilon}\right)_{P_{\rm g}} = -\left(\frac{\partial \ln P_{\rm g}}{\partial \varepsilon}\right)_{\varrho}\left(\frac{\partial \ln P_{\rm g}}{\partial \ln \varrho}\right)_{\varepsilon}^{-1} \tag{3.41}$$

and

$$\left(\frac{\partial T}{\partial \varepsilon}\right)_{P_{\rm g}} = \left(\frac{\partial T}{\partial \ln \varrho}\right)_{\varepsilon}\left(\frac{\partial \ln \varrho}{\partial \varepsilon}\right)_{P_{\rm g}} + \left(\frac{\partial T}{\partial \varepsilon}\right)_{\varrho}. \tag{3.42}$$

The enthalpy, H, is

$$H \equiv \varepsilon + P_{\rm g}/\varrho. \tag{3.43}$$

The specific heat at constant volume is

$$c_V \equiv \left(\frac{\partial T}{\partial \varepsilon}\right)_{\varrho}^{-1}. \tag{3.44}$$

Chapter 4

The radiative transfer

The main reason for the complications arising near the surface of stars is the interaction between radiation and matter (Nordlund 1985; Nordlund & Dravins 1990). The largest inhomogeneities occur in the same layers where we have the transition from convective to radiative energy transport and, furthermore, it is the region where matter gets optically thin resulting in the breakdown of the diffusion approximation in the radiation transfer. This latter obstacle really complicates the calculations a great deal and evaluation of the radiative transfer takes up 25-50% of the computing time.

The radiative heating of the gas may be expressed as the difference between absorption and emission as in (2.7), or may be rewritten as

$$Q_{\mathbf{rad}} = 4\pi\varrho \int_\lambda \kappa_\lambda (J_\lambda - S_\lambda) \mathrm{d}\lambda, \tag{4.1}$$

where the mean radiation intensity, J_λ, is

$$J_\lambda = \frac{1}{4\pi} \int_\Omega I_\lambda(\Omega) \mathrm{d}\Omega, \tag{4.2}$$

and I_λ is related to the source function by

$$\frac{\mathrm{d}I_\lambda}{\mathrm{d}\tau_\lambda} = I_\lambda - S_\lambda, \tag{4.3}$$

where the monochromatic optical depth, along a ray inclined at an angle θ to the surface normal, is defined by

$$\mathrm{d}\tau_\lambda = \varrho\kappa_\lambda \sec\theta \, \mathrm{d}z. \tag{4.4}$$

Realizing that Eq. (4.1) is a summation over of the order of a thousand wavelength points, each for about 10 different angles, that this should be done for each of the 100^2 grid points in a horizontal plane and that each of these are the result of solving the differential equation (4.3) at about 100 vertical grid points, it is clear this task

would cause severe digestive problems for even the largest supercomputers of today — and give me a *very* long holiday while waiting for results.

A way around this is to split the problem in two: the detailed frequency-dependent radiation transfer and radiation transfer, in a inhomogeneous medium. The first problem is solved for a 1-D mean stratification when calculating the EOS and opacity tables (Sect. 4.3) and the other one is solved in the simulations (Sect. 4.2).

4.1 The effect of lines

The presence of lines in absorption gives rise to different effects in optically thick and thin regions.

In the optically thick case, the diffusion approximation holds and the lines just enter through their influence on the Rosseland mean opacity, which can be increased significantly (more than 20%, *cf.* Fig. 3.9) by the lines. This increase results in a larger temperature gradient, and as $\tau(T = T_{\rm eff})$ is approximately fixed at $\tau \sim {}^2/_3$, this leads to higher temperatures below the photosphere (for fixed $T_{\rm eff}$). Since the optically thick layers are dominated by convection, this only pertains to a thin layer in cool stars, where the convection zone barely reaches the photosphere (see Sect. 7.2.2). A much more important effect occurs right at the surface, where the optical depth is unity in the continuum. Here, the presence of spectral lines leads to a *blocking* of some of the continuum light, and hence the total flux is reduced, relative to a case with no spectral lines. In order to compensate, so that the total flux indeed equals the nominal flux, the surface temperature must be increased (roughly by ${}^1/_4$ of the fraction of flux that is blocked). This is the so-called *backwarming effect* of spectral lines. Backwarming can also be regarded as the heating by photons back-scattered by the opaque lines.

Let us consider the radiative transfer at a single wavelength, λ, on the corresponding optical depth scale, τ_λ. This single wavelength is not in radiative equilibrium and may contribute heating and cooling

$$Q_{{\rm rad},\lambda} = 4\pi\varrho\kappa_\lambda(J_\lambda - S_\lambda), \tag{4.5}$$

at various heights, as radiative equilibrium only implies that the total heating $Q_{\rm rad}$ is zero. As we move upwards in the atmosphere, to optically thinner heights, the radiation starts to escape from the plasma, which causes an increasing anisotropy in the radiation field. There is no longer radiation coming in from above and less coming in from the sides, so J_λ will be reduced by more than a factor of two in the transition from optical thick to thin. The radiative heating of Eq. (4.5) will therefore become negative, and we have radiative cooling. When the radiation is fully decoupled from the plasma temperature and we only have radiation directed outward, J_λ can no longer decrease. But the source function $S_\lambda \simeq B_\lambda$, which is just a slightly scattering-altered Planck function, will decrease with temperature and

$Q_{\mathrm{rad},\lambda}$ will therefore increase again, eventually giving rise to a heating of the upper parts of the atmosphere.

All the above works in general, as long as non-LTE effects are neglected. Clearly, the higher opacity, the higher up in the atmosphere the various effects will set in. The main effect of spectral lines is to introduce a lot of high opacity in the middle of the source function. The continuous opacity is only large in the UV or in the far IR where the flux is low, but the lines place some high opacity in the most flux-rich wavelength region (*cf.* Fig. 3.6 and 3.7). The lines therefore spread the cooling and heating over a larger range of heights, as compared to an atmosphere without lines. Without lines all of the radiation would just decouple at one height and J would stay almost constant above this height. To obtain radiative equilibrium, $Q_{\mathrm{rad}} = 0$, the temperature would therefore also have to be almost constant above the height of decoupling. The decoupling would of course be spread out a little, as the wavelength variation of the continuum opacity covers a few orders of magnitude in the flux richest part of the spectrum. By including lines, this is easily increased to 6 orders of magnitude (*cf.* Fig. 3.6). The lines ensures that there are both heating and cooling at a large range of heights, and radiative equilibrium can therefore be sustained at a lower temperature. This effect is referred to as *surface cooling* by spectral lines.

4.2 3D radiative transfer

Assuming that the source function is known, as is the case in LTE with a given temperature structure, the equation of transfer (4.3) is a linear first-order differential equation with constant coefficients. This implies that there exists an integrating factor, which can be shown to be equal to $e^{-\tau_\lambda/\mu}$, and we may therefore rewrite the transfer equation as

$$\begin{aligned} I_\lambda(\tau_\lambda,\mu) &= \mu^{-1}\int_{\tau_\lambda}^{\infty} S_\lambda(t)e^{-(t-\tau_\lambda)/\mu}\mathrm{d}t \\ &= \frac{e^{\tau_\lambda/\mu}}{\mu}\int_0^{\infty} S_\lambda(t)e^{-t/\mu}\mathrm{d}t \end{aligned} \tag{4.6}$$

(Mihalas 1978, pp. 38). We recognize the integral as a *Laplace transform* and conclude that $\mu e^{-\tau_\lambda/\mu} I_\lambda(\tau_\lambda,\mu)$ is the Laplace transform, $\mathcal{L}$, of S_λ. We can furthermore define the linear operator $\hat{L}$

$$\hat{L}S_\lambda = \int_0^1 e^{\tau_\lambda/\mu}\mathcal{L}S_\lambda\frac{\mathrm{d}\mu}{\mu} - S_\lambda, \tag{4.7}$$

which is the parenthesis of the integral of the radiative heating in Eq. (4.1).

We also notice that $\hat{L}S_\lambda$ only depends on the run of $S_\lambda(\tau_\lambda)$, so if the relative opacity,

$$x_\lambda = \kappa_\lambda/\kappa, \tag{4.8}$$

where κ is the standard opacity defined in Eq. (4.17) or (4.18), is constant with depth for all wavelengths having relative opacity x_i, then the radiative transfer can be described by the same source function. Now, $x_\lambda(\tau_\lambda)$ is seldom constant, so instead we draw on the linearity of the Laplace operator to approximate the radiative transfer at wavelengths, $x_\lambda = x_i$, with an average source function S_i.

This concept is developed further by regrouping the opacity into four bins, x_i so that each i represents an interval in x, (Nordlund 1982; Nordlund & Dravins 1990) and the radiative heating can then be evaluated using

$$\begin{aligned}
\int_\lambda \kappa_\lambda (J_\lambda - B_\lambda) \mathrm{d}\lambda &\simeq \kappa \sum_j x_{\lambda_j} (J_{\lambda_j} - B_{\lambda_j}) w_{\lambda_j} && (4.9)\\
&= \kappa \sum_i \sum_{j(i)} x_{\lambda_j} (J_{\lambda_j} - B_{\lambda_j}) w_{\lambda_j} && (4.10)\\
&= \kappa \sum_i \sum_{j(i)} x_{\lambda_j} \hat{L}(B_{\lambda_j}) w_{\lambda_j} && (4.11)\\
&\simeq \kappa \sum_i x_i \hat{L} \left(\sum_{j(i)} B_{\lambda_j} w_{\lambda_j} \right) && (4.12)\\
&\equiv \kappa \sum_i x_i \hat{L}(B_i) w_i && (4.13)\\
&\equiv \kappa \sum_i x_i (J_i - B_i) w_i. && (4.14)
\end{aligned}$$

where I use $B_\lambda = S_\lambda$ in the spirit of LTE.

Equation (4.9) is just the discretization of the integral in wavelength, and the right hand side can get as close to the left hand side as we desire, depending on the number of wavelength points we choose. w_λ is the integration weights (not to be confused with the occupation probabilities, w_k, from Sect. 3.2).

The next step, (4.10), is a reordering of the wavelength points into groups, i, where $j(i)$ is the set of wavelength points that fall in bin i (the procedure is specified below), and in (4.11) the $(J_\lambda - B_\lambda)$ is substituted by its corresponding linear operator $\hat{L}(B_\lambda)$. Both of these steps are exact.

Going to (4.12) we employ several crucial assumptions. First of all, the relative opacity is discretized to a small number (in this case four) of values, x_i. The next and less straightforward approximation is to assume that all x_λ belonging to the same bin has the same variation with depth, and therefore can be represented by the same operator $\hat{L}_i$ (Nordlund & Dravins 1990). The next two steps are mere definitions of B_i, w_i and J_i respectively (see Eqs. (4.23) and (4.22) for explicit expressions).

The κ used above, is a standard opacity that defines the optical depth scale, τ, on which to solve the radiative transfer. This κ should be chosen so as to make Eq. (4.12) a good approximation for all optical depths.

In optically thick layers ($\tau_\lambda \gg 1$ for all λ) the diffusion approximation holds, and the *Rosseland mean opacity*

$$\frac{1}{\tilde{\kappa}} = \frac{\int_0^\infty \frac{1}{\kappa_\lambda + \sigma_\lambda} \frac{\partial B_\lambda}{\partial T} d\lambda}{\int_0^\infty \frac{\partial B_\lambda}{\partial T} d\lambda}, \tag{4.15}$$

where the scattering, σ_λ is included, reproduces all the transfer properties of the full monochromatic problem. For $\tau \to 0$, the intensity weighted mean

$$\langle \kappa \rangle J = \int_0^\infty \kappa_\lambda J_\lambda d\lambda \tag{4.16}$$

without scattering, reproduces the fluxes of the monochromatic solution (Mihalas 1978, Chapter 3.2). The original choice for the standard opacity was therefore

$$\kappa = e^{-2\tau} \langle \kappa \rangle + (1 - e^{-2\tau}) \tilde{\kappa}, \tag{4.17}$$

which is just a smooth transition between the two limiting cases (Nordlund & Dravins 1990). During my work, this was refined by Åke Nordlund and replaced by

$$\kappa = e^{-30\tilde{\tau}^*} \langle \kappa \rangle^* + (1 - e^{-30\tilde{\tau}^*}) \tilde{\kappa}^*, \tag{4.18}$$

where $\tilde{\tau}^*$ corresponds to the Rosseland mean opacity for the continuum bin ($i = 0$). The purpose of decreasing the optical depth at which the transition takes place is to ensure that the relatively large intensity weighted mean does not "contaminate" the opacity at optical depth unity.

The Rosseland mean opacity now only includes the continuum bin ($i = 0$),

$$\frac{1}{\tilde{\kappa}^*} = \frac{\sum_{j(i=0)} \frac{1}{\kappa_{\lambda_j} + \sigma_{\lambda_j}} \frac{\partial B_{\lambda_j}}{\partial T} w_{\lambda_j}}{\sum_{j(i=0)} \frac{\partial B_{\lambda_j}}{\partial T} w_{\lambda_j}}. \tag{4.19}$$

The intensity weighted opacity has been altered to only include optically thin wavelengths, by weighting with a factor $e^{-\tau_{\lambda_j}/2}$

$$\langle \kappa \rangle^* = \frac{\sum_j \kappa_{\lambda_j} J_{\lambda_j} e^{-\tau_{\lambda_j}/2} w_{\lambda_j}}{\sum_j J_{\lambda_j} e^{-\tau_{\lambda_j}/2} w_{\lambda_j}}. \tag{4.20}$$

The opacity table is calculated from a continuum Rosseland mean opacity, $\tilde{\kappa}_{\rm c}$, based on the continuum opacity alone, and then from the standard opacity we derive a correction factor, $x_\kappa = \kappa/\tilde{\kappa}_{\rm c}$. But κ is only evaluated for a single ϱ/T-track for

a given simulation and not for the whole table. x_κ is then regarded as a function of either temperature or optical depth, and is interpolated in the rest of the table to obtain κ. Nordlund & Stein use $x_\kappa(T)$, whereas I use $x_\kappa(\tau)$ after having found that τ for a given simulation may be approximated by a function in ϱ and T — in particular for small τ.

The standard opacity, so defined, reproduces the emergent flux of the full monochromatic problem well within one percent. This is checked routinely for all the simulations, by evaluating the radiative transfer for a slice of the simulation box, using the methods described in Sect. 4.3, both for the full monochromatic opacity and for the binned opacity. The differences are random and are due to the varying thermodynamical structure in the simulations, as x_κ is only evaluated for one ϱ/T stratification. The temporal and surface averaged fluxes are very close to the monochromatic case.

The opacity binning works as follows: The bins of relative opacities are chosen to be logarithmically equidistant

$$x_i = 10^{ai}, \tag{4.21}$$

where we use $i = 0, 1, 2, 3$ and $a = 1$. The binning weights are (following from the step (4.12) to (4.13))

$$w_i = \sum_{j(i)} w_{\lambda_j} \tag{4.22}$$

and it also follows that

$$B_i = \left(\sum_{j(i)} B_{\lambda_j} w_{\lambda_j} \right) / w_i. \tag{4.23}$$

The $j(i)$ over which the sums are taken are those j where τ_{λ_j}reaches unity within $i - \frac{1}{2} < \log \tau < i + \frac{1}{2}$, where τ without subscript is the standard optical depth scale defined via the standard opacity.

$$\mathrm{d}\tau = \varrho \kappa \mathrm{d}z. \tag{4.24}$$

The opacity binning is calculated for a horizontally averaged snapshot of the simulation. The pseudo Planck functions, B_i, are functions of temperature only through the temperature dependence of the Planck function, so the bin-membership of a contributing wavelength is assumed independent of temperature.

The angular integration to obtain the mean intensity, Eq. (4.16), is evaluated by keeping the simulation box fixed and interpolating it to a tilted grid, exploiting the periodic horizontal boundaries. Only the rectangular part of the box having standard optical depth $\tau < 300$ is used for the radiative transfer calculations, and this part is furthermore rescaled as described in Sect. 2.5 to optimize the resolution with respect to this problem.

As the simulations are far from plane parallel (the reason to perform the simulations), we have two independent angles to integrate over: inclination with vertical

(radial) lines, θ, and rotation about this line, ϕ. The radiative transfer is evaluated with just two θ-points and four ϕ-points, where the ϕ-points are rotated 15° per timestep to prevent the development of directional preferences. The $\mu = \cos\theta$-points are $\mu = 1, {}^1/_3$ with integration weights ${}^1/_4$ and ${}^3/_4$ respectively. The integral over ϕ is evaluated with the trapezoidal method. Including $\mu = 1$ is advantageous, because no ϕ averaging is need for vertical rays, and because the vertical direction in general gives the highest contribution to the flux. Given the two μ values, the weights are chosen to give exact results for the highest polynomial $I(\mu)$ (in this case a 1st order polynomial as we have two μ-points).

4.3 1D radiative transfer

In order to determine the bin membership of the wavelength points, *i.e.* the binned pseudo Planck functions, B_i, and the opacity correction factor x_κ, the detailed radiative transfer, Eq. (4.3), is calculated directly for all the wavelength points in the ODF representation of the opacity, for a horizontal and temporal averaged ϱ/T-stratification of the model.

The 3D effects, from integrating over tilted rays through an inhomogeneous media, are of course neglected, but instead the full wavelength dependence is included. While the models are in the process of relaxing, the mean stratification is checked from time to time, to assure that the table is consistent with the simulation. Also the binned emerging flux is compared with the detailed to make sure that the binning does not alter the surface averaged emerging flux.

4.4 The Feautrier technique

For both the 1D and 3D case, the transfer equation is solved using a modified *Feautrier technique* (Mihalas 1978; Nordlund 1982). The radiative transfer equation (4.3) is normally rewritten in terms of the average of in- and out-going intensities along a ray into the space angle Ω,

$$p_\lambda = \tfrac{1}{2}[I_\lambda(\Omega) + I_\lambda(-\Omega)] \tag{4.25}$$

$$\frac{\mathrm{d}^2 p_\lambda}{\mathrm{d}\tau_\lambda^2} = p_\lambda - B_\lambda, \tag{4.26}$$

with boundary conditions

$$\frac{\partial p_{\lambda,\Omega}}{\partial \tau_\lambda} = \begin{cases} p_{\lambda,\Omega} & \text{for } \tau_\lambda = 0 \\ \dfrac{\partial B_\lambda}{\partial \tau_\lambda} & \text{for } \tau_\lambda = \tau_{\lambda,\mathrm{max}} \end{cases}, \tag{4.27}$$

which is then solved numerically using some finite-difference scheme (Mihalas 1978). However, as p_λ approaches B_λ at large optical depths, the problem get very ill-posed

and leads to fatal round-off errors. If instead we use

$$q_\lambda = p_\lambda - B_\lambda, \tag{4.28}$$

and therefore

$$\frac{\mathrm{d}^2 q_\lambda}{\mathrm{d}\tau_\lambda^2} = q_\lambda - \frac{\mathrm{d}^2 B_\lambda}{\mathrm{d}\tau_\lambda^2}, \tag{4.29}$$

which can be solved in the same way as (4.26), but with the boundary conditions

$$\frac{\mathrm{d}q_\lambda}{\mathrm{d}\tau_\lambda} = q_\lambda + B_\lambda - \frac{\mathrm{d}B_\lambda}{\mathrm{d}\tau_\lambda} \qquad \text{for} \quad \tau_\lambda = 0 \tag{4.30}$$

$$q_\lambda = 0 \qquad \text{for} \quad \tau_\lambda = \tau_{\lambda,\mathbf{max}} \tag{4.31}$$

we can obtain accurate solutions for all τ.

Chapter 5

Six different stars

I have chosen a set of six pairs of stellar atmosphere parameters, $T_{\rm eff}$ and $g_{\rm surf}$, for my convection simulations, as listed in Tab. 5.1. This choice is motivated by the possibility of observing solar-like oscillations of the stars associated with these parameters. The first 6 rows in Tab. 5.1 contain the adopted observed global quantities for each of the stars. Star B is just a set of parameters, with no actual star attached to it, and started as a simulation of Procyon that turned out to give too low a $T_{\rm eff}$. The chemical mixture is $X = 70.296\%$ and $Z = 1.788\%$ corresponding to Gustafsson's mixture (*cf.* Sect. 3.1). Below the thin line, which splits the table in two, I

Table 5.1: Parameters for the simulations.

name	α Cen B	Sun	α Cen A	Star B	η Boo	Procyon
Spectral class	K 1 V	G 2 V	G 2 V	——	G 0 IV	F 5 IV-V
$T_{\rm eff,*}$	5325 K	5777 K	5800 K	6184 K	6070 K	6500 K
$g_{\rm surf}/[{\rm cm\,s^{-2}}]$	$3.604{\cdot}10^4$	$2.740{\cdot}10^4$	$1.970{\cdot}10^4$	$1.084{\cdot}10^4$	$5.668{\cdot}10^3$	$1.084{\cdot}10^4$
$M/M_\odot$	0.900	1.000	1.085	1.240	1.630	1.750
$L/L_\odot$	0.494	1.000	1.532	4.070	9.600	7.080
$R/R_\odot$	0.827	1.000	1.228	1.770	2.807	2.102
$T_{\rm eff}$	5362 K	5801 K	5768 K	6167 K	6023 K	6470 K
α	1.904	1.889	1.844	1.763	1.788	1.772
$d_{\rm CZ}$	30.69%	28.64%	30.71%	19.72%	21.50%	10.65%
$\left(\frac{P_{\rm turb}}{P_{\rm tot}}\right)_{\rm max}$	7.9%	10.7%	11.2%	15.5%	19.5%	21.0%

have given a few results from the simulations. These will be explained and discussed later in this chapter, and right now they just serve as appetizers. The stars in the table are ordered, from left to right, in increasing vehemence of the convection of which the peak turbulent- to total pressure ratio (given in the last row) is a rather

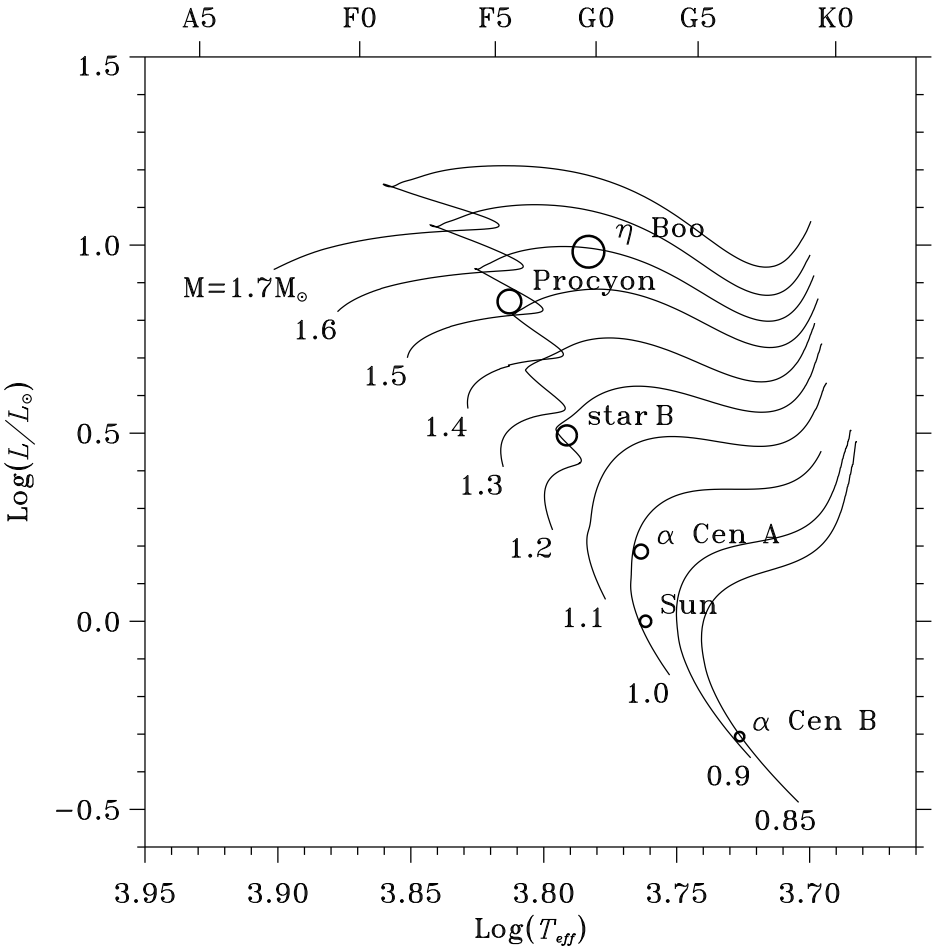

Fig. 5.1: This HR-diagram shows the six stars I investigate in this work, together with evolutionary tracks of stars in the same mass range. The evolutionary tracks, courtesy Christensen-Dalsgaard, give an idea of the evolutionary state of each of the six stars. The size of the symbols reflects the radii of the stars. The mass of the virtual star, Star B, is about 1.27 $M_\odot$, when derived from the tracks shown here.

good measure. I will return to this fierceness of the convection and other measures of it as well as its significance, repeatedly in this chapter.

The surface gravity, $g_{\rm surf}$, is an input parameter for the simulation, whereas the effective temperature depends on the convective fluxes in the model, and can be adjusted by changing the entropy of the gas flowing into the box at the bottom boundary, as described in Sect. 2.3.3.

The main objective of this work is to make a differential comparison of convection for various atmosphere parameters, rather than to compare specific stars. This is the reason that I just use the same chemical mixture for all the stars, and that I have not fine tuned the effective temperatures. These simulations will then be used as initial conditions for precise simulations of the actual stars, with the observed abundances and probably also with a higher resolution, in future work. This I have

so far only done in the solar case, as presented in chapter 8. In Fig. 5.1 I present the six program stars in an evolutionary context. The evolutionary tracks plotted in this figure (Christensen-dalsgaard 1982), are based on an EOS somewhat simpler than the MHD EOS used in the rest of this work, and is dubbed the EFF EOS for the initials of its authors, Eggleton et al. (1973). The evolutionary tracks are shifted systematically towards lower effective temperature and luminosity as compared to the MHD EOS case. The tracks based on MHD go straight through the location of the Sun and α Cen B, but due to the boundaries of the MHD EOS tables these tracks could not be followed to greater masses. The physics in the evolution code is treated in exactly the same way as in the envelope code and as described in Sect. 6.2.1. For the $T-\tau$ relation in the atmospheres of these models, a scaled fit to the $T-\tau$ relation derived from the solar simulation was used. Also the α derived from envelope matching to the solar simulation (see Tab. 5) was used for all the models. Assuming the (scaled) $T-\tau$ relation and α to be invariant is in accordance with normal practice. The validity of this practice is discussed and questioned in Trampedach et al. (1998a) and Trampedach et al. (1998b) (see App. D and E, respectively).

5.1 The asteroseismic motivation

The advent of helioseismology has opened up a whole new window to the solar interior, and now asteroseismology brings the promise of windows to the interior of other stars too. This will certainly be a vast improvement of the observational side of astrophysics, since until now we have only had the solar reference point for our stellar models. The micro physics, *i.e.* the EOS and the opacity, is of course independent of this state of affairs, as these are evaluated from *ab initio* models, but the convection that until now has been treated using the very crude mixing-length theory (MLT) for the majority of stellar models has one or two free parameters which are not set by the theory. It has been costumary to calibrate the MLT parameter α, and the likewise undetermined He abundance, Y, to obtain a solar model of the present age, radius and luminosity and then use this value, $\alpha_\odot$, for models of other stars too.

The detection of a large selection of p-modes in other stars, would suddenly give us a much firmer handle on our stellar models. In particular, dynamical phenomena are just extrapolated from the solar case, where the rather subtle effects on the thermodynamic stratification can be validated against the wealth of observed p-modes. Among these dynamical phenomena we find, apart from the obvious convection, also overshooting from convection zones into the surrounding stable layers (*cf.* Sect. 7.3), rotation and in particular differential rotation, semi convection, rotationally induced mixing and tidal distortion in binary and multiple systems. Still without touching the complications arising when introducing magnetic fields.

Based on the work of Christensen-Dalsgaard & Frandsen (1983), Kjeldsen &

Bedding (1995) have estimated the amplitudes of solar like oscillations in other stars, extrapolating from the solar case. Their work suggests that α Cen A and Procyon, among others, might oscillate with (soon) observable amplitudes. Also Christensen-Dalsgaard & Frandsen (1983) and Houdek et al. (1994) argue that more evolved stars, *i.e.* subgiants, will oscillate with larger amplitudes than main-sequence stars.

5.1.1 The Sun

The Sun has been a natural starting point for our exploration of stars, ever since it was realized that our Sun was just another star, which is one of the reasons that this star has been included in my work. Another reason is of course its proximity, which has allowed a quality and diversity of observations not possible for any other star. All these observations put tight constraints on theoretical models and are invaluable in validating (or discarding) the convection simulations presented here. The Sun is the only star for which the surface granulation (Sect. 7.2) can be seen directly and followed in time. Also the global intensity variation over the solar disk can be measured, and the very high dispersion spectra obtainable from the Sun allow very precise determinations of spectral line profiles (*cf.* Sect. 7.2.1). These spectra can tell a lot about the atmospheric stratification, chemical mixture and the velocity field — but only through analysis and comparison with theoretical spectra based on solar atmosphere calculations. Though the modern analysis and models are very sophisticated, there is still room for some controversies. The solar iron abundance, for example, which is a rather fundamental quantity is still uncertain and observations seem self-contradictory (*cf.* Sect. 9.3).

The solar effective temperature, 5777 ± 2.5 K, is derived from the solar irradiance observations giving, $L_\odot = (3.846 \pm 0.006) \cdot 10^{33}\,\mathrm{erg\,s^{-1}}$ (Willson & Hudson 1988), and using the solar radius (at optical depth $\tau = 1$), $R_\odot = 6.96 \cdot 10^{10}$ cm and the astronomical unit, 1 A. U.=$1.49598 \cdot 10^{13}$ cm (Stix 1989).

For the solar mass, I used the commonly used value, $M_\odot = 1.989 \cdot 10^{33}$ g, in agreement with solar system dynamics (Stix 1989) $GM_\odot = 1.32712438 \cdot 10^{26}\,\mathrm{dyn\,cm^2\,g^{-1}}$ and the CODATA value of the gravitational constant, $G = (6.67259 \pm 0.00085) \cdot 10^{-8}\,\mathrm{dyn\,cm^2\,g^{-2}}$ (Cohen & Taylor 1987), but gives $G = 6.67232 \cdot 10^{-8}\,\mathrm{dyn\,cm^2\,g^{-2}}$. These values are exactly the same as used by Christensen-Dalsgaard & Däppen (1992) for the 1D-models I compare with in Sect. 6.2.

5.1.2 The α Cen system

α Cen A and B (HD 128620 and HD 128621) are the two brightest members of a triple star system, where the C component, not studied here, is a small M5 V dwarf about ten magnitudes fainter than α Cen A and B. α Cen C is the well-known Proxima Cen — the closest star to the solar system, a mere 1.3 parsecs away. The A and B components form a fairly tight binary system, with mean separation of around 24 AU, and a period of 100 years, whereas the C component is very loosely

bound, if bound at all (Anosova et al. 1994).

As fundamental parameters for the two stars I have chosen luminosities in accordance with Noels et al. (1991), who find $\log(L_{\alpha\,\mathrm{CenA}}/L_\odot) = 0.1853 \pm 0.015$ and $\log(L_{\alpha\,\mathrm{CenB}}/L_\odot) = -0.3065 \pm 0.015$. The effective temperatures are chosen to agree with those obtained by Chmielewski et al. (1992), based on differential atmosphere analysis of hydrogen H_α line wings, between atmospheres in the model grid of Gustafsson et al. (1975). Using this method they find $T_{\mathrm{eff},\alpha\,\mathrm{CenA}} = 5800 \pm 20\,\mathrm{K}$ and $T_{\mathrm{eff},\alpha\,\mathrm{CenB}} = 5325 \pm 50\,\mathrm{K}$. Their analysis also results in a metallicity of [Fe/H]$= 0.22 \pm 0.02$ and [Fe/H]$= 0.26 \pm 0.04$ for α Cen A and α Cen B respectively. The masses determined from astrometrical data are $M_{\alpha\,\mathrm{CenA}}/M_\odot = 1.085 \pm 0.01$ and $M_{\alpha\,\mathrm{CenB}}/M_\odot = 0.90 \pm 0.01$ (Demarque et al. 1986).

Due to the many tight observational constraints on this binary, its assumed coevolution and chemical homogeneity, it is a very good challenge to stellar modelling. This challenge has been taken up by several teams with varying success. Conventional stellar models using the MLT formulation of convection and its parameter α, set by calibrations to the Sun, leads to too small a radius for α Cen A (Demarque et al. 1986). Fernandes & Neuforge (1995) who questions the universality of the MLT, finds that α is likely to differ with 0.2-0.3 between the two, with α_B being closest to the solar value. Lydon et al. (1993a) abandons the MLT picture altogether, and use various correlation functions derived from numerical simulations to describe the convection zone (See Sect. 7.5 for a discussion of their method).

5.1.3 η Boo

η Boo (HD 121370) is the most luminous G-type subgiant in the sky, which is rather promising for detections of solar-like oscillations, as mentioned in Sect. 5.1. This is in fact also the star with the most convincing detection of solar-like oscillations to date (Kjeldsen et al. 1995). By observing the temperature oscillations, through the effect on the hydrogen Balmer lines, they were able to detect and identify 13 modes.

Christensen-Dalsgaard et al. (1995) subsequently constructed evolutionary sequences of stars in the expected mass range, and calculated oscillation frequencies for these. The model that fits the observational constraints on both frequencies, effective temperature and luminosity, has $M_{\eta\mathrm{Boo}}/M_\odot = 1.63$, $T_{\mathrm{eff},\eta\mathrm{Boo}} = 6070\,\mathrm{K}$ and $L_{\eta\mathrm{Boo}}/L_\odot = 9.6$ (see also Tab. 5.1), in accordance with observations: $T_{\mathrm{eff},\eta\mathrm{Boo}} = 6070 \pm 50\,\mathrm{K}$ (Bell & Gustafsson 1989), and combining this with a parallax of 85.8 ± 2.3 mas (milliarcsecond) (Harrington et al. 1993) and an angular diameter of 2.24 ± 0.02 mas (Blackwell & Lynas-Gray 1994), gives a luminosity, $L_{\eta\mathrm{Boo}}/L_\odot = 9.5 \pm 0.7$.

The evolution calculations indicate that η Boo is in the hydrogen shell burning phase, although this is slightly dependent on the adopted value of the mixing-length parameter, α. A hydrogen shell source can have rather profound implications for the observed frequencies, as the expected sharp edge of the helium core can alter the behaviour of the p-modes to make them appear similar to trapped internal gravity waves (g-modes, not to be confused with the gravitational waves of general

relativity). The observed frequencies do in fact show signs of this effect, as discussed by Christensen-Dalsgaard et al. (1995).

5.1.4 Procyon

Procyon (α CMi, HD 61421) is the most luminous member of a binary system, only about 3.5 parsecs from the solar system. The B component is a $0.62\,M_\odot$ white dwarf, about ten magnitudes fainter than Procyon A (Provencal et al. 1997). They encircle each other with a period of 40.4 years, a close 16 AU apart.

The mass of Procyon is chosen in accordance with the astrometric observations, $M_{\rm Procyon}/M_\odot = 1.751 \pm 0.051$ (Irwin et al. 1992). The effective temperature $6500 \pm 100\,$K and luminosity $[\log L_{\rm Procyon}/L_\odot] = 0.85 \pm 0.06$ have been derived using a variety of observations, including angular diameter and absolute integrated flux measurements (Steffen 1985).

Due to its brightness and proximity, Procyon has also found widespread use as a flux standard, and motivated the "Photometric atlas of the spectrum of Procyon" (Griffin & Griffin 1979). But despite the many and diverse observations, repeated efforts to model this star has failed. One of the more recent attempts to model Procyon (Guenther & Demarque 1993) brings it barely inside the observational error bars. It is my belief that proper 3D RHD atmosphere models of this star will contribute significantly to resolving this problem. The convection in the atmosphere of Procyons is far more vigorous than in the solar atmosphere, and it should therefore not be a surprise that 1D atmospheres cannot reproduce observations.

The effect of convection is twofold. First it alters the emerging fluxes, mainly because of the large temperature fluctuations that affect the ionization equilibria and therefore the occupation of the absorbing states. The spectra are thus not thermodynamically consistent with a 1D model — the horizontally averaged occupation number of a state does not follow from the horizontally averaged temperature (see Sect. 6.1). This is a very likely cause for the confusion on abundances, and makes it hard to deduce a $T_{\rm eff}$ from spectroscopy.

Second, the very substantial turbulent pressure, amounting to more than 20% of the total pressure in the photosphere (see Tab. 5.1), greatly affects the hydrostatic equilibrium and expands the atmosphere. This furthermore changes the temperature gradient, $\nabla = {\rm dln}T/{\rm dln}P$, which alters the effect of the mixing-length parameter α. My estimate of the depth of the convection zone, $d_{\rm CZ}$, is 30% larger than that of the model of Guenther & Demarque (1993) having the deepest convection zone and involves twice as much mass. This can of course have some implications over the lifetime of the star, especially considering the late evolutionary stage of Procyon.

The next interesting step to take is of course to derive more precise fundamental parameters for Procyon, based on the new HIPPARCOS parallaxes (Emanuele et al. 1996; Lindegren et al. 1997). There have been several attempts to observe p-modes in Procyon (Isaak & Jones 1988; Gelly et al. 1988; Brown et al. 1991), but no definite positive detection to date.

Chapter 6

Mean models

For the sake of analysis and comparison with 1D models, I have computed various averages of a large number of quantities of the simulations. The averaging procedures are explained in App. D and E, and results in horizontally as well as optical depth averaged quantities, as listed in App. C.

6.1 The effect of non-linear fluctuations

In 3D models, a rather serious and yet unappreciated complication is introduced through the fluctuations of thermodynamic quantities: As the EOS (*cf.* Sect. 3.2) in general is not linear, in particular not in the photosphere where ionization of hydrogen sets in, we have that $\langle \mathrm{EOS} \rangle \neq \mathrm{EOS}(\langle \varrho \rangle, \langle \varepsilon \rangle)$, where "EOS" just denotes any thermodynamic quantity. How serious the '$\neq$'-sign is, is illustrated with EOS=T in Fig. 6.1. The effect on the horizontal average is rather dramatic (black solid versus gray solid lines), but even when the averaging is separated in the upflows (dashed) and the downflows (dotted), the pronounced discrepancy persists.

This means that the mean density/mean energy stratification is unlikely to result in a pressure corresponding to hydrostatic equilibrium. It is likewise unlikely that the averaged thermodynamical quantities are thermodynamically consistent, *i.e.* related through the expressions in Sect. 3.5. The opacity (see Sect. 3.3), being even more nonlinear, will naturally result in a larger discrepancy, severely complicating our analysis of the transition region in the photosphere.

6.2 Matching with 1-D envelopes

The simulations only cover a very thin layer near the surface of the stars, but I would like infer properties of the bulk of the CZ from the simulations. In order to do so, I have developed a program for matching 1D envelope models (Christensen-Dalsgaard & Däppen 1992; Christensen-Dalsgaard 1993) with the averaged simulations. Convection in the envelope models is described by the standard MLT formalism (*cf.*

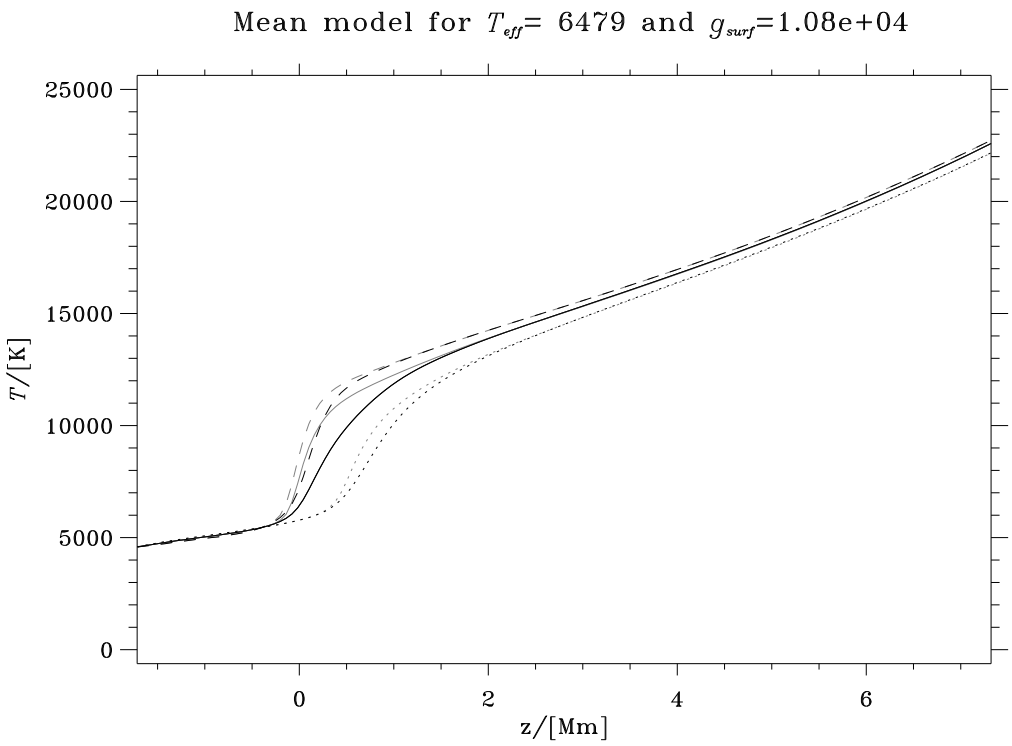

Fig. 6.1: This figure shows the effect of a non-linear EOS, on the temporal and horizontal averaged temperatures of the Procyon simulation. The black lines are averages of the actual temperature, and the gray lines are the temperature evaluated via the EOS, as $T(\langle\varrho\rangle, \langle\varepsilon\rangle)$. Dotted lines are for the downflow, dashed for the upflow, and solid lines are for the total horizontal average.

Sect. 6.2.1). To make the 1D and 3D models as compatible as possible, I have introduced a turbulent pressure in the 1D models

$$P_{\text{turb,1D}} = \beta v_{\text{conv}}^2 \varrho, \tag{6.1}$$

where v_{conv} is the MLT convective velocity, given by Eq. (6.8). β is a form factor, which I assume constant with depth (but differs between stars). The purpose of this $P_{\text{turb,1D}}$ is to supply the envelope model with a turbulent pressure below the fitting point, which resembles the turbulent pressure that would result from an extension of the simulation to large depths. From Figs. 6.2-6.7 we see that Eq. (6.1) is a reasonable extrapolation of the turbulent pressure of the simulations.

The matching is performed as follows:

- The coefficients of the expression

$$T = T_{\text{eff}} \left(\frac{3}{4}\right)^{\frac{1}{4}} \left[c_1 + \tilde{\tau} + c_2 e^{-c_3\tilde{\tau}} + c_4 e^{-c_5\tilde{\tau}}\right], \tag{6.2}$$

are fitted to the temporal and $\tau_{\rm Ross}$-averaged temperature, above $\tau_{\rm Ross} = 2.2$ (the fit does not work below this, and all energy is transported by convection here, anyway). This fit is then used for a T-τ relation in the envelope calculations (see also App. E).

- A fitting (total) pressure, $P_{\rm fit}$, is chosen deep in the simulation to minimize the effects of non-linear fluctuations (see Sect. 6.1), but also far enough from the bottom to avoid boundary effects (as can be seen in $\nabla_{\rm s}$, Fig. 3.2).

- I then solve

$$T_{\rm 3D}(P_{\rm fit}) = T_{\rm 1D}(P_{\rm fit}) \quad and \qquad \varrho_{\rm 3D}(P_{\rm fit}) = \varrho_{\rm 1D}(P_{\rm fit}) \tag{6.3}$$

using a Newton-Raphson scheme in α, the mixing-length parameter, and β, from Eq. (6.1) (see also App. D).

The mass and luminosity of the envelope is constant during the fitting procedure, and corresponds to $g_{\rm surf}$ and $T_{\rm eff}$ of the simulation, whereas $g_{\rm surf}$ and $T_{\rm eff}$ for the envelope differs from those of the simulation due to the elevation effect. This amounts to no more than a few Kelvins, though.

6.2.1 The MLT formulation

The normal way to incorporate the effects of convection in stellar model, whether it is atmosphere, envelope or evolutionary models, is by use of the mixing-length theory (MLT). The philosophy behind this theory is described in Sect. 7.4. There are a lot of variations over the MLT theme, and many researchers have tried to make it less ad hoc by taking account of various effects not considered in the original formulation. An excellent overview of these variatiants can be found in Gough (1976).

The envelope program I use (Christensen-Dalsgaard & Däppen 1992) relies on the MLT version by Böhm-Vitense (1958) which was first incorporated in stellar evolution calculations by Henyey et al. (1965).

The radiative flux is expressed as

$$F_{\rm rad} = \frac{4acT^4\nabla}{3\tilde{\kappa}H_P}, \tag{6.4}$$

where ∇ is the horizontal average stratification and the total flux is

$$F = \frac{4acT^4\nabla_{\rm rad}}{3\tilde{\kappa}H_P}, \tag{6.5}$$

where $\nabla_{\rm rad}$ is the temperature gradient necessary for transporting the whole flux by radiation. The convective flux is assumed equal to the enthalpy flux, F_H, thereby neglecting a possible kinetic energy flux, $F_{\rm kin}$,

$$F_{\rm conv} \simeq F_H = \tfrac{1}{2}c_P\varrho^2 v\alpha T(\nabla - \nabla'), \tag{6.6}$$

where ∇' is the temperature gradient of the convective eddies and

$$\nabla_{\rm ad} < \nabla' < \nabla < \nabla_{\rm rad} \tag{6.7}$$

in a convection zone. The neglect of $F_{\rm kin}$, Eq. (7.2) is based on the assumption of a filling factor $f_{\rm up} = \frac{1}{2}$, where $f_{\rm up}$ is the fraction of a horizontal cross section occupied by upflows. Also neglecting density fluctuations and demanding a zero net mass flux results in $F_{\rm kin} = 0$.

The mean speed corresponding to the convective flux is

$$v^2 = gH_P\delta\frac{\alpha^2}{\nu}(\nabla - \nabla'), \tag{6.8}$$

where ν is a factor that describes the braking by turbulence. With $\nu = 4$ there is no breaking and ν increases with increasing turbulent viscosity. Böhm-Vitense (1958) somewhat arbitrarily suggested $\nu = 8$ which is also adopted in this work. δ is the logarithmic density gradient at constant pressure; $\delta = -(\partial \ln\varrho/\partial \ln T)_P$. The convective efficiency factor is defined by

$$\gamma = \frac{\nabla - \nabla'}{\nabla' - \nabla_{\rm ad}}, \tag{6.9}$$

and is determined by the horizontal radiative flux between a rising bubble and its surroundings

$$\gamma = \frac{c_P\varrho^2}{2acT^3\theta}, \tag{6.10}$$

where θ is an interpolation between the optical thick and optical thin cases

$$\theta = \frac{\alpha H_P\kappa}{1 + y(\alpha H_P\kappa)^2}. \tag{6.11}$$

The parameter y is determined by the horizontal temperature profiles of a rising blob in the opaque case. Christensen-Dalsgaard (1993) uses $y = 1/3$ in accordance with the original suggestion by Böhm-Vitense (1958). The total flux is just taken to be the sum of the radiative and convective fluxes

$$F = F_{\rm rad} + F_{\rm conv}. \tag{6.12}$$

Combining Eqs. (6.4)-(6.12) and eliminating F, v and ∇' yields a cubic equation in the convective efficiency

$$\phi\gamma^3 + \gamma^2 + \gamma = B(\nabla_{\rm rad} - \nabla_{\rm ad}) \tag{6.13}$$

where $\phi = 3/4y$.

The effect of varying the two parameters ν and y was assessed by Henyey et al. (1965), but they are barely mentioned nowadays and the MLT is commonly considered a one-parameter theory.

6.2.2 The Sun

Fig. 6.2 presents the results of matching the solar simulation with a 1D envelope model. The match is successful, and the two cases seem to approach each other asymptotically at depth (which is assumed with this matching scheme). At a depth of 1.5 Mm the two cases begin to diverge, and in the photosphere, the elevation by turbulent pressure, Λ, as described by Eq. (7.10), is easily recognized. It is

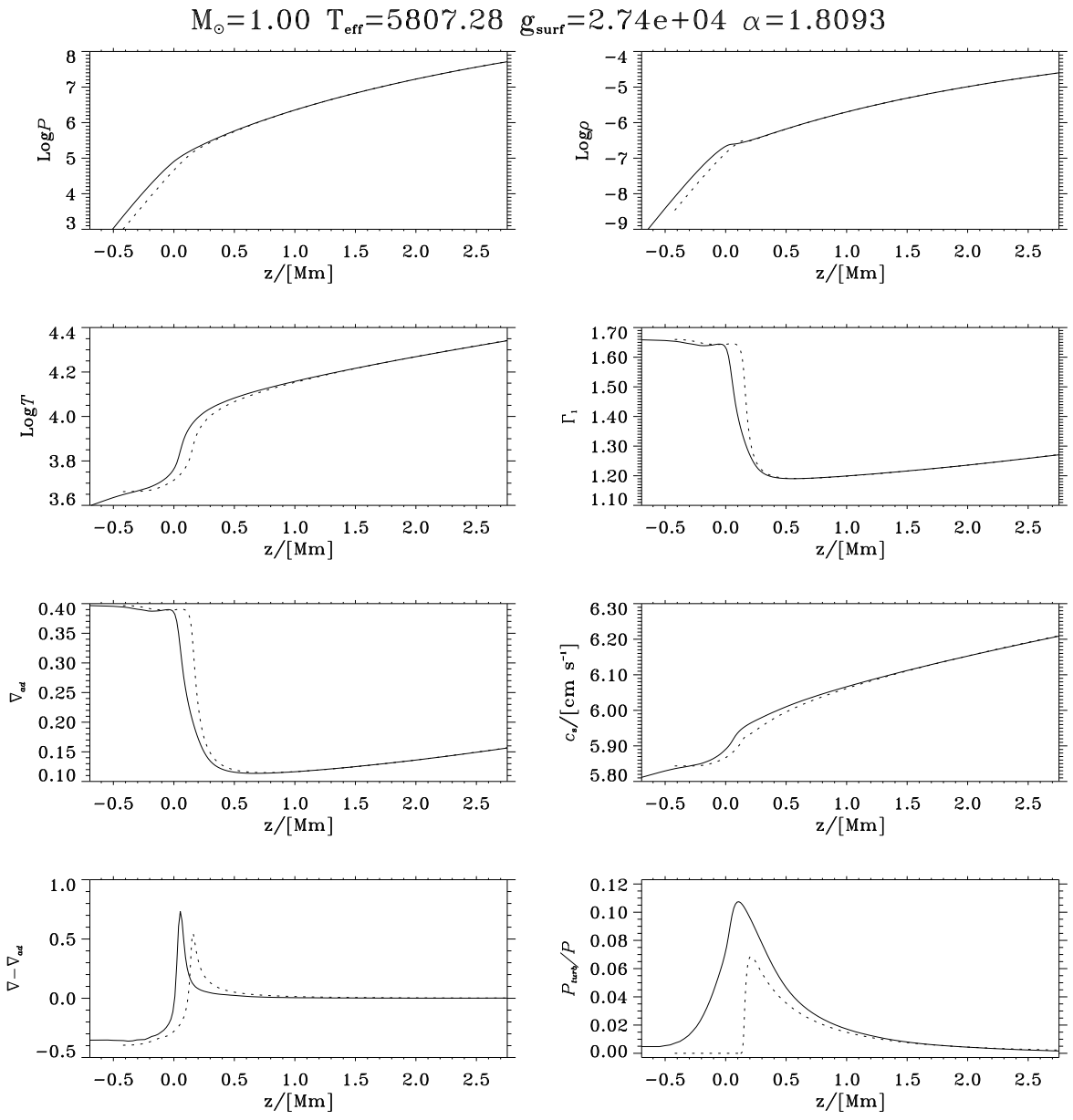

Fig. 6.2: Comparison of the horizontally averaged simulation (solid lines) and the matched 1D envelope model (dotted lines) for the solar case.

reassuring to see, how well the actual 3D turbulent pressure is approximated by the MLT expression, Eq. (6.1).

6.2.3 α Cen A

The result of matching envelope models to the α Cen A simulation, Fig. 6.3, are rather similar to the solar case, Fig. 6.2. Notice how the large drop in *e.g.* Γ_1 and $\nabla_{\rm ad}$ just below the photosphere, due to ionization of hydrogen, is broadened relative to the 1D case, because of the turbulent pressure expansion of the atmosphere. As is also the case for the solar match, although less pronounced, this broadening is accompanied by an narrowing and slight increase, of the superadiabatic peak.

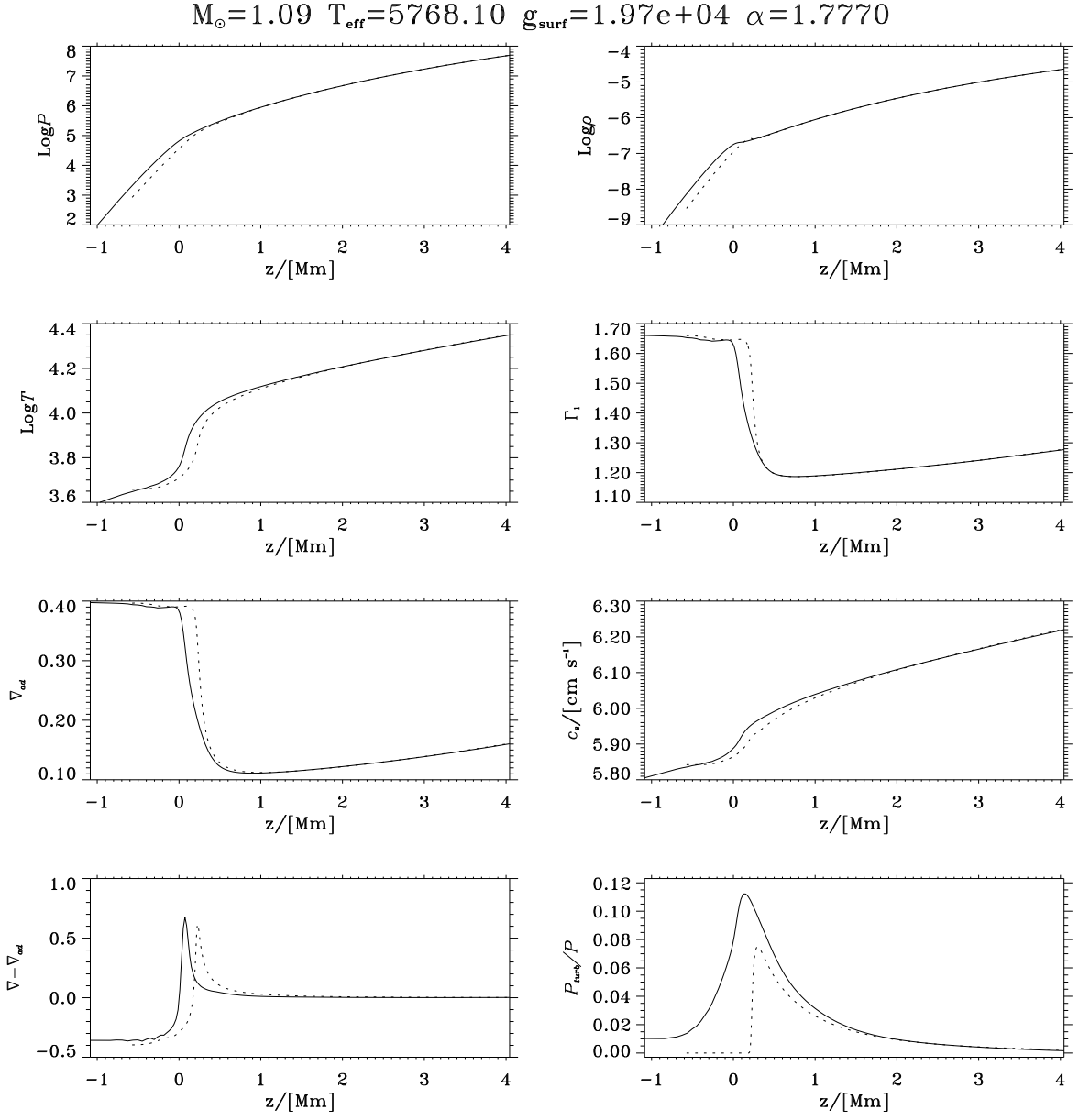

Fig. 6.3: Comparison of the horizontally averaged simulation (solid lines) and the matched 1D envelope model (dotted lines) for α Cen A.

6.2.4 α Cen B

α Cen B is the star with the most sedate convection and, as expected, turns out to be the star best described by a 1D envelope model. Most of the turbulent pressure can even be described by MLT, except for the overshoot region of course. This lack of overshoot means that less than half of the actual turbulent pressure levitation, Λ, is present in the 1D model (*cf.* Fig. 7.10). The envelope model of course also lacks the inhomogeneities, which accounts for about 30% of the atmospheric expansion.

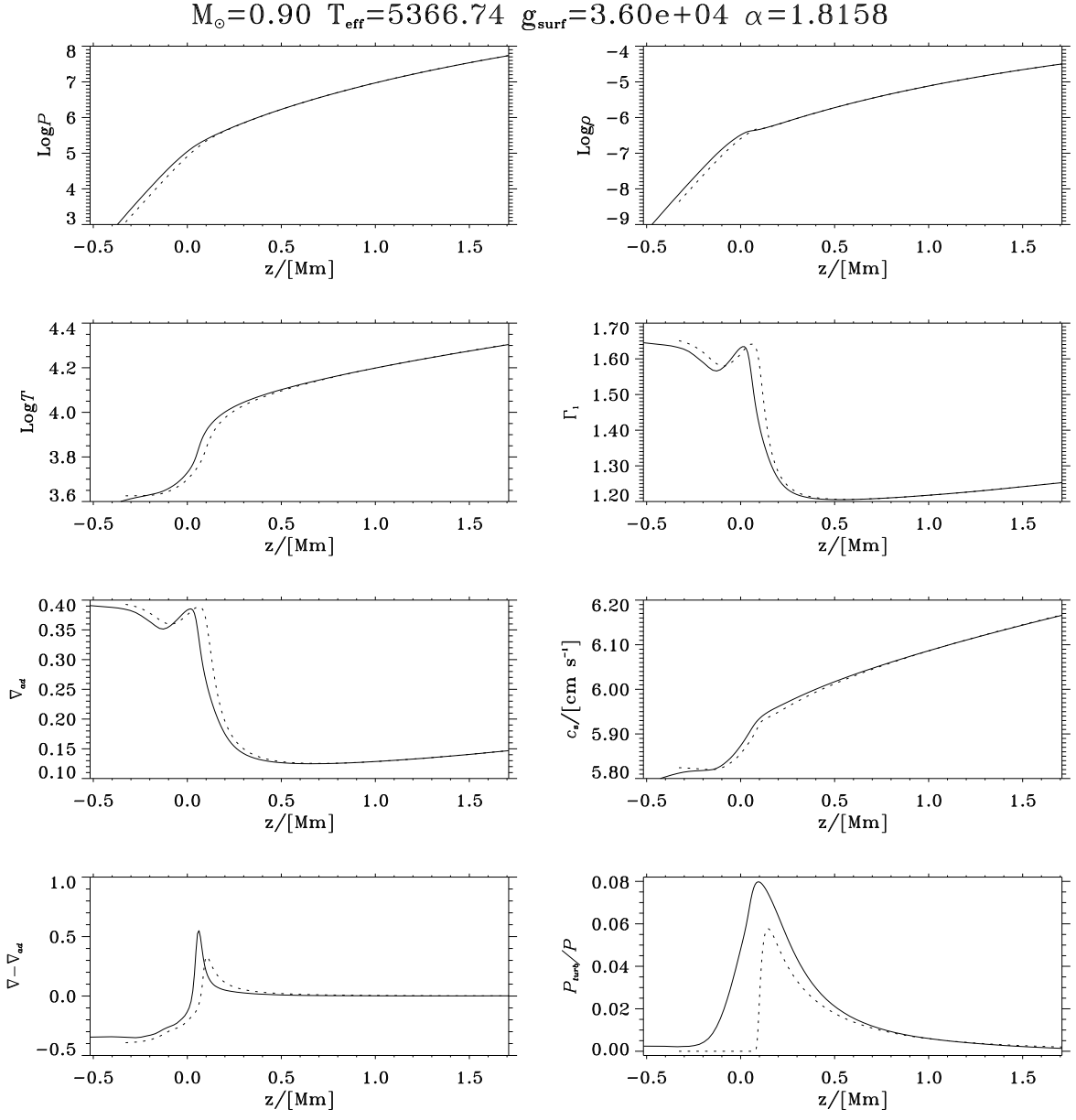

Fig. 6.4: Comparison of the horizontally averaged simulation (solid lines) and the matched 1D envelope model (dotted lines) for α Cen B.

6.2.5 η Boo

The matching program met some problems here, as the fluctuations in the bottom of the box got rather large, but the outcome (Fig. 6.5) does look quite reasonable anyway. The most interesting effect here is the pronounced distortion of the stratification (T, Γ_1, $\nabla_{\rm ad}$ in particular) with respect to the 1D model, due to the collective effect of turbulent pressure and inhomogeneity levitation of the atmosphere. Only half of the 1.27 Mm atmospheric expansion comes from Λ.

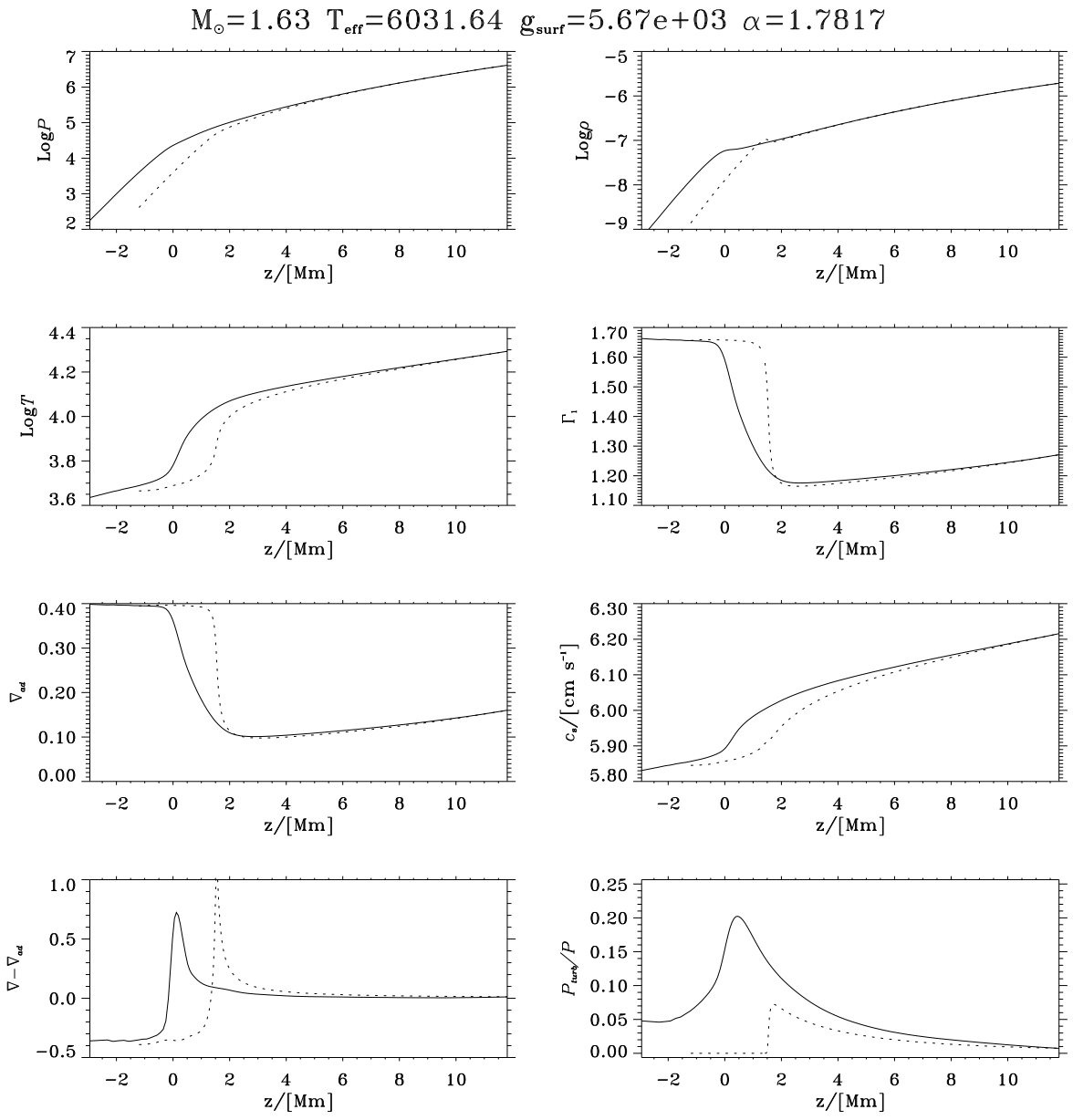

Fig. 6.5: Comparison of the horizontally averaged simulation (solid lines) and the matched 1D envelope model (dotted lines) for η Boo.

6.2.6 Procyon

Also Procyon gave problems with large temperature fluctuations at the bottom of the box, but again the results look reasonable. Procyon is the star displaying the most vigorous convection, which can most easily be inferred from the large turbulent to total pressure ratio, of 21.0% in the photosphere (see Tab. 5.1). Notice that MLT model of this match has a somewhat narrower superadiabatic peak than the simulation.

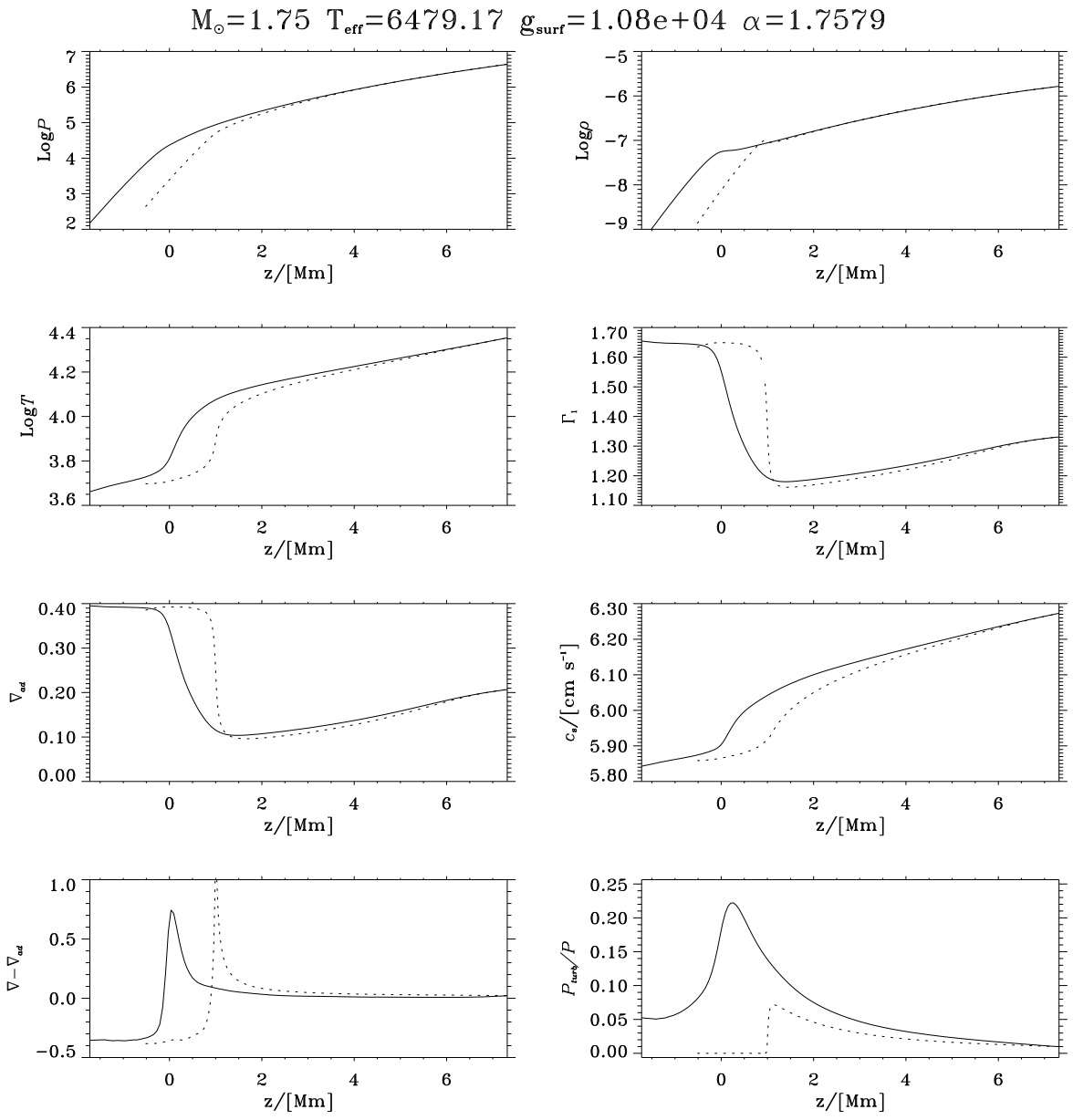

Fig. 6.6: Comparison of the horizontally averaged simulation (solid lines) and the matched 1D envelope model (dotted lines) for Procyon.

6.2.7 Star B

Fig. 6.7 displays a rather good match of the Star B case. Notice that the small ∇_s in the lower part of the simulation (lower left panel), is always larger for the MLT case, which is also the case for the matching of the other stars. The plot of the soundspeed, c_s, nicely illustrates where convection will affect the p-modes through stratification effects, and how the resonance cavity is expanded by the turbulent pressure.

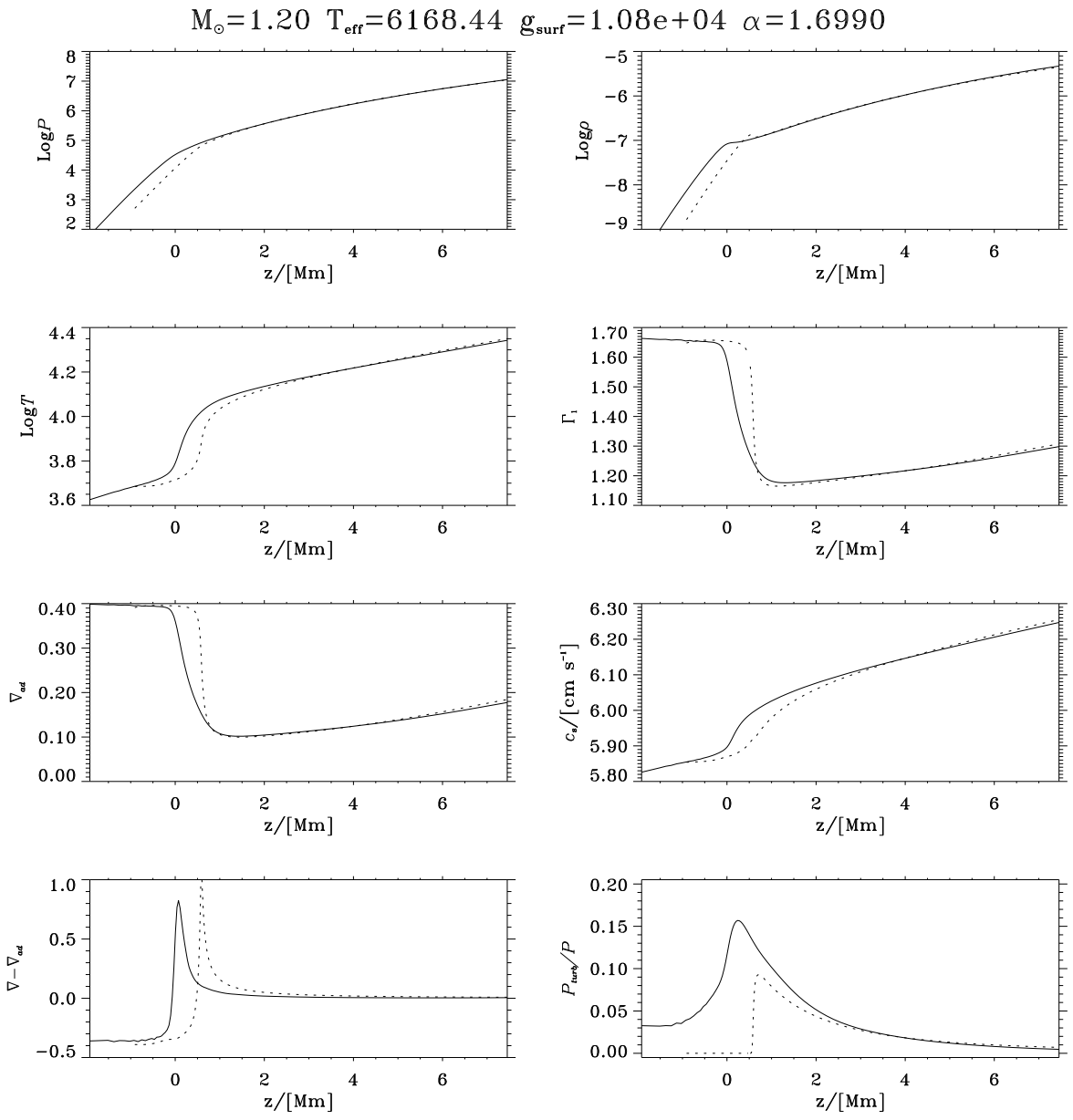

Fig. 6.7: Comparison of the horizontally averaged simulation (solid lines) and the matched 1D envelope model (dotted lines) for Star B.

Chapter 7

Morphology of convection as observed in the simulations

7.1 Below the surface

A lot of features of the convection observed in the simulations are common to all the stars I simulate, and worth a chapter of their own.

- The convection is dominated by the efficient cooling at the surface, which creates the downdrafts so typically for these simulations. The downdrafts and the abrupt cooling at the surface, can be seen in Fig. 7.2.

- The slowly up-welling warm plasma expands as it rises, thereby smoothing out the inhomogeneities, resulting in a rather smooth and laminar upflow.

- The downdrafts on the other hand are compressed as they evolve, and therefore enhance fluctuations. The downdrafts are much less ordered than the up-flows, and contain a much broader spectrum of fluctuations in hydrodynamical as well as thermodynamical quantities.

- Many of the downdrafts persist to the bottom of the simulation boxes (see Fig. 7.2).

- Overturning of plasma, from the up-flows into a downward motion, occurs at all depths, not only at the photospheric boundary layer (*cf.* Fig. 7.2). This is a straightforward consequence of the large density gradient in the atmospheres, combined with conservation of mass — what comes up must come down. This means that far from all of the up-flowing plasma ever makes it to the cooling surface. This fact is the main obstacle for convection to get efficient.

- Entrainment, surrounding plasma being sucked into the downdrafts, is very important for the stability of the downdrafts.

- The interface between up-flows and downdrafts generates a lot of vorticity, and this is the place to look for fully developed turbulence as can be seen from the picture on the front cover. This picture depicts the large-amplitude vorticity in the high-resolution solar simulation (*cf.* Sect. 8), and the high vorticity does a nice job in outlining the boundary between upflow and downdraft.
- As the downdrafts get narrower towards the bottom of the simulations, the turbulence eventually fills up the downdrafts.

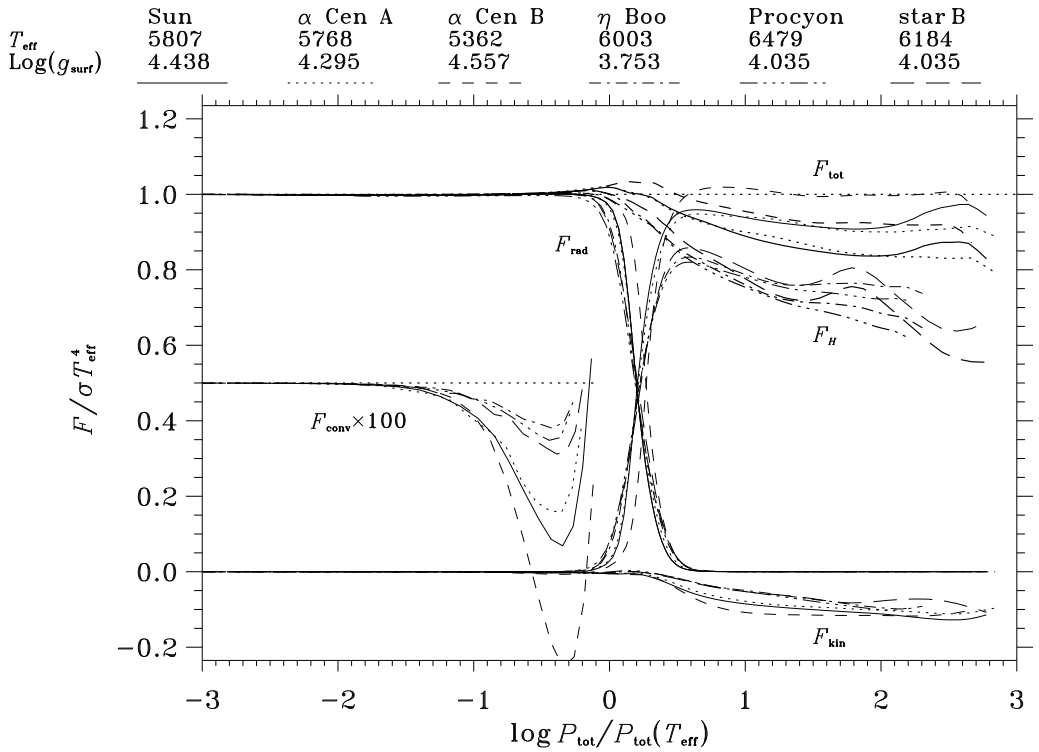

Fig. 7.1: This figure shows the various fluxes as function of logarithmic pressure scaled with the photospheric pressure, for the six stars as indicated above the plot. The enlarged part of the convective flux, $F_{\rm conv} = F_H + F_{\rm kin}$, illustrates the overshooting as described in Sect. 7.3.

- The convective flux consists of the enthalpy flux

$$F_H = \langle(\varepsilon\varrho + P_{\rm g})u_r\rangle_{\rm L} = \langle(\varepsilon + P_{\rm g}/\varrho)(\varrho u_r - \langle\varrho u_r\rangle)\rangle \tag{7.1}$$

and the kinetic energy flux

$$F_{\rm kin} = \tfrac{1}{2}\langle\varrho u_r u^2\rangle_{\rm L} = \tfrac{1}{2}\langle u^2(\varrho u_r - \langle\varrho u_r\rangle)\rangle \tag{7.2}$$

where L denotes Lagrangian averages, performed in order to filter out the effect of temporary net mass fluxes, which just causes flux to lap back and forth without really getting anywhere. All the fluxes are depicted in Fig. 7.1.

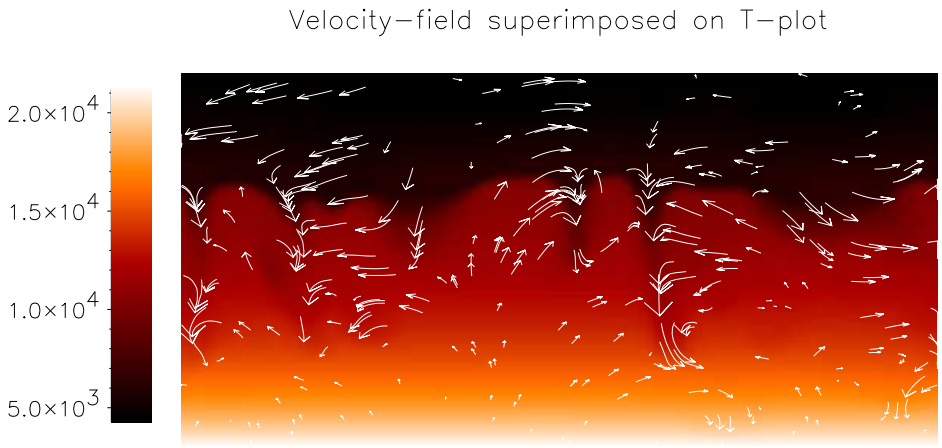

Fig. 7.2: The velocity field of a snapshot from the solar simulation, plotted atop of an image of the temperature. Yellow is warm, and red and black is cooler according to the colour scale to the left. Notice the warm upflows and the cool downdrafts extending down to the bottom of the simulation box. The photosphere is easily recognized as the dark edge.

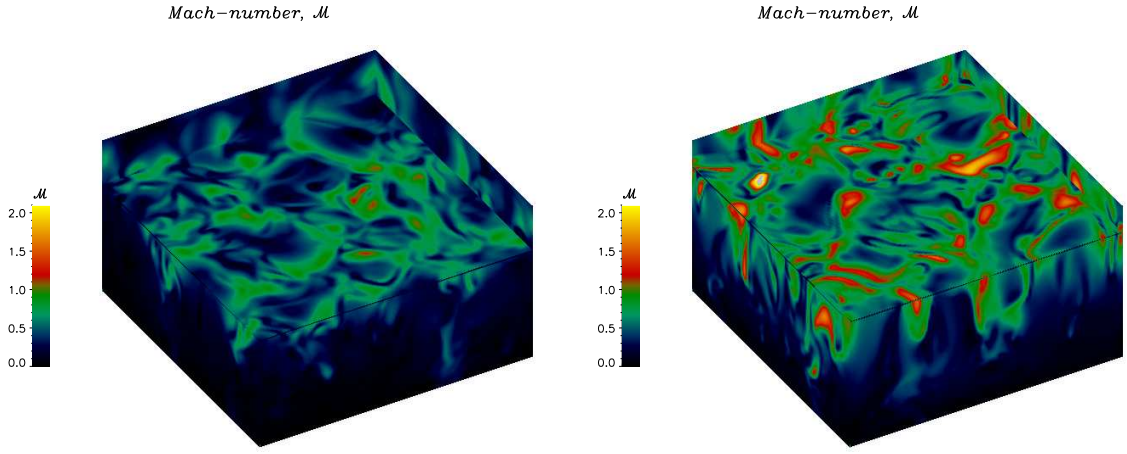

Fig. 7.3: Mach numbers, $\mathcal{M}$, for the α Cen A (left) and the η Boo (right) simulations. The α Cen A simulation barely reaches sonic flow speeds, whereas the η Boo simulation displays super sonic flows (red-yellow) at the boundaries between upflows and downdrafts.

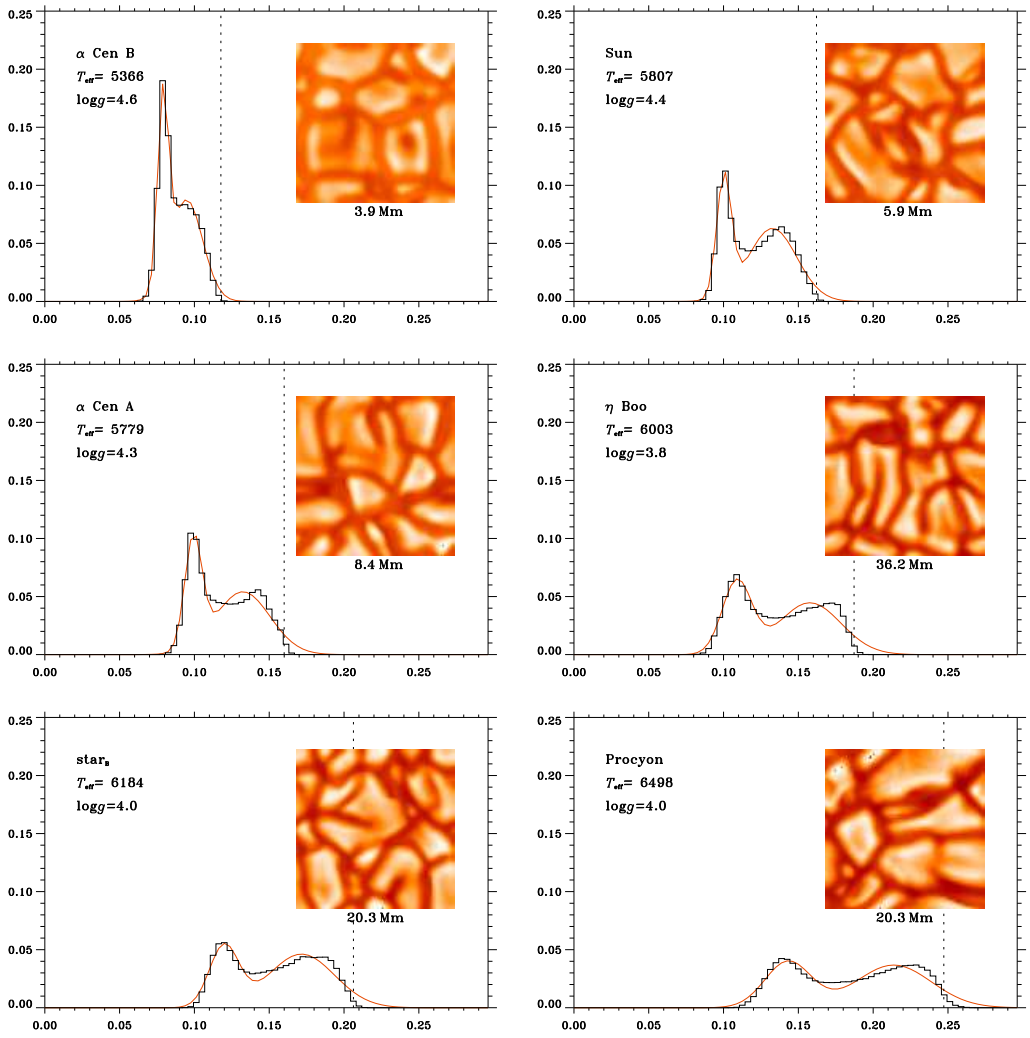

Fig. 7.4: This figure shows the distribution of surface intensities for each of the six stars, as well as images of snapshots of the surface intensity. The x-axis is the white light intensity in units of $\frac{1}{2} \times 10^{11}\,\mathrm{erg\,cm^{-2}}$, and the y-axis is the normalized frequency of occurrence of a given intensity. The vertical dotted line in each plot, marks the intensity where $I = \frac{1}{2}\sigma T_{\mathrm{eff}}^4$. The horizontal extent of the simulations is indicated below the snapshots. The red curves through the intensity distributions are just double-Gauss fits to highlight the symmetry of the low intensity peak and the asymmetry of the high intensity peak.

- The kinetic energy flux is negative everywhere due to an anti-correlation between filling factor (Fig. 7.11) and density contrast (Fig. 7.8) and amounts to about a tenth of the total flux in the convection zone.
- For the stars with convection more vigorous than the Sun, supersonic flows are normal in the photosphere, and even for the Sun the flow gets slightly supersonic now and then.
- The highest Mach numbers, $\mathcal{M} = |\boldsymbol{u}|/c_{\rm s}$, are found in the photosphere in the downdrafts, as can be seen from Fig. 7.3.

7.2 Granulation

The granular pattern in the surface intensity is a well known feature of the Sun (Scharmer 1989; Berger et al. 1995), but we have no direct observations of granulation on the surface of other stars except for some tentative observations with the *Hubble Space Telescope* of very large scale granulation on the red giant, Betelgeuse (Gilliland & Dupree 1996).

7.2.1 Spectral line asymmetries

It is however, possible to see the effect of granulation on the shapes of spectral lines (Bruning & Saar 1989). The variation of the vertical and horizontal velocity field with optical depth, and, very importantly, the correlation of this velocity field with temperature (Atroshcenko et al. 1989), distorts the otherwise symmetric line profiles. This distortion is quantified by the *bisector* — the bended line of symmetry of a spectral line (See Fig. 7.5). Because of the complexity of the phenomena, it is not possible in an unambiguous way to deduce the atmospheric structure from these asymmetries, and a more fruitful approach is to let observations and theory meet at the bisector, by calculating disk integrated bisectors based on numerical simulations of convection (Dravins & Nordlund 1990a; Dravins & Nordlund 1990b). This is a good, sensitive and very important test of the validity of the simulations that can be applied to all stars of sufficient brightness to allow for high dispersion spectroscopy — including the Sun. So far such tests have been encouraging, and a comparison between Fig. 7.5 and Bruls (1993, Fig. 8) shows a good agreement and leaves little room for further subgrid turbulence of importance.

I have not had the time to do more work on bisectors for the present thesis, but it will be the subject of forthcoming papers.

7.2.2 Granular patterns

So for the time being, our knowledge of the behaviour of granulation with changing stellar parameters comes from theoretical work — mainly from numerical simulations. Nordlund & Dravins (1990) have made atmospheric simulations of Procyon,

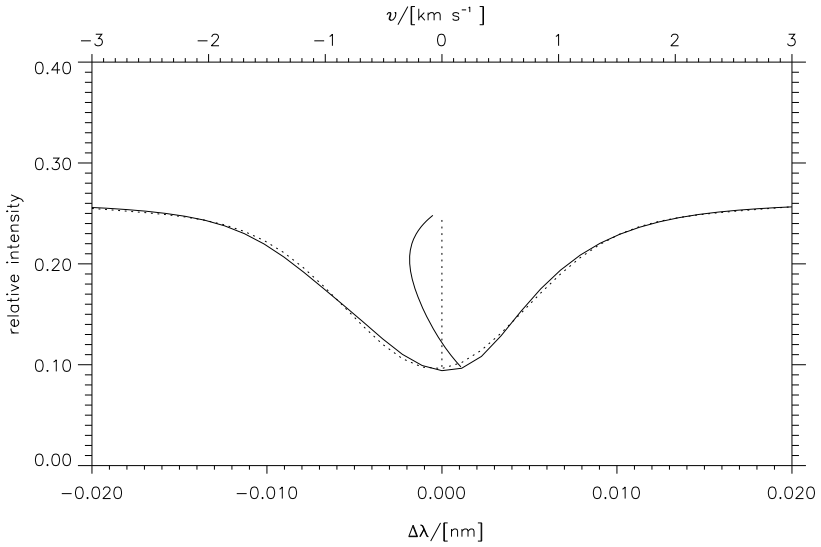

Fig. 7.5: An example of a bisector from one of my early solar simulations. This plot is for the 676.80 nm Ni I line from the 3.6576 eV, $z^3\mathrm{P}^0$ excited state. This line is chosen for its importance in various Doppler instruments for helioseismology and was also investigated by Bruls (1993). The dotted line is a Gaussian fit to the line. The bisector is plotted on the velocity scale and the line on the wavelength scale, which means that the bisector is exaggerated by a factor of three relative to the line profile.

α Cen A and α Cen B, as well as for β Hyi, a G2 IV dwarf of one solar mass, but lower surface gravity, representing the future Sun (Dravins et al. 1993). These simulations were carried out with an earlier version of the code I use for this work. Apart from the changes I have made to the atomic physics, the change in the expression of the standard opacity (from Eq. (4.17) to (4.18)) and the change to hyper diffusion (*cf.* Sect. 2.2) this previous version suffered from being anelastic. There were therefore no sound waves, shocks or supersonic flows present in these simulations. The neglect of compressibility will naturally have the largest effect on the stars with the most vigorous convection, *e.g.* Procyon in this case. The simulation domain was also restricted by the computer power at that time, to contain $32 \times 32 \times 32$ grid points, as opposed to the $50 \times 50 \times 82$. The increase in vertical resolution is particularly important, in order to resolve the very steep photospheric gradients, and computing the radiative transfer relies heavily on a good vertical resolution.

The distributions of surface intensities are depicted in Fig. 7.4. The plots in this figure are arranged in order of increasing convective vehemence from the upper left to the lower right corner, and this is also reflected in the behaviour of the intensities. The more violent the convection, the larger the intensity contrast between the bright upflows and the darker intergranular downflow. The simulations can furthermore

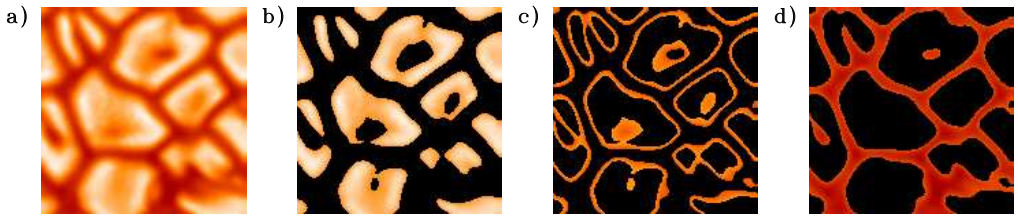

Fig. 7.6: Binary masking by intensity can reveal where the contributions to the intensity distribution come from. **a)** shows the full intensity picture of a snapshot from the Procyon simulation. In **b)** I have masked out everything but the brightest in the granules and **d)** shows the intergranular lanes. In **c)** I highlight the intermediate intensities, to show that not only do they stem from the edges of the granules but also from the breaking up of granules.

be paired in equi-violent pairs on the other diagonal: (α Cen A, Sun) and (Star B, η Boo).

It is interesting to see that the intergranular lanes exhibits a nicely Gaussian intensity distribution, whereas the warmer upflows show a skewed distribution with clear preference for the brightest. This is in accordance with the general behaviour of the convection in the simulations, that the plasma in the upflow is rather undisturbed, *i.e.* rises almost adiabatically and in unison, and then cools of very abruptly at almost the same height.

The intensity distribution in the upflows turn out to have a very sharp cutoff at $I = \frac{1}{2}\sigma T_{\rm eff}^4$ shown by the vertical dotted line in Fig. 7.4. This cutoff seems rather insensitive to the stellar parameters, whereas the mean of intensity distribution is

$$\frac{\sigma T_{\rm eff}^4}{2\pi} / \int_0^1 l(\mu)\mu \mathrm{d}\mu, \tag{7.3}$$

where $l(\mu) = I(\mu)/I(0)$ is the limbdarkening function. The integral is 0.393 for the sun, but seems to change more with stellar parameters than the position of the cutoff, which is a rather interesting result although it is not understood yet. The reason that the x-axis in Fig. 7.4 is $\frac{1}{2}I$ is a missing factor of two in the simulation code, which I was unaware of at the time of making the plot. Fortunately this missing factor do not have any effect on the simulations.

The broad distribution of say, the temperature or velocity in the downdrafts is due to the size of the granules in the following way: Plasma emerging in the middle of a large granule and overturning at the surface, has to travel farther to reach the intergranular lanes than plasma rising at the edge of a granule, and hence is subject to cooling for a longer time.

The intermediate part of the intensity distribution, between the bright granules and the darker lanes, has of course a contribution from the edges of the granules but the largest contribution comes from the breaking up of granules, as can be

seen in Fig. 7.6. Fig. 7.6 shows three large granules in the process of breaking up with the top one being farthest in the process. This granule has a nicely centered developing cool spot — a phenomena which is also known from observations of the

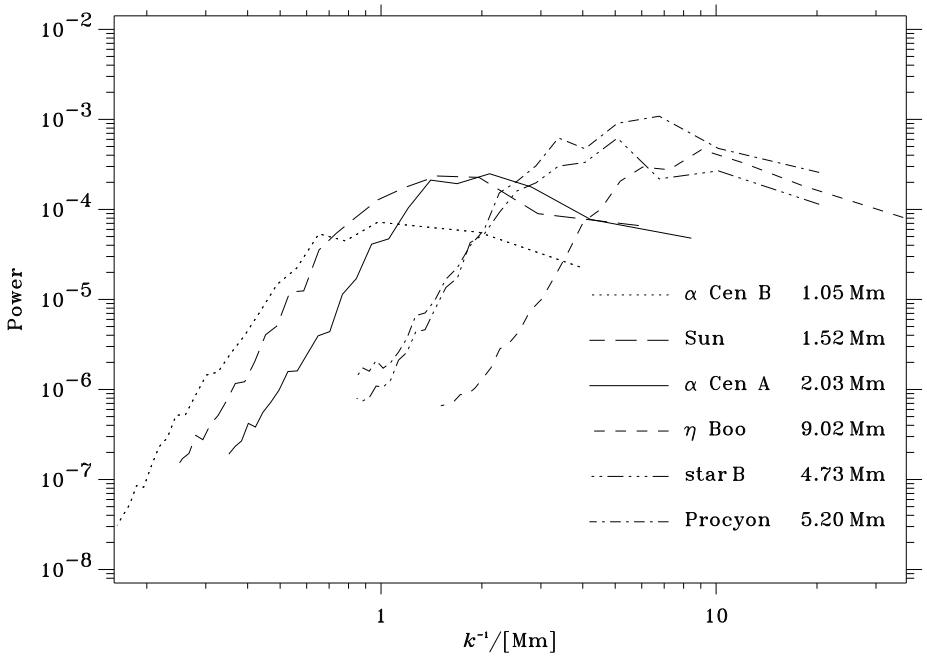

Fig. 7.7: This is a composite plot of the spectra of horizontal fluctuations in the surface intensities. The curves are the time-averaged power from Fourier transforming each of the snapshots that went into calculation of the distribution functions depicted in Fig. 7.4. The abscissa is the horizontal size of a feature, and the maximum in the distribution is the typical granular size.

Sun, as exploding granules. The development of most "exploding granules" is rather sedate though, and the term was coined when the resolution of observations of solar granulations was poor and only the largest and most violent occurrences could be seen. The dark spot appears as the granule gets too large for all the up-welling gas in the granule to reach the intergranular lanes. It is simply a topological problem caused by the r^2 dependence of an area and the r dependence of circumference. The gas in the middle of the granule will therefore get trapped at the surface for so long that it cools and gets sufficiently over-dense to sink back again and form a new downdraft. The vertical trapping is supplied by the density stratification, which only admits a small portion of the up-welling plasma to greater heights. A discussion of the phenomena together with comparisons between solar observations and simulations can be found in Rast (1995). The splitting of granules in Fig. 7.6 of the Procyon simulation occurs over the order of 30 minutes. Several recently split granules can be recognized as well.

The emerging intensity naturally reflects the horizontal temperature structure, but the largest temperature fluctuations, occuring at the transition from convective to radiative transport of the energy, is hidden at intermediate optical depths for cool stars as exemplified by the α Cen B simulation. For the other stars the convection is brought out in the daylight so to speak, and the largest fluctuations occurs at optical thin heights. This indicates that the optical depth at the top of the convection zone determines how vigorous the convection will be at the surface, as measured by the intensity contrast or the turbulent- to totalpressure ratio. There are at least two reasons for this. The escape of radiation makes the convective transport of energy less effecient which means that the velocities have to go up in order to maintain the flux. Second, the escape of radiation tends to enhance the temperature contrast in horizontal layers, although the same contrast with optical depth only increase slightly, *i.e.* the iso-τ surfaces are much more ondulated for stars with vigorous convection.

Just looking at the granular patterns in Fig. 7.4, it is hard to tell the stars apart from the shapes of the granules. Apart from the variation in intensity contrast and of course the size, the six snapshots could just as well be six instances of one simulation. Maybe a thorough statistical analysis can reveal some differences in the shapes, but for now the pattern looks rather universal.

The spectra of sizes of horizontal features, as depicted in Fig. 7.7 displays some rather broad maxima, corresponding to the typical granular size for each of the simulations. These typical sizes, as derived from analytical fits to the spectra, are indicated in the figure for each of the stars. In relation to such spectra it is very common to infer the presence of turbulence and compare with *Kolmogorov spectra* (*e.g.* Landau & Lifshitz 1987) of fully developed turbulence, but the impression from Fig. 7.4 can hardly be said to suggest fully developed turbulence so I will refrain from that and refer to Nordlund et al. (1997) for a discussion of turbulence in the solar photosphere. The main conclusion from this article is that the shape of the spectra is most likely caused by the edges of the granules and not by turbulence. A few of the points supporting this idea have been mentioned in Sect. 7.1.

7.3 Convective overshooting

The up-flowing plasma contains so much kinetic energy that it does not stop at the top of the convection zone, but penetrates far into the convectively stable layers.

Nesis & Mattig (1989) have deduced the RMS velocity field in the overshoot region from observations of spectral line profiles across the solar disk. Their analysis was restricted to describe the velocities in terms of a family of four-parameter functions with height. They find velocities smaller than ours by factors of about 3, and their horizontal velocities, probably restricted by the functional form, follows the vertical, in gross conflict with our results. There is not much to guide the analysis of this kind of observations if more than orders of magnitude estimates are wanted.

This merely to stress that this region in stellar atmospheres is extremely messy. As mentioned in relation to Fig. 7.5, I find it far more fruitful to let observations and theory meet as close to the observations as possible now we have the simulations.

In the abcense of chemical gradients, the top of the convection zone is defined by the *Schwarzschild criterion* (*e.g.* Kippenhahn & Weigert 1990), according to which a layer is stable against convection if

$$\nabla - \nabla_{\rm ad} = \nabla_{\rm s} < 0. \tag{7.4}$$

As the superadiabatic gradient can also be expressed by means of the entropy, S,

$$\nabla_{\rm s} = \frac{\partial S}{c_P \partial \ln P}, \tag{7.5}$$

Eq. (7.4) implies that the top of the CZ occurs at an entropy extremum — a minimum. If a layer is stable, a fluctuation will oscillate around its origin [referred to as g-modes for gravity modes. *e.g.* Christensen-Dalsgaard (1994)], whereas if the layer is unstable, the fluctuation will grow and be accelerated away from its origin.

- The correlation between velocity and density changes sign at the boundary of the CZ, thereby changing the effect of buoyancy. In Fig. 7.8, panel **a**, this can be seen from the density curves. Following the dashed upflow curve, we notice that that upflow approaches the surface while increasing its density deficiency (relative to the full horizontal average, shown with solid curves), but in the photosphere the upflows suddenly get over-dense and are accelerated back towards the CZ and vica verca.

- Because buoyancy now works against a rising motion, pressure forces will tend to redistribute the energy into the horizontal directions, resulting in large horizontal velocities persisting to greater heights than the vertical velocities (see Fig. 7.8, panel **b)**).

- - Or put in another way: The sudden increase in the density gradient in the photosphere (See Fig. 7.8, panel **a)**), forces an increase in the horizontal velocities in order to divert the vertical flow into the downdrafts, to maintain a zero net mass flux. Using the equation of mass conservation, Eq. (2.4) on an upflow and assuming steady state and neglecting the horizontal variation in density we get

  $$\frac{\partial u_{\rm h}}{\partial s} \simeq u_z \frac{\partial \ln \varrho}{\partial z} - \frac{\partial u_z}{\partial z}, \tag{7.6}$$

  where the density gradient is the dominating term in the upflow. s is distance in the horizontal direction. Despite the decreasing vertical velocities with height in the overshoot region, the increasing logarithmic density gradient makes the horizontal velocities grow until the gradient levels off allowing the horizontal velocities to decrease again.

- As a consequence of the above point, we also see very large pressure fluctuations, (panel **c**) of Fig. 7.8) which follows the horizontal velocities nicely (panel **b**)). The horizontal part of the momentum equation, Eq. (2.2), is

$$\frac{\partial \boldsymbol{u}_{\rm h}}{\partial t} = -\boldsymbol{u}_{\rm h} \cdot \nabla_{\rm h} \boldsymbol{u}_{\rm h} - \frac{P}{\varrho} \nabla_{\rm h} \ln P \tag{7.7}$$

  where the two terms on the right-hand side are depicted in panel **d**) of Fig. 7.8. This figure shows that the time derivative is rather small (though not vanishing) explaining the correspondence between pressure fluctuations and horizontal velocities.

- Correlation between velocity and temperature changes sign and gets very weak.

- Correlation between velocity and pressure grows. High pressure in the upflows, as shown in Fig. 7.8 panel **c**).

- The enthalpy flux turns slightly negative above the convection zone. Both energy and density correlation with vertical velocity change sign, but the speed and filling factor of the downward motions grows and results in a negative enthalpy flux.

- The kinetic energy flux remains negative, but decreases fast with height and is always smaller than the enthalpy flux.

- The total convective flux, $F_H + F_{\rm kin}$ is therefore small and negative in the overshoot region (*cf.* Fig. 7.1).

- The enlarged part of Fig. 7.1, showing the overshooting convective flux, displays a rather counter-intuitive behaviour. The more vigorous the convection the smaller the flux.

- The main feature of overshooting is the non-zero velocity field above the CZ. This velocity field gives rise to a turbulent pressure, supplying more than half of the total turbulent levitation of the atmosphere as shown in Fig. 7.10.

It has been attempted to model the overshoot region in 1D plane parallel atmosphere models, with a positive convective flux (Kurucz 1993; Kurucz 1992c) which is rather unphysical as also discussed by Castelli et al. (1997). As can be seen from Eq. (6.6) and (6.9) the enthalpy flux is proportional to $\nabla_{\rm s}$. The factor of proportionality contains the ad hoc assumptions that MLT is based on, but the proportionality is physical (Kippenhahn & Weigert 1990, chapter 30.4.1), which means that the convective flux (kinetic + enthalpy) has to get negative outside convection zones.

The convective flux in the overshoot region is not the most important phenomena of this region. After all it only amounts to less than one percent of the total flux.

The velocity field and the inhomogeneities are far more important. I have already shown how the velocity field is responsible for the horizontal pressure fluctuations, but the vertical velocities also contribute to the momentum balance with a turbulent pressure as shown in Sect. 2.1. Taking the time average of Eq. (2.10), the buoyancy term will vanish (if there is no net mass flux in or out of the simulation domain) and we can write down the equation of hydrostatic equilibrium

$$\frac{\partial}{\partial z}(P_{\rm turb} + \langle P_{\rm g}\rangle) = -\boldsymbol{g}\langle\varrho\rangle. \tag{7.8}$$

Turning around the expression and integrating

$$z_2 - z_1 = \int_{z_1}^{z_2} \frac{\partial P_{\rm tot}}{\partial z}\frac{{\rm d}z}{g\langle\varrho\rangle} \tag{7.9}$$

we just find the height interval we are integrating over, but it is also the distance the pressure has lifted the mass. If there were no pressure all the mass would be at z_1 due to the gravity.

This leads me to define the atmospheric levitation by turbulent pressure

$$\Lambda = \int_{z_1}^{z_2} \frac{\partial P_{\rm turb}}{\partial z}\frac{{\rm d}z}{g\langle\varrho\rangle}. \tag{7.10}$$

which summarizes the turbulent pressure contribution to hydrostatic support into a height. Keeping the $\varrho, T, P_{\rm g}$-stratification fixed, turning off the turbulent pressure would cause a decrease, Λ, in the atmospheric extent. The turbulent pressure does however alter this stratification so the actual difference in atmospheric height, between including and neglecting $P_{\rm turb}$, will not be Λ.

7.4 Comparison with the mixing-length formalism

In the mixing-length formalism the convective flux is transported by blobs of warm rising or cool sinking plasma. Such convective eddies[1] are assumed to be rather spherical or at least to have about the same dimensions in the radial as in the horizontal directions. There are various choices for the size of an eddy. The most common choice is a size, l, proportional to the local pressure scale height, $l = \alpha H_P$, where α is a scale-factor of order unity (Böhm-Vitense 1958). Another popular choice is that of density scale height, $l = \alpha H_\varrho$, and most recently, it has been suggested to use $l = \alpha z$, where z is the distance to the top of the convection zone (Canuto & Mazzitelli 1991; Canuto & Mazzitelli 1992). It is furthermore assumed that the blobs only travel a distance comparable to their own size before they dissolve

[1] That is eddy not Eddy. See (Adams 1989b, pp.323) for a thorough confusion on this subject.

and thermalize with their surroundings. This is obviously in conflict with simulations presented here, displaying correlation lengths far longer than a pressure scale height. In fact the downdrafts in the simulations persist to the bottom of the simulations although they often merge with others. This is a correlation over more than 10 pressure scale heights.

The upflow, just being what is in between the downdrafts, is even more correlated with height as it rises (almost) adiabatically before it cools of very abruptly at the surface.

A mixing-length proportional to the pressure (or rather the density) scale height is, however, justified. From the filling factors in Fig. 7.11 we see that the upflow always has approximately the same fraction of a horizontal area at its disposal (at least below the photospheric transition region). When the dense plasma flows upward from z_1 to z_2, a fraction $(\varrho_1 - \varrho_2)/\varrho_1$ has to leave the vertical flow (overturn) in order to maintain the density stratification. The fraction that has to leave, or the dilution of the upflow, per height, is consequently $\mathrm{d}\ln\varrho/\mathrm{d}z$ — the inverse of the density scale height, H_ϱ. So the mixing-length is in fact not the distance over which a convective eddy dissolves, but rather the distance over which the flow is diluted by overturning — a dilution length.

The superadiabatic gradients resulting from this assumption about the mixing-length, has a much larger spread in the peak values, as compared to the simulations, as can be clearly seen from Figs. 6.2 - 6.7. The ∇_s from the simulations are compared in Fig. 7.9, and here we see how the area of ∇_s, *i.e.* the overall effeciency of the convection as also the depth of the convection zone, mostly arise from a variation in the width of the superadiabatic peak. We also notice how this width is grouped by vehemence of the convection, exactly as the intensity contrasts in Fig. 7.4. The top of the convection zone is marked by $\nabla_\mathrm{s} = 0$ and is ordered in the same way, although less pronounced, as on the optical depth scale, with the more vigorous convection zones extending higher than the more sedate. Also the ∇_s from the simulations is smaller and seems to decrease faster with depth in the interior of the convection zone, as compared to the mixing-length models presented in Figs. 6.2 - 6.7. Whether this is just due to the differences in height and width of the ∇_s peak or if it is caused by more fundamental flaws in the mixing-length formulation is still unclear.

The neglect of kinetic flux might be the more dubious approximation, depending on the behaviour deep in the convection zone below the simulations. From Fig. 7.1 and 7.11 one could speculate that F_kin below the surface, stays almost a constant fraction of the total flux. The convective efficiency factor,

$$\gamma = \frac{\nabla - \nabla'}{\nabla' - \nabla_\mathrm{ad}}, \tag{7.11}$$

of MLT is a measure of the "heat excess" of the eddie with respect to its surroundings relative to its superadiabaticity (recall that $\nabla_\mathrm{ad} < \nabla' < \nabla$). As the enthalpy flux is proportional to $(\nabla - \nabla')$ the γ found from solving Eq. (6.13) neglecting F_kin will be too low. Including F_kin, F_H will be larger than the total flux and the actual

efficiency will be larger than that found from Eq. (6.13).

The $f_{\rm up} \neq \frac{1}{2}$ necessary to produce a non-vanishing $F_{\rm kin}$ introduces an asymmetry between the rising and sinking eddies and this will of course alter the enthalpy flux as well. How to include this asymmetry, in a self-consistent and realistic way, is unfortunately rather unclear.

I am convinced that such asymmetric models of convection, *i.e.* two-stream models, will be the next step towards realistic modelling of convection in stellar structure and evolution calculations. Such models have to contain a lot of assumptions about geometries and correlations, but with the simulations to lean upon, much more sophisticated and realistic assumptions can be made with a hopefully higher degree of generality and a closer connection to the micro physics. An inclusion of radiative effects in the photosphere, for example, would make a convection theory rather more trustworthy. Various versions of two-stream models have been investigated by *e.g.* Nordlund (1974; 1976) and Rieutord & Zahn (1995).

7.5 Comparison with the theory of Lydon, Fox and Sofia

This theory by Lydon et al. (1992) is in many ways a vast improvement over MLT formulations. It is based on simplified expressions for various correlations, derived from 3D numerical simulations. Based on these correlations, they derive expressions for the convective flux, as functions of the local state of the plasma. It is therefore a *local* theory, not taking into account the history of the plasma flows, just as the standard MLT. One of the improvements over MLT is the inclusion of the kinetic energy flux in the expression of the total convective flux

$$F_{\rm conv} = F_H + F_{\rm kin}, \tag{7.12}$$

together with the realization that $F_{\rm kin} < 0$.

This being said, there are also several shortcomings of their formulation. The most serious problem is the extent of their simulations. They only extend to the top of the convection zone, thereby omitting all the dynamics and the important cooling in the photosphere and overshoot region. Their evaluation of the radiative transfer in the diffusion approximation, is thereby justified. Most of the various simplified expressions for the correlations also break down near the surface, due to the very effects (inhomogeneities, radiative cooling, etc.) that determine the effeciency of the convection. The top and bottom boundaries of the simulations are furthermore impenetrable and stress-free (Chan & Sofia 1989), which means that they will reflect all flows, thereby having a large effect on the simulation.

As I find that a detailed and realistic treatment of the transition region in the photosphere is very important for the resulting efficiency of the convection, I consider the results of their approach to be rather dubious, despite their success in modelling both the Sun (Lydon et al. 1993b) and the α Cen system (Lydon et al. 1993a).

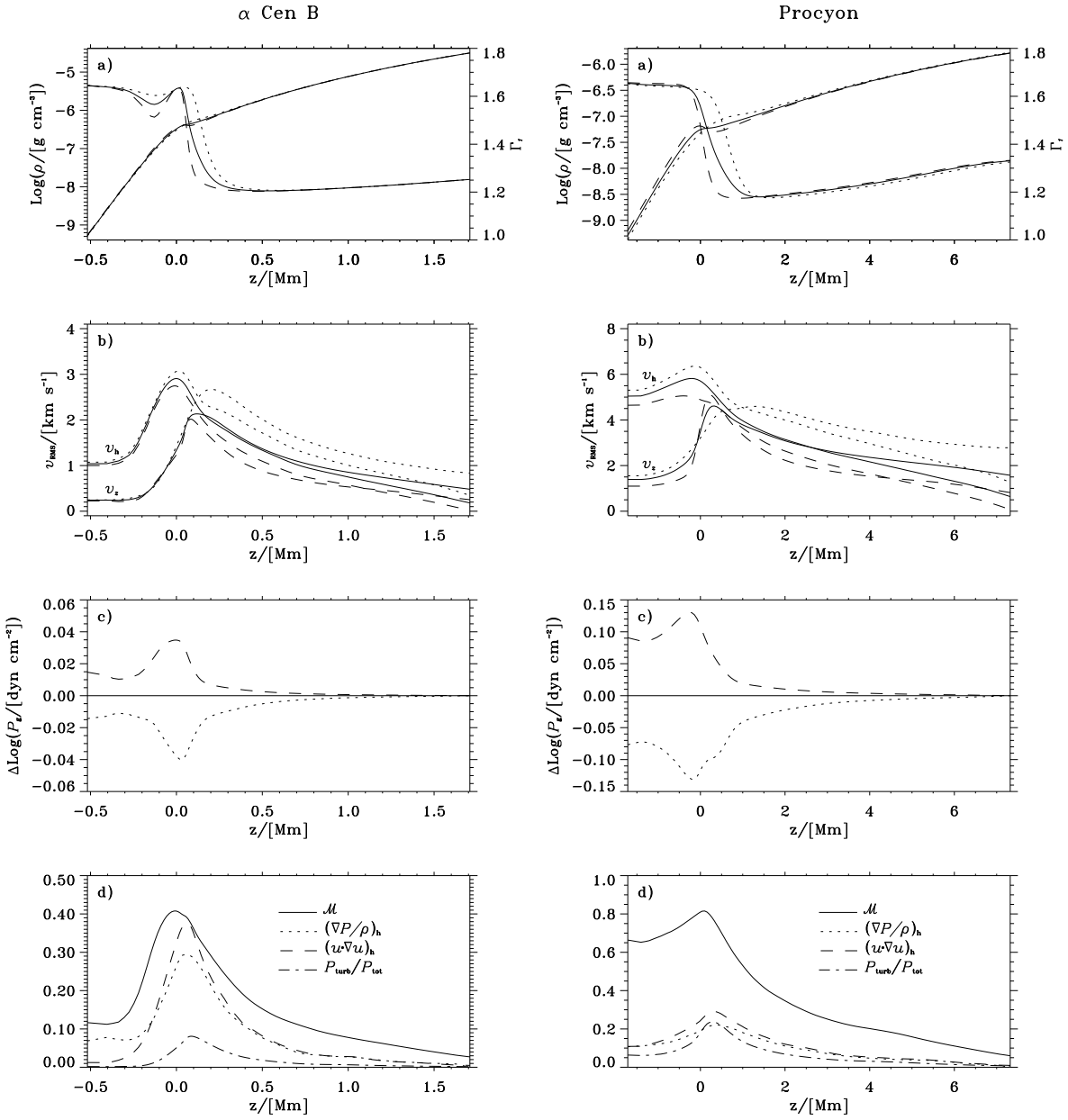

Fig. 7.8: A selection of hydrodynamical quantities for the star with the most sedate convection, α Cen B, and the star with the most vigorous convection Procyon. In panel **a)** the monotonically increasing curves shows the density, associated with the left axis. The other curves and the right axis shows the adiabatic exponent, Γ_1. In the upper panels, **a)**-**c)**, dotted lines shows horizontal averages over downflows, dashed lines over upflows and solid lines are total horizontal averages. Panel **c)** shows the gas pressure excess in the upflow and deficit in the downflow. The plots in panel **d)**, illustrating the momentum equation (2.2), are made from single snapshots and are not separated in up- and downflows. $\mathcal{M}$ is the Mach number, $|\boldsymbol{u}|/c_{\rm s}$, where $c_{\rm s}$ is the adiabatic sound speed, Eq. (2.20).

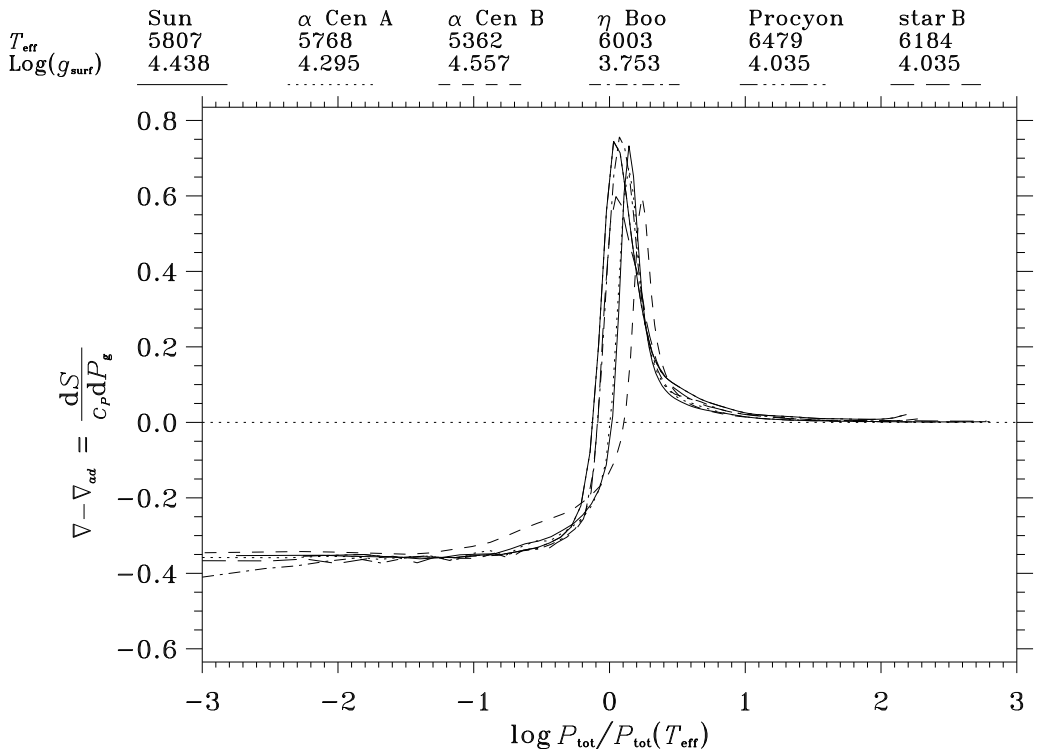

Fig. 7.9: The superadiabatic gradient for the six stars. Notice the different heights of the top of the convection zone (where the curves crosses the dotted zero-line) relative to the photosphere. The weakest convection occurs in α Cen B where the top of the CZ is buried just below the photosphere, whereas the stars with stronger convection has the top of their CZ fully exposed.

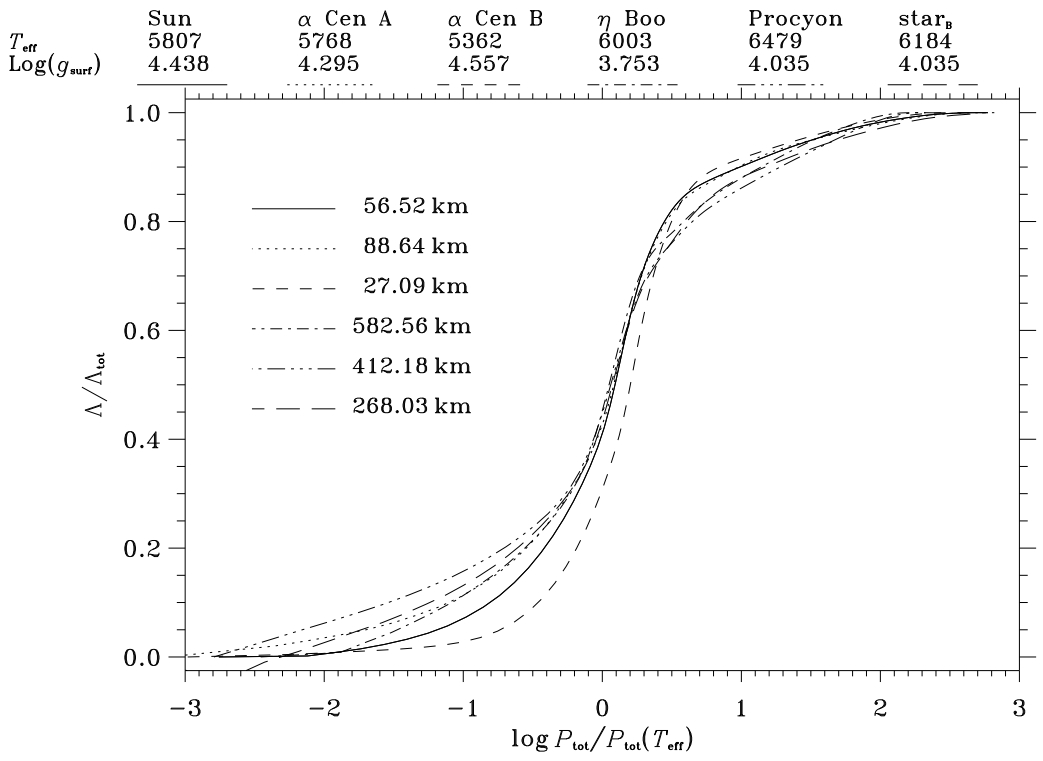

Fig. 7.10:The normalized atmospheric levitation, Λ, as calculated from Eq. (7.10). The total expansion of each of the atmospheres, is given to the left of the curves. Notice that at least half of the levitation occurs above the convection zone. The top of the convection zones can be inferred from Fig. 7.9.

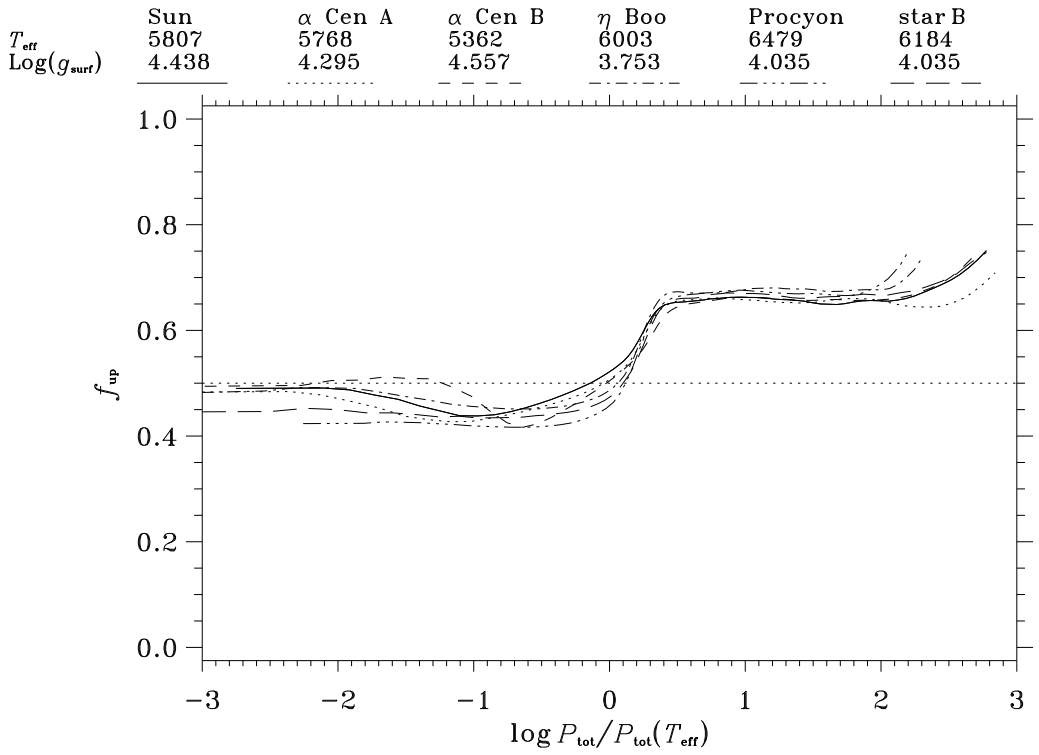

Fig. 7.11: The filling factors, $f_{\rm up}$, as function of logarithmic pressure scaled with the photospheric pressure, for the six stars as indicated above the plot.

Chapter 8

High-precision solar simulation

This simulation has been performed on a $100 \times 100 \times 82$ grid, with the solar composition, X=73.69%, Y=24.50% and Z=1.81%, as listed in Tab. 3.1, and a surface gravitation, $g_{\rm surf}= 2.740{\cdot}10^4$ cm s^{-2} (see Sect. 5.1.1). The effective temperature $T_{\rm eff}$ = 5776.6 K, has been carefully adjusted to give the observed value of 5777 K (see Sect. 5.1.1).

The motivation for such a high precision simulation are many. First of all it is instrumental for our understanding of the behaviour of p-modes in the upper layers of the Sun. A horizontally and temporal averaged version of the simulation (as described in Sect. 6) is matched to a standard 1D-envelope (*cf.* Sect. 6.2) and the ensuing combination is then used as input for the evaluation of p-mode frequencies. This has been done with great success (Rosenthal et al. 1998), helping to explain the discrepancy between observations and standard solar models.

8.1 The surface flux

As part of the nursing of the simulations, I routinely calculate detailed emergent fluxes, to make sure that the binned radiative transfer (*cf.* Sect. 4.2) reproduces the detailed version within a per cent. The radiative transfer is just evaluated for a single vertical slice, rather than for the whole simulation box to save CPU time.

Fig. 8.1 presents the results of such a calculation. The upper panel shows the full ODF spectrum, consisting of 100 Å wide giant lines, compared with the observations compiled and combined by Colina et al. (1996). The observations are smoothed with a 10 Å wide Gaussian, making it hard to compare directly with the rapidly fluctuating ODF spectrum. The two spectra do indeed look very dissimilar.

In panel **b)** I have therefore plotted the accumulated fluxes (trapezoidal integration), which are much easier and relevant to compare. The bumpy structure of the ODF spectra is due to the regular size and shape of the giant lines, and does not affect the good agreement.

In panel **c)** I have plotted the difference between the two accumulated fluxes in

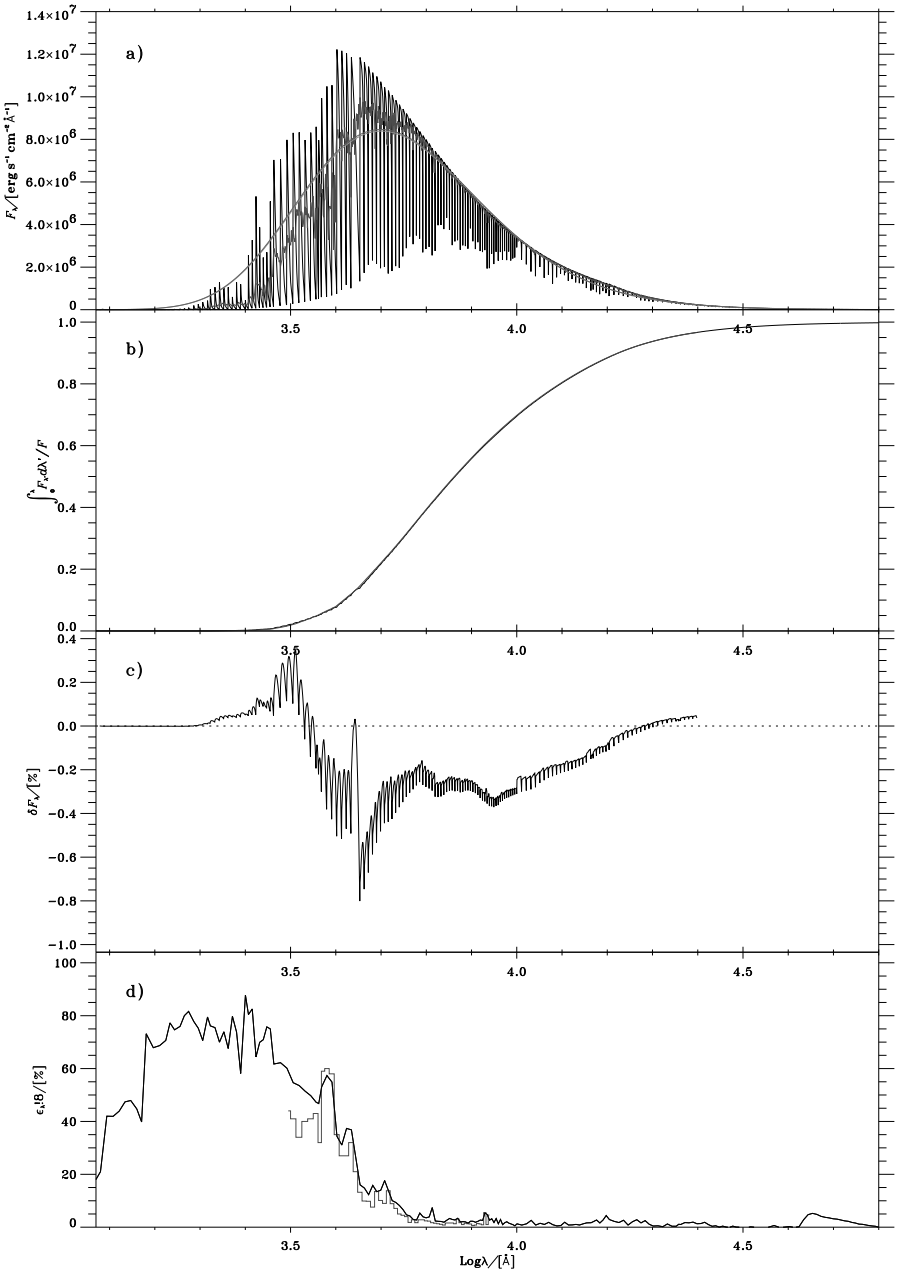

Fig. 8.1: A presentation of the emergent flux from the high-res solar simulation, and comparison with observations. Panel **a)** shows the full ODF spectrum together with the observed solar flux (Colina et al. 1996) (grey curve). I have also plotted the Planck curve for comparison. Panel **b)** is a plot of the accumulated fluxes for the simulation and the observations. Panel **c)** is a plot of the difference of the accumulated flux (simulation−observation) relative to the nominel flux. Panel **d)** depicts the line-blocking derived from the ODF spectrum and compares with observations (Michard 1950) (gray curve).

the sense (simulation−observation), in order to reveal the differences. This is just for a single snapshot and the picture changes noticeable with time, but the trend of too much UV flux and too little visible and IR flux is persistent.

In panel **d)** I have plotted the line blocking, defined as

$$\varepsilon_\lambda \equiv 1 - \frac{\int_{\lambda-\Delta\lambda}^{\lambda+\Delta\lambda} F_{\lambda'} d\lambda'}{\int_{\Delta\lambda}^{\lambda+\Delta\lambda} F_{\lambda'}^{\rm cont} d\lambda'}, \tag{8.1}$$

where $F_\lambda^{\rm cont}$ is the continuum flux and $\Delta\lambda$ is the resolution of the line-blocking coefficient. From this definition we see that ε_λ is the fraction of flux blocked out by the lines. The most serious problem in evaluating blocking coefficients, is the determination of the continuum flux in the UV part of the spectrum. As mentioned in Sect. 3.3.3 the UV is crowded with lines and it is impossible directly to observe a continuum. Derivation of line-blocking from observations in the UV therefore rests on assumptions and models, and should not be considered as directly observable quantities. The continuum fluxes for the simulation are just calculated as a linear interpolation between the low-opacity triangulation point of all the giant lines. This procedure can underestimate the line-blocking, by underestimating the continuum flux.

The observed line-blocking (Michard 1950) (gray curve in Fig. 8.1) follows the curve for the simulation, although the observed blocking is systematically a few percent lower. This can very well be a confirmation of my suspicion that the bf-absorption from metals is larger than previously assumed, so that a larger part of the missing UV opacity is due to bf-absorption rather than line absorption (see Sect. 3.3.3). The missing UV opacity problem (Kurucz 1992b) is not necessarily solved when the modelled fluxes agree with observations. Also the distribution between continuum and lines, as described by the line-blocking, has to agree.

The surface temperature of the simulation changes from minute to minute, so to make a fair comparison, I scale the simulation fluxes with the Planck functions of the actual and the nominel $T_{\rm eff}$.

The observations only extend up to 25 000 Å, which means they miss a fair amount of IR flux. I simply pad the simulation above 25 000 Å, to compensate for this, and then scale the whole patch to obtain the nominel flux corresponding to $T_{\rm eff} = 5777\,{\rm K}$ (see Sect. 5.1.1). The observations seems to give a too low total flux, even with the padded IR flux. As the observations are merged from a number of different atlasses obtained with different techniques, I do not find this discrepancy alarming.

8.2 The 1D envelope match

The matching to a 1D envelope model, is performed as described in Sect. 6.2, and a summary of the results can be seen in Fig. 8.2. The single most spectacular result

of this envelope match, is the derived depth of the convection zone:

$$d_{\rm CZ} = 28.61 \pm 0.02\%, \tag{8.2}$$

which is in good agreement with inversion of helioseismic observations, $28.7 \pm 0.1\%$ (Basu & Antia 1997) in accordance with similar results of Christensen-Dalsgaard et al. (1991). The uncertainty I state for my result (8.2), is based on RMS deviations of $d_{\rm CZ}$, when basing the envelope match on different subsets of the total timeserie.

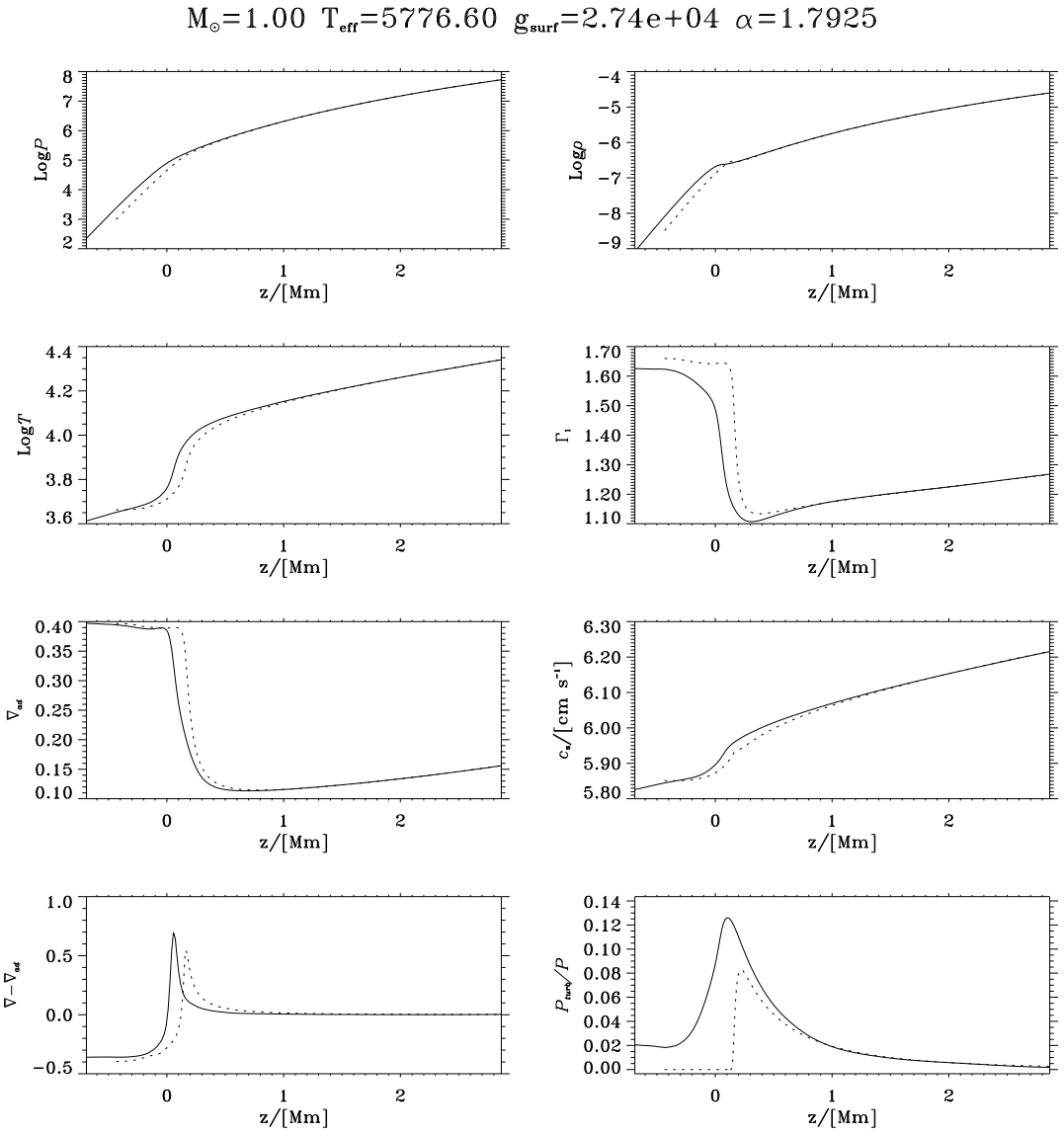

Fig. 8.2: Comparison of the horizontally averaged high precision solar simulation and the matched 1D envelope model. The solid line shows the averaged simulation and the dotted line is the matched envelope model.

If this result is not a highly unlikely coincidence (mind Murphy), this indicates several things. It indicates that the simulation gives a good representation of the solar atmospheric mean stratification, which implies both that the atomic physics is in good agreement with the real world, and that the hydrodynamics, as simulated with this rather modest grid resolution, captures the important effects. It also demonstrates that the matching procedure is sound, and that 3D RHD simulations can be used as upper boundary conditions for 1D stellar structure calculations.

The levitation of the atmosphere caused by the turbulent pressure, as calculated from Eq. (7.10) is $\Lambda = 69.4\,\mathrm{km}$. On the other hand, the difference in height between the 1D (with some turbulent pressure) and the 3D case, as inferred from the density plot in Fig. 8.2, is almost 100 km. This (substantial) extra levitation must be due to the effects of inhomogeneities and non-linear fluctuations (see Sect. 6.1). Comparing the P_{turb} plot in Fig. 8.2 with the levitations in Fig. 7.10, we notice that the 1D turbulent pressure can only supply about 20% of the full, 3D turbulent pressure levitation.

The superadiabatic gradient is somewhat larger in the simulations than in the MLT envelope (lower left panel of Fig. 8.2), which is in accordance with observations. Attempts to model the hydrogen Balmer line shapes, for example, suggest a large ∇_{s}, which can only be produced by MLT if $\alpha = 0.5$ (Fuhrmann et al. 1993). Such a low value is, however, incompatible with solar evolution calculations. Fuhrmann et al. (1993) also made the same analysis for Procyon and got the same result. My envelope match of Procyon on the other hand, suggests a slightly smaller ∇_{s} (see Fig. 6.6). As Procyon experiences a far more violent convection, as does the Sun, I am convinced that turbulent pressure levitation, large inhomogeneities and supersonic flows render MLT rather inadequate for describing phenomena as temperature sensitive as Balmer-line formation.

Chapter 9

Future prospects

This section is a small summary of projects that would be relevant to spend some time on in the future. One of the first and easiest things to do better is of course to increase the spatial resolution of the simulations, having the main effect of increasing the turbulent to total pressure ratio, but also altering the transport properties of the simulation somewhat.

And then it would also be nice to conclude the picture by including magnetic fields and maybe even rotation and sphericity.

9.1 Atomic physics

Much of this work has been concerned with updates of the EOS and opacity routines, but this has resulted in some inconsistency between the actual EOS and the EOS used for the computation of continuous opacities (see Sect. 3.1) — and the line opacity is based on yet a third EOS. This certainly needs some tidying up.

The release of the OP data makes it desirable to include these in a future version of the table program, which would also be consistent with the use of the MHD-EOS, having the same theoretical basis (see chapter 3). In Sect. 3.3.3 I also suggest the use of total opacity distribution functions, including both line and continuous absorption, or the equivalent total opacity sampling, which I would also like to carry out some day.

9.2 Other stars

Those were some of the improvements that can be done to the convection simulations, but there are also a lot of things that can be done to the analysis and further usage of these simulations. In this project I have only investigated the ($T_{\rm eff}$, $g_{\rm surf}$) plane. It would also be interesting to investigate the behaviour as function of Y and Z, the abundances of helium and heavier elements. In that respect it is interesting to look at all the aspects I have addressed in this thesis. The change in the

mixing-length parameter α with chemical composition, is needed to model in detail isochrones for globular clusters, which is one of the best tests of our stellar evolution models. We also need high-metallicity simulations to be able to investigate the α Cen system correctly.

Low-metallicity stars are interesting because they consist mainly of primordial matter, that is matter that has not been processed in other stars, but comes more or less directly from the Big Bang. In connection to that, it would be very valuable to have line profiles of for example Li and Be transitions in low-Z stars. The exact profile, perturbed differently by turbulence at different depths, is very important for abundance determinations.

And then I have only investigated a very small region it $T_{\rm eff}$ and $g_{\rm surf}$ in the solar neighbourhood. I would like to go beyond η Boo towards the giant area, and I also think it would be interesting to see what a very thin convection zone, so thin that it can be contained in the simulation box, looks like.

9.3 Confronting observations

There are also a lot of diagnostic work that has to be done, especially for the high precision solar simulation (Sect. 8). By diagnostic work, I here mean the computation of directly observable quantities, to assess the validity of the simulations, and in particular, to find out if the spatial resolution is sufficient.

The wings of the Balmer lines are one of these strong diagnostic tools, for the present with some discrepancy between theory and observations (Fuhrmann et al. 1993). For the solar case I also find it important to reconcile the observed limb darkening (Pierce & Slaughter 1977; Pierce et al. 1977) with that of models (Blackwell et al. 1995). Using the simulations as a basis for a determination of the solar iron abundance, might also reduce the current discrepancy between models and observations (Blackwell et al. 1995; Holweger et al. 1995).

Chapter 10

Conclusion

The thesis presented here has primarily resulted in a number of realistic simulations of stellar photospheres, ready for further analysis. The low-resolution simulations are intended as starters for high-resolution simulations of each of the six stars, with individual metallicities. These simulations can then be used as basis for a detailed analysis of observational phenomena, and as atmospheric structure models for oscillation calculations.

The six low-resolution simulations have already in this thesis proven invaluable in guiding the construction of a self-contained, self-consistent and physically reasonable convection formalism, for use in stellar structure and evolution calculations. I have touched many issues related to this project in chapter 7, *e.g.* the importance of the horizontal flows, the stratification in density, the significance of overshooting, and so on, but only on a phenomenological level. I did, however, show that many of the normal assumptions about convection are wrong.

In App. D I present a calibration of the mixing-length parameter, α, which suggests that it has to vary with atmospheric parameters, $T_{\rm eff}$ and $g_{\rm surf}$, in order to match the simulations.

In App. E I take a closer look on the use of T-τ relations as boundary condition for 1D stellar models, and stress the importance of using consistent combinations of atmospheric opacities and T-τ relations.

The kind of simulations presented here are instrumental for deriving simpler formulations of convection, for use in stellar structure and evolution codes, as well as for atmospheric models. Such a formalism should be made to reproduce the observations of the simulations, as well as the broad range of observations of the sun (helioseismological as optical), and can only then be used with confidence for other stars.

Bibliography

Adams, D. 1989a, "The hitchhiker's guide to the galaxy". In (Adams 1989c), 1

Adams, D. 1989b, "Life, the universe and everything". In (Adams 1989c), 311

Adams, D. 1989c, The more than complete hitchhiker's guide. Wings Books, New York

Alexander, D. R., Brocato, E., Cassisi, S., Castellani, V., Ciacio, F., Degl'Innocenti, S. 1997, "A theoretical approach to globular cluster low main sequence stars", A&A 317, 90

Alexander, D. R., Ferguson, J. W. 1994, "Low-temperature Rosseland opacities", ApJ 437, 879

Allen, C. W. 1973, Astrophysical quantities. The Athlone Press, 3 edition. p. 70

Allison, A. C., Dalgarno, A. 1969, "Photodissociation of vibrationally excited H_2, HD and D_2 by absorption into the continua of the Lyman and Werner systems", Atomic Data 1, 91

Anders, E., Grevesse, N. 1989, "Abundances of the elements: Meteoritic and solar", Geochim. Cosmochim. Acta 53(1), 197

Anosova, J., Orlov, V. V., Pavlova, N. A. 1994, "Dynamics of nearby multiple stars. The α Centauri system", A&A 292, 115

Atroshcenko, I. N., Gadun, A. S., Kostik, R. I. 1989, "Asymmetry of lines in the solar and Procyon spectra". In: R. J. Rutten and G. Severino (eds.), Solar and stellar granulation, NATO ASI series, Kluwer Academic Publishers, 135

Basu, S., Antia, H. M. 1995, "Helium abundance in the solar envelope", MNRAS 276, 1402

Basu, S., Antia, H. M. 1997, "Seismic measurement of the depth of the solar convection zone", M.N.R.A.S. 287, 189

Bates, D. R. 1952, "Absorption of radiation by an atmosphere of H, H^+ and H_2^+—semiclassical treatment", MNRAS 112(1), 40

Bell, K. L. 1980, "The free-free absorption coefficient of the negative ion of molecular hydrogen", J. Phys. B 13, 1859

Bell, K. L., Berrington, K. A. 1987, "Free-free absorption coefficient of the negative hydrogen ion", J. Phys. B 20, 801

Bell, R. A., Gustafsson, B. 1989, "The effective temperature and colours of G and K stars", M. N. R. A. S. 236, 653

Bell, R. A., Paltoglou, G., Tripicco, M. J. 1994, "The calibration of synthetic

colours", M.N.R.A.S. 268, 771
Berger, T. E., Schrijver, C. J., Shine, R. A., Tarbell, T. D., Title, A. M., Scharmer, G. B. 1995, "New observations of subarcsecond photospheric bright points", ApJ 454, 531
Berrington, K. A. (ed.) 1997, The opacity project, Vol. 2. Institute of Physics Publishing
Blackwell, D. E., Lynas-Gray, A. E. 1994, "Stellar effective temperatures and angular diameters determined by the infrared flux method (IRFM): Revisions using improved Kurucz LTE stellar atmospheres", A&A 282, 899
Blackwell, D. E., Lynas-Gray, A. E., Smith, G. 1995, "On the determination of the solar iron abundance using Fe I lines", A&A 296, 217
Bogges III, A. 1959, "The emission spectrum of H_2^+", ApJ 129(2), 432
Böhm-Vitense, E. 1958, "Über die Wasserstoffkonvektionszone in Sternen verschiedener Effektivtemperaturen und Leuchtkräfte", Zs. f. Astroph. 46, 108
Broad, J. T., Reinhardt, W. P. 1976, "One- and two-electron photoejection from H^-: A multichannel J-matrix calculation", Phys. Rev. A 14, 2159
Brown, C. M., Ginter, M. C., Johansson, S., Tilford, S. G. 1988, "Absorption spectra of Fe I in the 1500–3215 Å region", J. Opt. Soc. Am. B5, 2125
Brown, T. M., Gilliland, R. L., Noyes, R. W., Ramsey, L. W. 1991, "Detection of possible p-mode oscillations on Procyon", ApJ 368, 599
Bruls, J. H. M. J. 1993, "The formation of helioseismology lines. IV. The Ni I 676.8 nm intercombination line", A&A 269, 509
Brummell, N. H., Hurlburt, N. E., Toomre, J. 1996, "Turbulent compressible convection with rotation. I. Flow structure and evolution", ApJ 473, 494
Bruning, D. H., Saar, S. H. 1989, "Line asymmetries in late-type dwarf photospheres". In: R. J. Rutten and G. Severino (eds.), Solar and stellar granulation, NATO ASI series, Kluwer, 145
Buckingham, R. A., Reid, S., Spence, R. 1952, "Continuous absorption by the hydrogen molecular ion", M.N.R.A.S. 112, 382
Butler, K., Mendoza, C., Zeippen, C. J. 1993, "Atomic data for opacity calculations: XIX. The magnesium isoelectronic sequence", J. Phys. B 26, 4409
Canuto, V. M., Mazzitelli, I. 1991, "Stellar turbulent convection: A new model and applications", ApJ 370, 295
Canuto, V. M., Mazzitelli, I. 1992, "Further improvements of a new model for turbulent convection in stars", ApJ 389, 724
Castelli, F., Gratton, R. G., Kurucz, R. L. 1997, "Notes on the convection in the ATLAS9 model atmospheres", A&A 318(3), 841
Castelli, F., Kurucz, R. L. 1994, "Model atmospheres for Vega", A&A 281, 817
Chan, K. L., Sofia, S. 1989, "Turbulent compressible convection in a deep atmosphere. IV. Results of three-dimensional computations", ApJ 336, 1022
Chmielewski, Y., Friel, E., Cayrel De Strobel, G., Bentolila, C. 1992, "The 1992 detailed analyses of Alpha Centauri A and Alpha Centauri B", A&A 263, 219
Christensen-dalsgaard, J. 1982, "On solar models and their periods of oscillation",

M. N. R. A. S. 199, 735
Christensen-Dalsgaard, J. 1991, Lecture notes on stellar structure and evolution. Institut for Fysik og Astronomi, Århus, Denmark
Christensen-Dalsgaard, J. 1993, "Pulsation theory and stellar structure". In: W. W. Weis and A. Baglin (eds.), Inside the Stars, IAU Coll. 137, 483
Christensen-Dalsgaard, J. 1994, Lecture notes on stellar oscillations. Institut for Fysik og Astronomi, Århus, Denmark
Christensen-Dalsgaard, J., Bedding, T. R., Kjeldsen, H. 1995, "Modeling solar-like oscillations in η Bootis", ApJ 443, L29
Christensen-Dalsgaard, J., Däppen, W. 1992, "Solar oscillations and the equation of state", A&AR 4, 267. Chp. 2.1.
Christensen-Dalsgaard, J., Frandsen, S. 1983, "Stellar 5 min oscillations", Sol. Phys. 82, 469
Christensen-Dalsgaard, J., Gough, D. O., Thompson, M. J. 1991, "The depth of the solar convection zone", ApJ 378, 413
Cohen, E. R., Taylor, B. N. 1987, "The 1986 adjustment of the fundamental physical constants", Rev. Mod. Phys. 59(4), 1121
Colina, L., Bohlin, R. C., Castelli, F. 1996, "The 0.12–2.5μm absolute flux distribution of the sun for comparison with solar analog stars", AJ 112(1), 307
Cox, J. P., Guili, R. T. 1968, Physical principles, Vol. 1 of Principles of Stellar Structure. Gordon and Breach, Science Publishers
Cunto, W., Mendoza, C. 1993. TOPbase (6.0) User's Guide. Technical Report CSC-01-92, IBM Venezuela Scientific Center, Caracas, Venezuela. http://astro.u-strasbg.fr:80/OP.html
Däppen, W. 1980, "An analytical version of the free-energy minimization method for the equation of state of stellar plasmas", A&A 91, 212
Däppen, W., Mihalas, D., Hummer, D. G., Mihalas, B. W. 1988, "The equation of state for stellar envelopes. III. Thermodynamic quantities", ApJ 332, 261
de Boor, C. 1978, A practical guide to splines. Springer Verlag
de Jager, C., Neven, L. 1960, "The computation of partition functions in a stellar atmosphere", Bull. Astr. Inst. Netherlands 15(495), 55
Debye, P., Hückel, E. 1923, "Zur Theorie der Electrolyte", Physic. Zeit. 24(9), 185
Demarque, P., Guenther, D. B., van Altena, W. F. 1986, "The case of α Centauri: Mass, age and p-mode oscillation spectrum", ApJ 300, 773
Doughty, N. A., Fraser, P. A. 1966, "The free-free absorption coefficient of the negative hydrogen ion", Mon. Not. R. astr. Soc. 132, 267
Doughty, N. A., Fraser, P. A., McEachran, R. P. 1966, "The bound-free absorption coeficient of the negative hydrogen ion", Mon. Not. R. astr. Soc. 132, 255
Doyle, R. O. 1968, "The astrophysical significance of the continuous spectrum of the hydrogen quasi-molecule", ApJ 153, 987
Dravins, D., Lindegren, L., Nordlund, Å., Vandenberg, D. A. 1993, "The distant future of solar activity: A case study of β Hydri. I. stellar evolution, lithium abundance, and photospheric structure", ApJ 403, 385

Dravins, D., Nordlund, Å. 1990a, "Stellar granulation. IV. Line formation in inhomogeneous stellar photospheres", A&A 228, 184

Dravins, D., Nordlund, Å. 1990b, "Stellar granulation. V. Synthetic spectral lines in disk-integrated starlight", A&A 228, 203

Dziembowski, W. A., Pamyatnykh, A. A., Sienkiewicz, R. 1992, "Seismological test of standard solar models calculated with new opacities", Acta Astron. 42, 5

Eggleton, P. P., Faulkner, J., Flannery, B. P. 1973, "An approximate equation of state for stellar material", A&A 23, 325

Emanuele, A., Badiali, M., Cardini, D., Pannunzio, R., Bernacca, P. L. 1996, "Relative astrometry with Hipparcos: Double stars with orbital motion.", A&A 312, 1038

Fernandes, J., Neuforge, C. 1995, "α Centauri and convection theories", A&A 295, 678

Ford, A. L., Docken, K. K., Dalgarno, A. 1975, "The photoionization and dissociative photoionization of H_2, HD and D_2", ApJ 195, 819

Fuhrmann, K., Axer, M., Gehren, T. 1993, "Balmer lines in cool dwarf stars. I. Basic influence of atmospheric models", A&A 271, 451

Gavrila, M. 1967, "Elastic scattering of photons by a hydrogen atom", Phys. Rev. 163(1), 147

Gelly, B., Grec, G., Fossat, E. 1988, "Evidence for global pressure oscillations in Procyon and α Centauri". In: J. Christensen-Dalsgaard and S. Frandsen (eds.), Advances in helio- and asteroseismology, IAU Symp. 123, Kluwer, Dordrecht, 249

Gilliland, R. L., Dupree, A. K. 1996, "HST imaging of Betelgeuse". In: K. G. Strassmeier and J. L. Linskey (eds.), Stellar surface structure, IAU Symp. 176, Kluwer, Dordrecht, 165

Gough, D. O. 1976, "The current state of stellar mixing-length theory". In: E. A. Spiegel and J. P. Zahn (eds.), Convection in moderate-mass stars, Vol. 71 of Lecture Notes in Physics, IAU Coll. 38, Springer Verlag, Berlin, 15

Graboske, H. C., Harwood, D. J., Rogers, F. J. 1969, "Thermodynamic properties of nonideal gases. I. Free-energy minimization method", Physical Review 186(1), 210

Grevesse, N., Noels, A. 1992, "Cosmic abundaces of the elements". In: N. Prantzos, E. Vangioni-Flam, and M. Cassé (eds.), Origin and Evolution of the Elements, Cambridge University press, 15

Griem, H. R. 1964, Plasma spectroscopy. McGraw-Hill, New York

Griffin, R., Griffin, R. 1979. A photometric atlas of the spectrum of Procyon. $\lambda\lambda$ 3140–7470 Å. Technical report, Institute of Astronomy, Cambridge, England

Guenther, D. B., Demarque, P. 1993, "Evolution and seismology of Procyon", ApJ 405, 298

Gustafsson, B. 1973, "A fortran program for calculating "continuous" absorption coefficients of stellar atmospheres", Upps. Astr. Obs. Ann. 5(6)

Gustafsson, B., Bell, R. A., Nordlund, K. E. Å. 1975, "A grid of model atmospheres

for metal-defecient giant stars I.", A&A 42, 407

Hansen, J. E., Ziegenbein, B., Lincke, R., Kelly, H. P. 1977, "Observation and interpretation of the photoionization of the neutral iron atom FeI", J. Phys. B 10(1), 37

Harrington, R. S., Dahn, C. C., Kallarakal, V. V., Guetter, H. H., Riepe, B. Y., Walker, R. L., Pier, J. R., Vrba, F. J., Luginbuhl, C. B., Harris, H. C., Ables, H. D. 1993, "U.S. Naval Observatory photographic parallaxes - List IX", AJ 105, 1571

Henyey, L., Vardya, M. S., Bodenheimer, P. 1965, "Studies in stellar evolution. III. The calculation of model envelopes", ApJ 142(3), 841

Herzberg, G., Howe, L. L. 1959, "The Lyman bands of molecular hydrogen", Canadian J. Phys. 37, 636

Hofsaess, D. 1979, "Photoionization cross sections calculated by the scaled Thomas-Fermi method ($h\nu \leq 50$eV)", Atomic data and nuclear data tables 24(4), 385

Holweger, H., Kock, M., Bard, A. 1995, "On the determination of the solar iron abundance using Fe I lines. Comments on a paper by D. E. Blackwell et al. and presentation of new results for weak lines", A&A 296, 233

Houdek, G., Rogl, J., Balmforth, N. J., Christensen-Dalsgaard, J. 1994, "Excitation of solarlike oscillations in main-sequence stars". In: R. K. Ulrich, E. J. Rhodes, Jr., and W. Däppen (eds.), GONG'94: Helio- and astero-seismology from the earth and space, ASP, 641

Huebner, W. F., Merts, A. L., Magee Jr., N. H., Argo, M. F. 1977. Astrophysical opacity library. Technical Report LA-6760-M, Los Alamos Scientific Laboratory

Hummer, D. G., Mihalas, D. 1988, "The equation of state for stellar envelopes. I. An occupation probability formalism for the truncation of internal partitition functions", ApJ 331, 794

Iglesias, C. A., Rogers, F. R., Wilson, B. G. 1992, "Spin-orbit interaction effects on the Rosseland mean opacity", ApJ 397, 717

Inglis, D. R., Teller, E. 1939, "Ionic depression of series limits in one-electron spectra", ApJ 90(3), 439

Irwin, A. W., Fletcher, J. M., Yang, S. L. S., Walker, G. A. H., Goodenough, C. 1992, "The orbit and mass of Procyon", Publ. Astr. Soc. Pac. 104, 489

Isaak, G. R., Jones, A. R. 1988, "A spectroscopic search for oscillations in the 769.9 nm potassium line of Procyon". In: J. Christensen-Dalsgaard and S. Frandsen (eds.), Advances in helio- and asteroseismology, IAU Symp. 123, Kluwer, Dordrecht, 255

John, T. L. 1978, "Neutral bremsstrahlung from molecular hydrogen and nitrogen", A&A 67, 395

Karzas, W. J., Latter, R. 1961, "Electron radiative transitions in a Coulomb field", ApJS 6(55), 167

Kippenhahn, K., Weigert, A. 1990, Stellar structure and evolution. Astronomy and astrophysics library, Springer-Verlag, 1 edition

Kjeldsen, H., Bedding, T. R. 1995, "Amplitudes of stellar oscillations: The implica-

tions for asteroseismology", A&A 293, 87

Kjeldsen, H., Bedding, T. R., Viskum, M., Frandsen, S. 1995, "Solarlike oscillations in η Boo", AJ 109, 1313

Kurucz, R. L. 1992a, "Atomic and molecular data for opacity calculations", Rev. Mex. Astron. Astrofis. 23, 45

Kurucz, R. L. 1992b, "Finding the "missing" solar ultraviolet opacity", Rev. Mex. Astron. Astrofis. 23, 181

Kurucz, R. L. 1992c, "Model atmospheres for population synthesis". In: B. Barbuy and A. Renzini (eds.), The stellar population of galaxies, IAU, 225

Kurucz, R. L. 1993. Atlas9. Kurucz CD-ROM No. 13. Stellar atmosphere programs and $2\,\mathrm{km\,s^{-1}}$ grid

Kurucz, R. L., van Dishoeck, E. F., Tarafdar, S. P. 1987, "OH and CH continous opacity in solar and stellar atmospheres", ApJ 322, 992

Landau, L. D., Lifshitz, E. M. 1987, Fluid mechanics, Vol. 6 of Course of theoretical Physics. Pergamon Press, Oxford, England, 2nd edition

Langhoff, P., Sims, J., Corcoran, C. T. 1974, "Stieltjes-integral approximations to photoabsorption and dispersion profiles in atomic helium", Phys . Rev. A 10(3), 829. Table VIII

Lester, J. B. 1996, "The status of continuous opacities". In: S. J. Adelman, F. Kupka, and W. W. Weiss (eds.), Model atmospheres and spectrum synthesis, ASP, 19. Conf. Series, Vol. 108

Lindegren, L., Mignard, F., Soederhjelm, S., Badiali, M., Bernstein, H. H., Lampens, P., Pannunzio, R., Arenou, F., Bernacca, P. L., Falin, J. L., Froeschle, M., Kovalevsky, J., Martin, C., Perryman, M. A. C., Wielen, R. 1997, "Double star data in the Hipparcos catalogue.", A&A 323, L53

Lydon, T. J., Fox, P. A., Sofia, S. 1992, "A formulation of convection for stellar structure and evolution calculations without the mixing-length theory approximations. I. Application to the sun", ApJ 397, 701

Lydon, T. J., Fox, P. A., Sofia, S. 1993a, "A formulation of convection for stellar structure and evolution calculations without the mixing-length theory approximations. II. Application to α Centauri A and B", ApJ 413, 390

Lydon, T. J., Fox, P. A., Sofia, S. 1993b, "Improved solar models constructed with a formulation of convection for stellar structure and evolution calculations without the mixing-length theory approximations", ApJ 403, L79

Magain, P. 1983, "The missing UV opacity and the colours of solar-type stars", A&A 122(1-2), 225

Mathisen, R. 1984, "Photo cross-sections for stellar atmosphere calculations – compilation of references and data". In: Publication series, Institute of theoretical atrophysics, University of Oslo, Chapt. 1

Mendoza, C., Zeippen, C. J. 1987, "Radiative atomic data for neutral magnesium. II. Photoionization cross sections", A&A 179, 346

Michard, R. 1950, "On the energy distribution in the ultra-violet continuous spectrum of the sun", B. A. N. 11(416), 227

Mihalas, D. 1965, "Model atmospheres and line profiles for early-type stars", ApJS 9(92), 321

Mihalas, D. 1967, "The calculation of model stellar atmospheres", Meth. in Computational Phys. 7, 1

Mihalas, D. 1978, Stellar atmospheres. W. H. Freeman and Company, second edition

Mihalas, D., Däppen, W., Hummer, D. G. 1988, "The equation of state for stellar envelopes. II. Algorithm and selected results", ApJ 331, 815

Mihalas, D., Hummer, D. G., Mihalas, B. W., Däppen, W. 1990, "The equation of state for stellar envelopes. IV. Thermodynamic quantities and selected ionization fractions for six elemental mixtures", ApJ 350, 300

Moore, C. E. 1949. Atomic energy levels, I. ^{1}H-^{23}V. Technical report, US Dpt. of Comm., Nat. Bur. of Standards. Circ. 467

Moore, C. E. 1952a. Atomic energy levels, II. ^{24}Cr-^{41}Nb. Technical report, US Dpt. of Commerce, National Bureau of Standards. Circ. 467

Moore, C. E. 1952b. An ultraviolet multiplet table. Technical Report 488, National Bureau of Standards. Section 2

Moore, C. E. 1958. Atomic energy levels, III. ^{42}Mo-^{57}La; ^{72}Hf-^{89}Ac. Technical report, US Dpt. of Commerce, National Bureau of Standards. Circ. 467

Moore, C. E. 1959. A revised ultraviolet multiplet table. Technical report, National Bureau of Standards. Note 30

Moskalik, P., Dziembowski, W. A. 1992, "New opacities and the origin of the β Cephei pulsation", A&A 256, L5

Musielak, Z. E., Rosner, R., Stein, R. F., Ulmschneider, P. 1994, "On sound generation by turbulent convection: A new look at old results", ApJ 423, 474

Nave, G., Johansson, S., Learner, R. C. M., Thorne, A. P., Brault, J. W. 1994, "A new multiplet table for FeI", ApJS 94, 221

Nesis, A., Mattig, W. 1989, "The height dependence of vertical and horizontal velocities attributed to the convective overshoot in the solar atmosphere", A&A 221, 130

Noels, A., Grevesse, N., Magain, P., Neuforge, C., Baglin, A., Lebreton, Y. 1991, "Calibration of the Alpha Centauri system - metallicity and age", A&A 247, 91

Nordlund, Å. 1974, "On convection in stellar atmospheres", A&A 32, 407

Nordlund, Å. 1976, "A two component representation of stellar atmospheres with convection", A&A 50, 23

Nordlund, Å. 1982, "Numerical simulations of the solar granulation. I. Basic equations and methods", A&A 107, 1

Nordlund, Å. 1985, "Solar convection", Sol. Phys. 100, 209

Nordlund, Å., Dravins, D. 1990, "Stellar granulation. III. Hydrodynamic model atmospheres", A&A 228, 155

Nordlund, Å., Galsgaard, K. 1997, "A 3D MHD code for parallel computers", Journal of Computational Physics (in preparation)

Nordlund, Å., Spruit, H. C., Ludwig, H.-G., Trampedach, R. 1997, "Is stellar granulation turbulence?", A&A 328, 229

Nordlund, Å., Stein, R. F. 1990, "3-D simulations of solar and stellar convection and magnetoconvection", Comput. Phys. Commun. 59, 119

Pannekoek, A. 1938, "The hydrogen lines near the Balmer limit", M.N.R.A.S. 98, 694

Peach, G. 1967, "Total continuous absorption coefficients for complex atoms", Mem. R. astr. Soc. 71, 29

Perryman, M. A. C., Lindegren, L., Kovalevsky, J., Hog, E., Bastian, U., Bernacca, P. L., Creze, M., Donati, F., Grenon, M., Grewing, M., Van Leeuwen, F., Van Der Marel, H., Mignard, F., Murray, C. A., Le Poole, R. S., Schrijver, H., Turon, C., Arenou, F., Froeschle, M., Petersen, C. S. 1997, "The Hipparcos catalogue.", A&A 323, L49

Petersen, J. O. 1990, "Studies of Cepheid-type variability. VII. Stellar opacities and multimode Cepheid variables", A&A 238, 160

Petreymann, E. 1974, "Line-blanketing and model stellar atmospheres", A&A 33, 203

Pierce, A. K., Slaughter, C. D. 1977, "Solar limb darkening. I: $\lambda\lambda$(3033–7297)", Sol. Phys. 51, 25

Pierce, A. K., Slaughter, C. D., Weinberger, D. 1977, "Solar limb darkening in the interval 7 404–24 018 Å, II", Sol. Phys. 52, 179

Pillet, P., van Linden van den Heuvell, H. B., Smith, W. W., Kachru, R., Tran, N. H., Gallagher, T. F. 1984, "Microwave ionization of Na Rydberg atoms", Phys. Rev. A 30(1), 280

Provencal, J. L., Shipman, H. L., Wesemael, F., Bergeron, P., Bond, H. E., Liebert, J., Sion, E. M. 1997, "Wide field planetary camera 2 photometry of the bright, mysterious white dwarf Procyon B", ApJ 480, 777

Rast, M. P. 1995, "On the nature of "exploding" granules and granule fragmentation", ApJ 443, 863

Rieutord, M., Zahn, J. P. 1995, "Plumes in stellar convection zones", A&A 296, 127

Rogers, F. J., Swenson, F. J., Iglesias, C. l. A. 1996, "OPAL equation-of-state tables for astrophysical applications", ApJ 456, 902

Rogers, F. R., Iglesias, C. A. 1994, "Astrophysical opacity", Science 263, 50

Rosenthal, C., Christensen-Dalsgaard, J., Nordlund, Å., Stein, R. F., Trampedach, R. 1998, "Convective contributions to the frequencies of solar oscillations", A&A (submitted)

Rott, N. 1990, "Note on the history of the Reynolds number", Annu. Rev. Fluid Mech. 22, 1

Sawey, P. M. J., Berrington, K. A. 1992, "Atomic data for opacity calculations", J. Phys. B 25, 1451

Scharmer, G. B. 1989, "High resolution granulation observations from La Palma: Techniques and first results". In: R. J. Rutten and G. Severino (eds.), Solar and stellar granulation, NATO ASI series, Kluwer, Dordrecht, 161

Seaton, M. J. (ed.) 1995, The opacity project, Vol. 1. Institute of Physics Publishing

Sneden, C., Johnson, H. R., Krupp, B. M. 1976, "A statistical method for treating

molecular line opacities", ApJ 204, 281
Spanier, J., Oldham, K. B. 1987, An atlas of functions, Chapt. 62, 653. Hemisphere Pub., Washington, D.C.
Stancil, P. C. 1994, "Continous absorption by He_2^+ and H_2^+ in cool white dwarfs", ApJ 430, 360
Steffen, M. 1985, "A model atmosphere analysis of the F5 IV-V subgiant Procyon", A&AS 59, 403
Stein, R. F. 1989, "Convection and waves". In: R. J. Rutten and G. Severino (eds.), Solar and stellar granulation, Kluwer Academic Publishers, 381
Stein, R. F., Nordlund, Å. 1989, "Topology of convection beneath the solar surface", ApJ 342, L95
Stein, R. F., Nordlund, Å. 1990, "Convection and its influence on oscillations". In: D. Gough and J. Toomre (eds.), Challenges to theories of the structure of moderate-mass stars, Vol. 388 of Lecture Notes in Physics, Springer Verlag, Berlin, 195
Stein, R. F., Nordlund, Å., Brandenburg, A. 1997. difcof.f. Private communications
Stix, M. 1989, The Sun. Astronomy and astrophysics library, Springer Verlag, Berlin
Strikwerda, J. C. 1989, Finite difference schemes and partial differential equations. Mathematics Series, Wadsworth & Brooks/Cole Advanced Books & Software, Pacific Grove, California
Tarafdar, S. P., Vardya, M. S. 1969, "Opacity cross sections for He, C, N, O and H^-". In: O. Gingerich (ed.), Theory and observation of normal stellar atmospheres, Harvard Smithsonian, The M.I.T. Press, Cambridge, 143
Trampedach, R., Christensen-Dalsgaard, J., Nordlund, Å., Stein, R. F. 1998a, "Calibrating the mixing-length with 3D RHD simulations", A&A (in preparation)
Trampedach, R., Christensen-Dalsgaard, J., Nordlund, Å., Stein, R. F. 1998b, "On using T-τ relations as outer boundary condition for stellar models", A&A (in preparation)
Trampedach, R., Däppen, W., Rogers, F., Baturin, V. A. 1997, "A comparative study of the MHD and OPAL equations of state", A&A (in preparation)
Traving, G., Baschek, B., Holweger, H. 1966, "Tabellen für die Berechnung von Zustandssummen", Abh. Hamburger Sternw. Bergedorf VIII(1), 3
Tsuji, T. 1973, "Molecular abundances in stellar atmospheres. II.", A&A 23, 411
Unsöld, A. 1955, Physik der Sternatmosphären. Springer Verlag. p. 168
van Linden van den Heuvell, H. B., Gallagher, T. F. 1985, "Ionization of Na atoms by 8-GHz electric fields", Phys. Rev. A 32(3), 1495
Vardya, M. S. 1965, "Thermodynamics of a solar composition gaseous mixture", M. N. R. A. S. 129, 205
Vardya, M. S. 1966, "Pressure dissociation and the hydrogen molecular ion", M. N. R. A. S. 134, 183
Vernezza, J. E., Avrett, E. H., Loeser, R. 1981, "Structure of the solar chromosphere. III. Models of the EUV brightness components of the quiet sun", ApJS 45, 635
Victor, G. A., Dalgarno, A. 1969, "Dipole properties of molecular hydrogen", J.

Chem. Phys. 50, 2535. Table III

Wiese, W. L., Kelleher, D. E., Paquette, D. R. 1972, "Detailed study of the Stark broadening of Balmer lines in a high-density plasma", Phys. Rev. A 6(3), 1132

Willson, R. C., Hudson, H. S. 1988, "Solar luminosity variations in solar cycle 21", Nature 332, 810

Wishart, A. W. 1979, "The bound-free photo-detachment cross-section of H^-", Mon. Not. R. astr. Soc. 187, 59

Appendix A

Opacity updates

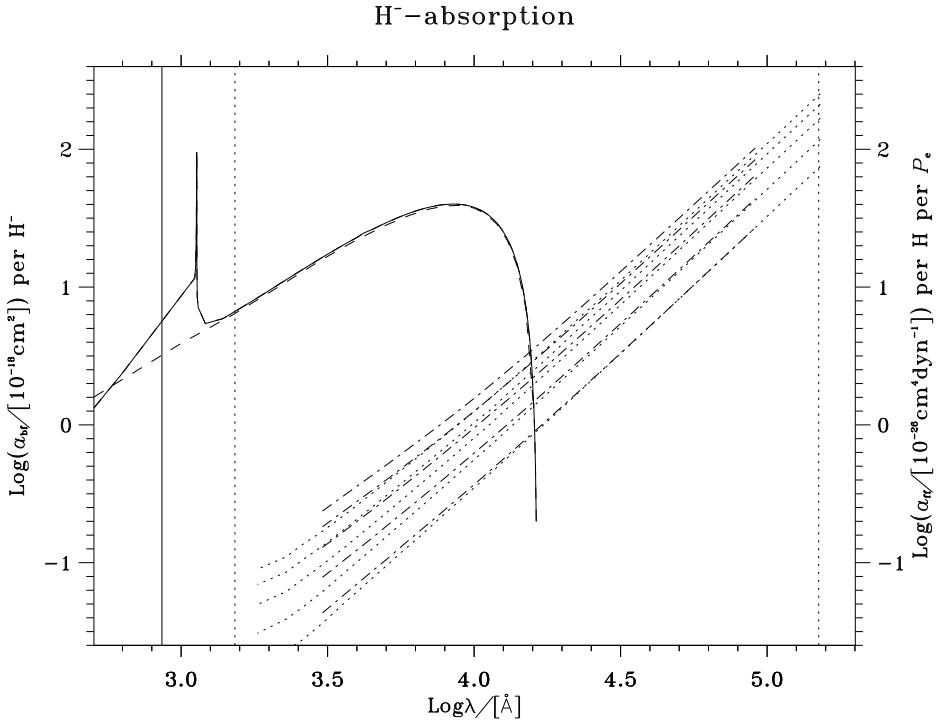

Fig. A.1: The solid line shows the currently used bf absorption (left axis) by the H^- ion (Broad & Reinhardt 1976). The thin resonance is left out in the calculations, but I have included it in this plot to show a less commonly known feature of the H^- opacity. The dashed line is the former bf absorption (Doughty et al. 1966). The dotted lines are ff absorption (right axis) (Bell & Berrington 1987) for $\Theta = 5040/T$ =0.5, 0.8, 1.2, 1.6, 2.0 from bottom to top. The dot-dashed lines are the old values (Doughty & Fraser 1966).

This appendix is a graphical presentation of the changes I have made to the continuous opacities. These new opacities are used both in the convection simulations

and in the 1D envelope models.

All the plots presented here have the same x-scale, to make it easier to compare between them. The vertical lines are also common to all the plots, where the dotted lines show the extent of the previously used wavelength interval, and the solid

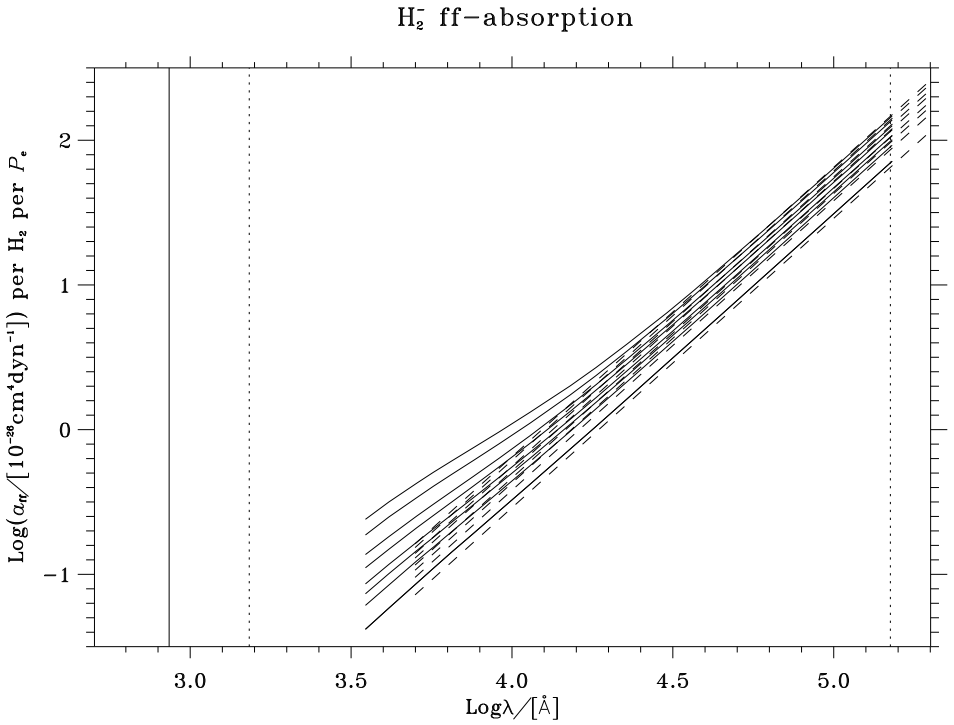

Fig. A.2: Comparison of the H_2^- absorption. The solid lines are the present values (Bell 1980) and the dashed lines show the old values (John 1978), for $\Theta = 5040/T$ =0.5, 0.8, 1.0, 1.2, 1.6, 2.0, 2.8, 3.6 from bottom to top. Stimulated emission is included.

vertical line is the present extent, with the upper bound being the boundary of the plot.

The bf absorption from the H^- ion (Fig. A.1) is generally slightly larger in the new version. The new absorption below 1 200Å is due to the inclusion of excited target states, *e.g.* the final atomic hydrogen state is an excited state. The spike at 1 130.5Å is the resonance with the first excited state in the hydrogen atom, and there are in fact several such resonances with the higher excited states at lower wavelengths, but they give much smaller spikes and are smoothed out in this plot. Because of the rather coarse wavelength resolution (30Å near the resonance) used for the continuous opacity calculations and the linear interpolation to the 12 times finer ODF wavelength mesh, and because one of the wavelength points actually is situated at the centre of the resonance, the opacity would be largely overestimated if including this very thin resonance. It has therefore been left out, and only the absorption edge remains. The ff absorption is consistently lower in the new version,

especially towards shorter wavelengths and lower temperatures.

The changes in the ff-absorption by the H_2^- molecular ion (Fig. A.2), mostly

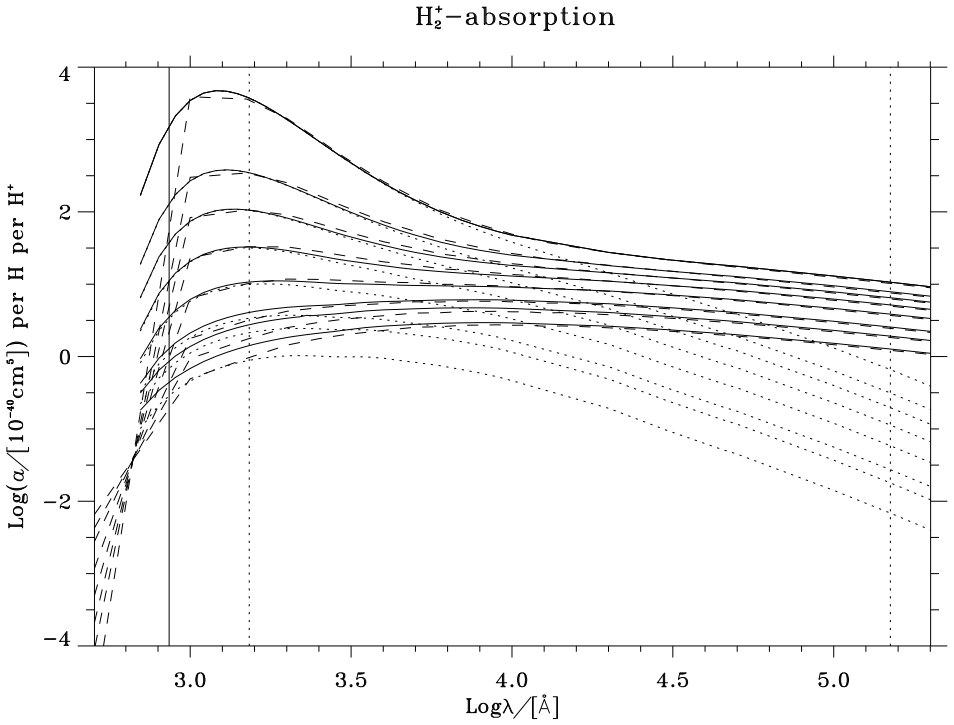

Fig. A.3: In this plot the solid line is the combination of bf and ff absorption by the H_2^+ molecular ion, including stimulated emission (Stancil 1994). The dotted line shows the bf part of this absorption. For comparison is plotted the previously used interpolation of Mihalas (1965) based on the semiclassical results of Bates (1952) (dashed lines). The curves are for $\Theta = 5040/T$ =0.1, 0.2, 0.3, 0.4, 0.6, 0.8, 1.2 from bottom to top.

affect the low-temperature/short-wavelength region, enhancing the H_2^- absorption by almost a factor of three. At longer wavelengths though, the update tends to decrease the absorption slightly (see Bell (1980) for a discussion on the various approximations in the two cases).

The update of the H_2^+ absorption has some effect at intermediate wavelengths and low temperatures, where the absorption is lowered by as much as 15%, and at high temperatures and short wavelengths where the absorption is increased by up to 35 % (see Fig. A.3). The update consists in treating the bf absorption fully quantum mechanical and including 423 bound rotational-vibrational states (Stancil 1994), as opposed to the semi-classical continuum of states used by Bates (1952). Expanding the wavelength interval downward, also brings us out in a region that would get undersampled with the old data.

I have not been able to find any newer calculations of absorption by the H+H quasi-molecule, so in Fig. A.4 I just present what has always been used. My largest

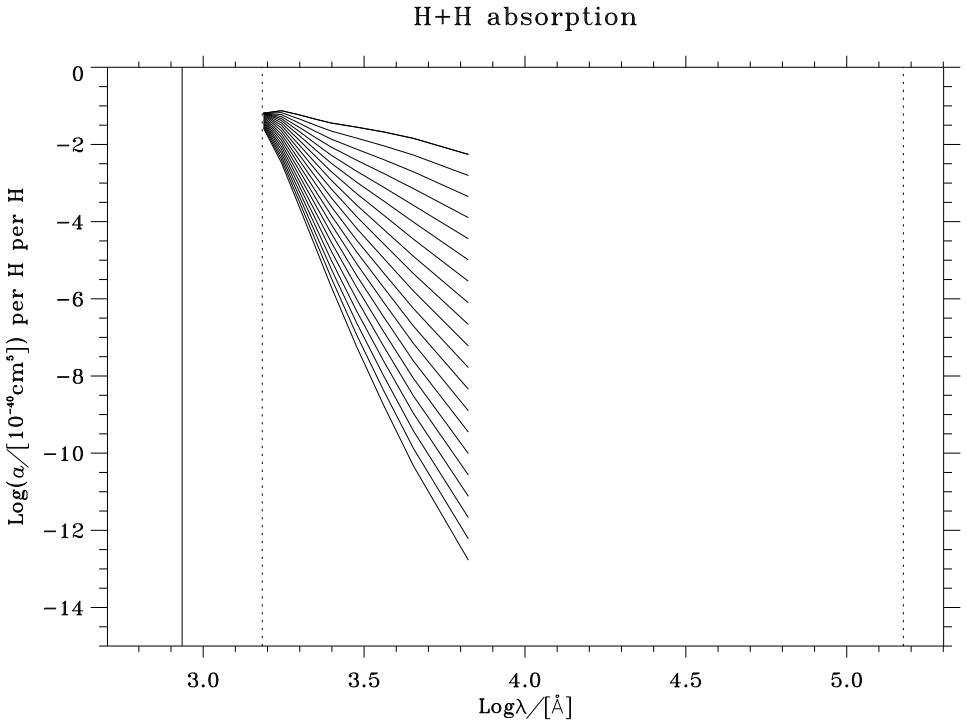

Fig. A.4: The absorption by the H+H quasi-molecule is unchanged but has been included here for comparison with the other sources of absorption. The curves are for $\Theta = 5040/T = 0.1 - 2.0$ with steps of 0.1, from top to bottom.

concern with this opacity source is the extrapolations involved. The original data (Doyle 1968) only cover $\lambda = 1\,540$–$6\,667$ Å and θ =0.5–2.0; the highest temperatures and shortest wavelengths, having the largest absorption are not covered.

The inclusion of continuous molecular opacities (see Fig. A.5) has hardly any effect for solar Rosseland mean opacities, as the abundances of these molecules are quite low (see Fig. A.9). But there is a small effect anyway, and it increases going to cooler stars. From Fig. A.9 we also see that the number densities of molecules decrease more slowly with temperature for lower $T_{\rm eff}$ and higher $g_{\rm surf}$. Where $\langle T \rangle = T_{\rm eff}$ for the respective stars, we observe more than a factor of ten in difference between η Boo and α Cen B.

And now to the metallic opacities. The next three figures (Fig. A.6 - A.8) present the absorption from metallic absorbers, 3-4 per plot for the same three temperatures as in Fig. 3.6–3.8. The wavelength axis is organized in the same way, with the three vertical lines, as in the previous figures in this appendix. Apart from these I have also plotted the Rosseland weighting function for the three temperatures (dashed curves on a commmon, but arbitrary scale), to give a feeling for the effect on the Rosseland opacity.

Fig. A.6 displays the absorption by neutral Al, Mg and Si and Mg in particular deserves a comment. The ground state absorption to the blue of 1621.5Å has a rather

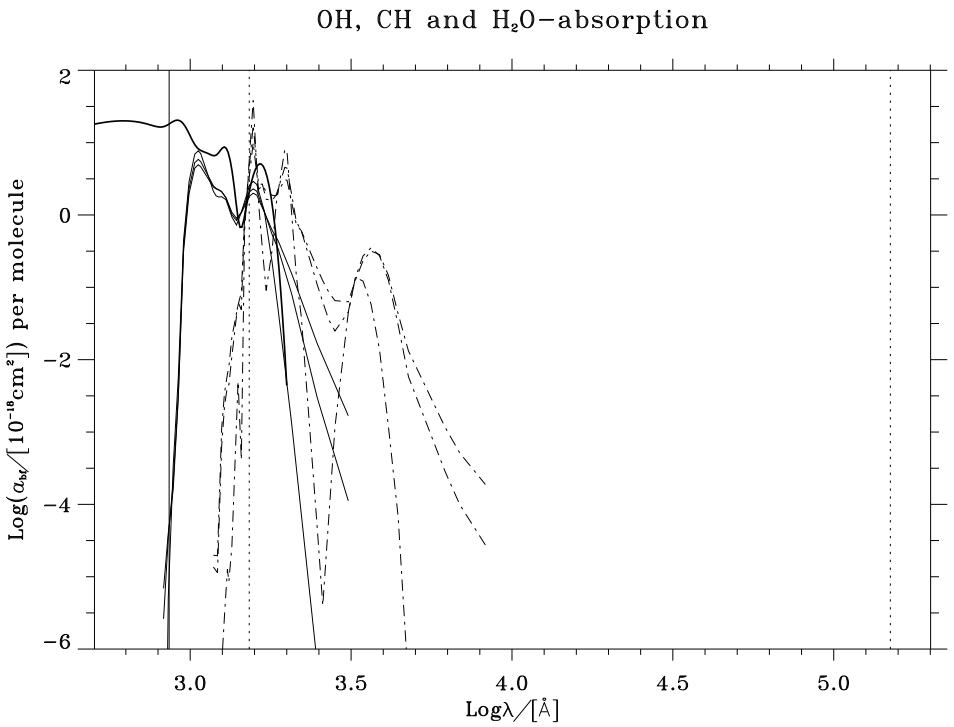

Fig. A.5: The continuous absorption by molecules is new to the program. Absorption by water vapour is shown by the thick solid line stopping at $\lambda \simeq 2\,000$Å(cf. Mat1, p. 47). The thin solid and the dot-dashed lines are the absorption by OH and CH-molecules respectively, for temperatures 1 000, 5 000 and 9 000 K (Kurucz et al. 1987). For peaks the upper-most curve is for the lowest temperature and vice versa for troughs.

peculiar behaviour which is the result of detailed quantum mechanical calculations (Mendoza & Zeippen 1987). In this article the authors state a fitting formula which is just about the most precise fitting formula I have ever seen for such a complicated function. Their calculations does in fact result in further resonances, much narrower and in between the resonances shown here, but by leaving out the appropriate terms in the fitting formula, these resonances can be discarded (because of my low wavelength resolution), without affecting the rest noticeable.

Also the absorption from the second excited state has a somewhat peculiar behaviour. The resonance at 3009Å is actually used in a truncated version for my calculations, again because of the wavelength resolution (100Å). The resonance is scaled down by a factor of 5.26 to give approximately the same Rosseland mean on the adopted wavelength mesh and with linear interpolation to the 12 times finer ODF wavelength mesh, as compared to the Rosseland mean of the resonance calculated on a mesh that fully resolves the peak.

The continuous part of this absorption (2059-3757Å) can be fitted nicely to a function of the form; $1 - \exp(x)$ for $x \leq 0$, which gives rise to the funny hump on

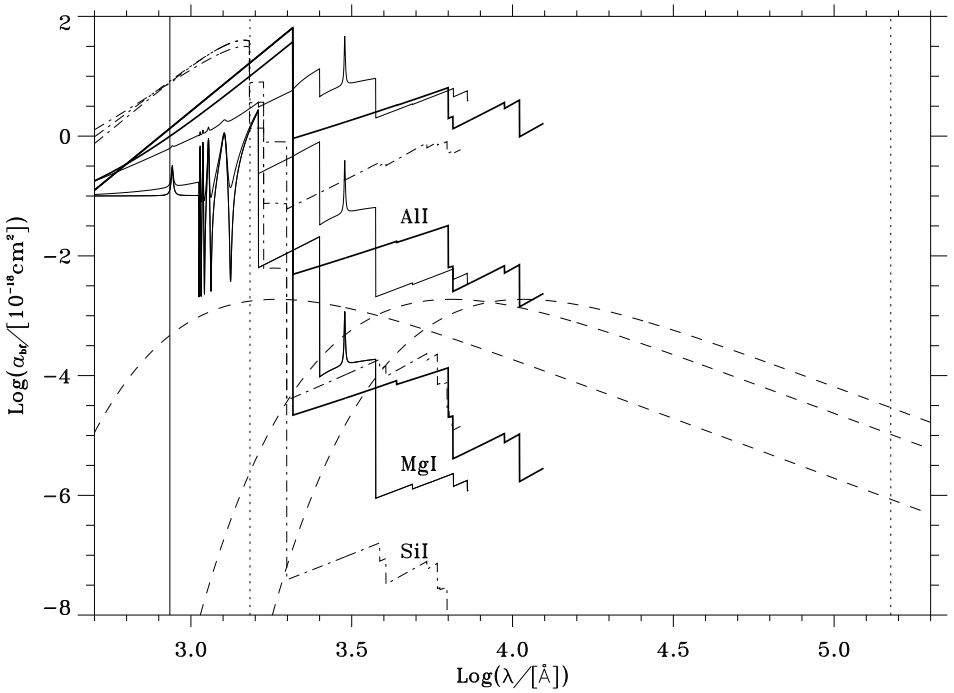

Fig. A.6: Bound-free opacity from atomic Al, Mg and Si per atom. The thick solid line is the AlI opacity from Mat1 p. 32-33, the thin solid line is MgI from Mat1 p. 29-30 using the ground state absorption by Mendoza & Zeippen (1987) and the dot-dashed line is the SiI opacity from Mat1 p. 33-34 supplied with tabulated values (Peach 1967) for $\lambda > 5839$Å. All the opacities are shown for three temperatures; 3 470, 5 820 and 20 310K, from bottom to top and I have also plotted the Rosseland weighting function for those temperatures, right to left.

the first excited state absorption at high temperatures. The rest of the absorption in this figure is just expressed as power series in λ with exponents ranging between 1.7 and 9.1.

Fig. A.7 displays the absorption by neutral He and Na and the Mg^+-ion. It is striking that the absorption by the second most abundant element, He, is so much weaker than any of the other opacity sources considered here. And this is of course the reason that the He abundance cannot be determined spectroscopically. Comparing with Fig. A.6, we also see that neutral Mg has a considerable larger absorption than its ion. All the absorption in this figure is expressed as power series in λ, with exponents ranging from 1 to 4, except for the ground state absorption by Na, which is fitted by a sum of three Gaussians. The Na absorption is clearly the largest in this plot, but it is efficiently counteracted by its low abundance (see Fig. A.9).

Fig. A.8 is admittedly a bit crowded, showing both the N, Ca, Ca^+ and Fe absorption. The Fe absorption is by far the most complex, including 26 states. In

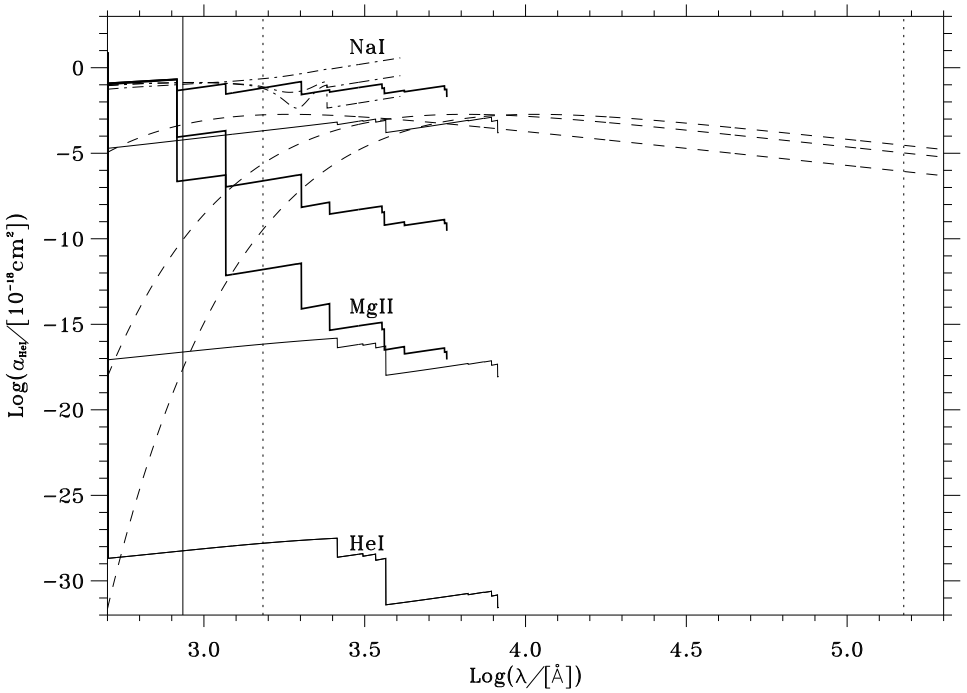

Fig. A.7: Bound-free opacity from atomic He, Na and the Mg^+ ion per particle. The thin solid line shows the HeI opacity from Mat1 p. 20-22, The thick solid line is the MgII opacity from Mat1 p. 31 and the dot-dashed line is the NaI opacity from Mat1 p. 28. Temperatures and Rosseland weighting functions (dashed lines) as for Fig. A.6.

Mat1 the FeI ground state absorption (Hansen et al. 1977, experimental) is presented for wavelengths between 1 150Å and up to the ionization threshold of 1 569Å. This, I have fitted to a sum of 7 Gaussians, clearly smoothing out a lot of the complicated structure. According to new theoretical work by Sawey & Berrington (1992) there is also substantial absorption at shorter wavelengths (their Fig. 3a), which I have fitted (loosely) to a Lorentzian plus a logistic curve to approach the constant level at short wavelengths. This Lorentzian is the peak at 1 050Å in Fig. A.8.

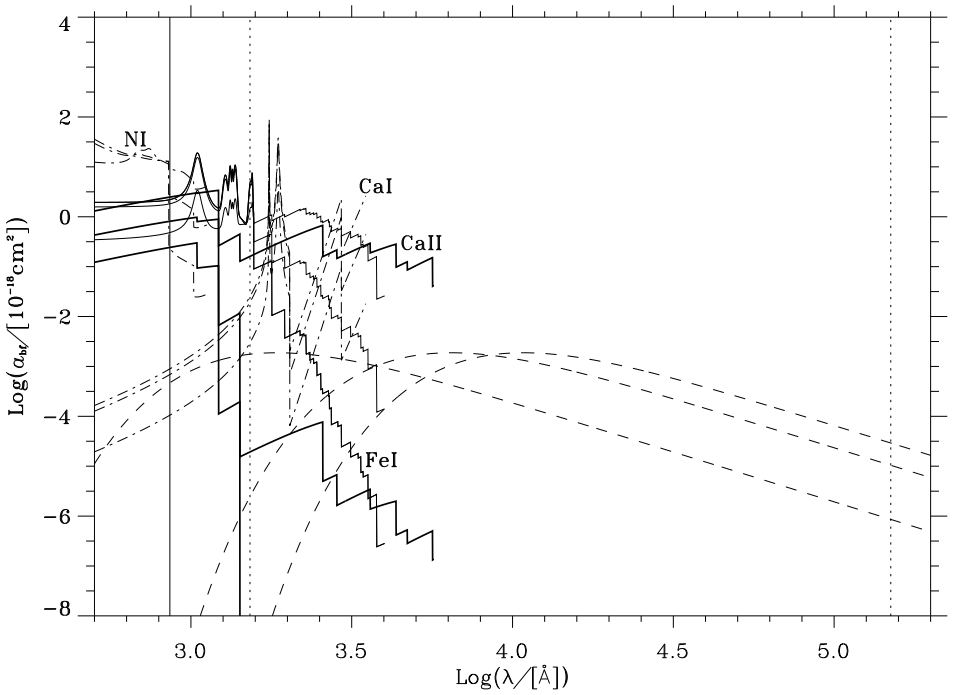

Fig. A.8: Bound-free opacity from atomic Fe, Ca, N and the Ca^+ ion per particle. The thin solid lines are for the FeI opacity (Mat1 p.40-41) and (Sawey & Berrington 1992) bluewards of 1 150Å. both the NI opacity (Mat1 p. 25-26) and the CaI opacity from Mat1 p. 38-39 are plotted with dot-dashed, and the thick solid line is the CaII ion opacity (Mat1 p. 39-40). Temperatures and Rosseland weighting functions (dashed lines) as for Fig. A.6.

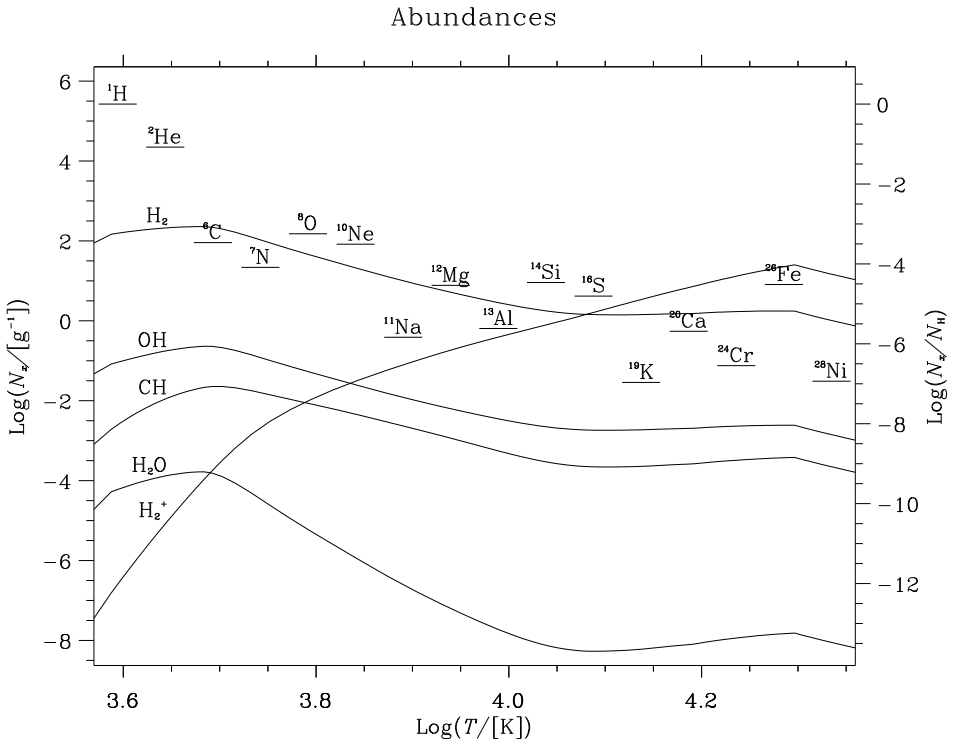

Fig. A.9: The number densities of H_2-, H_2^+-, OH-, CH-, and H_2O-molecules, as function of mean temperature in a typical snapshot of the Sun. In this plot I also show the abundances used for the heavier elements, to make it easier to judge the importance of the various opacity contributions. On the left abscissa I have the number of the respective particles per gram of stellar matter, and on the right axis the number densities are normalized to the numbers of hydrogen atoms.

Appendix B

Scattering by atomic hydrogen

The interaction of light with an electron in a bound state of a classical harmonic oscillator with *eigenfrequency* ω_0, can be expressed as

$$\sigma_{\text{Ray}} = \sigma_{\text{T}}\omega^4 \text{Re}[P(\omega)]^2, \tag{B.1}$$

$$a_{\text{line}} = \sigma_{\text{T}}\omega^4 \text{Im}[P(\omega)]^2, \tag{B.2}$$

where σ_{Ray} is the Rayleigh scattering (3.34) and a_{line} is the line absorption, due to a complex polarizability $P(\omega)$

$$P(\omega) = \frac{1}{\omega_0^2 - \omega^2 - 2i\gamma_{\text{cl}}\omega^2}, \tag{B.3}$$

where the energies or cyclic frequencies, ω should be expressed in units of Rydbergs, for the above formulas to work, and γ_{cl} is the classical damping constant due to radiation damping $\gamma_{\text{cl}} = \alpha^3\omega_0^2/6$ where α is the fine-structure constant. The Thompson scattering σ_{T} given by (3.34), is the cross-section for scattering by free electrons and also the limit of the atomic scattering cross-section, when $\omega \gg \omega_0$.

For $\omega \ll \omega_0$ we have $\sigma_{\text{Ray}} \propto (\omega/\omega_0)^4$ which is the part of the scattering actually called Rayleigh scattering. The ω_0 displays the fact that the bound electron resonates with the other allowed bound states in the atom. The semiclassical, or pseudo quantum mechanical, generalization is performed by introducing oscillator strengths

$$P_i(\omega) = \frac{\sqrt{f_i}}{\omega_i^2 - \omega^2 - 2i\gamma_i\omega^2}, \tag{B.4}$$

and using $\gamma_i = f_i\gamma_{\text{cl}}$. The index i enumerates the allowed bound states in the atom, and to get the total polarizability from resonating with all states, (B.4) should be summed over all states. The oscillator strengths f_i are defined as conversion factors between the classical results and the real world (experiments or quantum-mechanical calculations). Tables can be found in, say, Allen (1973), p. 70.

This pseudo-quantum-mechanical treatment in fact works surprisingly well, in comparisons with more sophisticated calculations (see Fig. B.2). Though the agreement gets worse near resonances, the behaviour is still correct, and the long and

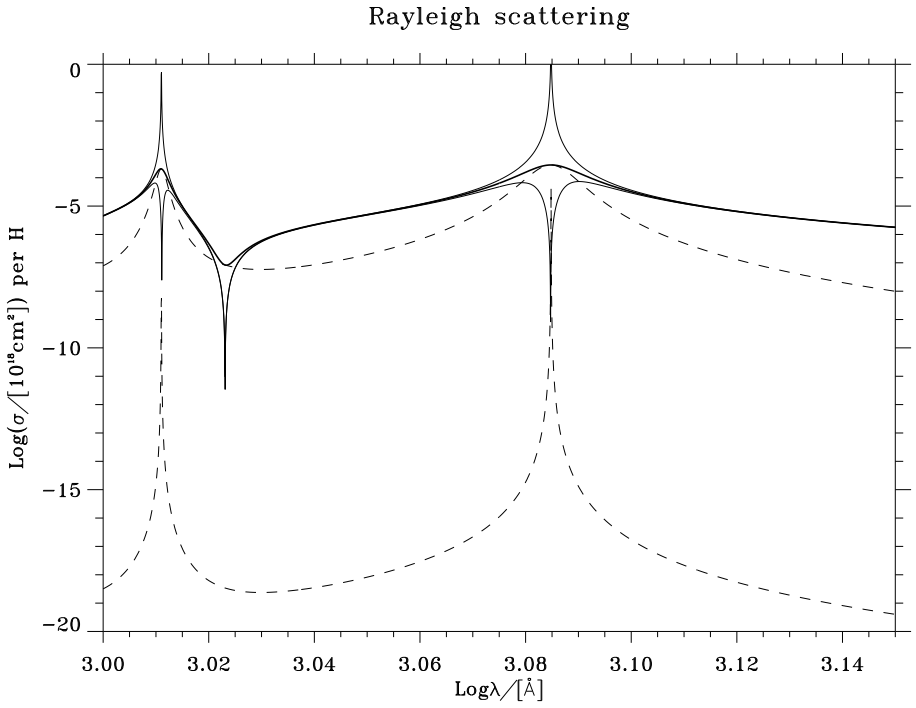

Fig. B.1: The effect of changing the damping constant, on the absorption and scattering cross-sections for atomic hydrogen around the first two Lyman lines, Lα (1216Å) and Lβ (1026Å). The solid lines are the scattering part and the dashed lines are the absorption part. The upper solid line and the lower dashed line corresponds to using γ_i for the damping constant, whereas the lower solid and the upper dashed correspond to using $5 \cdot 10^5 \gamma_i$. The thick solid curve is the sum of the latter scattering and absorption and also the form I adopt for the Rayleigh scattering by atomic hydrogen.

short wavelength limits are also correct. I would suggest Cox & Guili (1968; chapter 2.10d) for a more thorough discussion.

We can now write (B.1) as

$$\sigma_{\rm Ray} = \sigma_{\rm T}\omega^4 \sum_i f_i \frac{4\gamma_i\omega^2(\omega_0^2-\omega^2)}{[(\omega_i^2-\omega^2)^2+(2\gamma_i\omega^2)^2]^2} \tag{B.5}$$

$$a_{\rm line} = \sigma_{\rm T}\omega^4 \sum_i f_i \frac{(\omega_i^2-\omega^2)^2-(2\gamma_i\omega^2)^2}{[(\omega_i^2-\omega^2)^2+(2\gamma_i\omega^2)^2]^2}. \tag{B.6}$$

Again, (B.5) is the scattering due to the real part of the polarizability and (B.6) is the absorption stemming from the imaginary part.

The adopted damping constant, γ_i is not all that physical, as collisional broadening is not included. This would add a very complicated term in ϱ and T and easily increase the damping constant (or equivalently, the line width) by orders of magnitude.

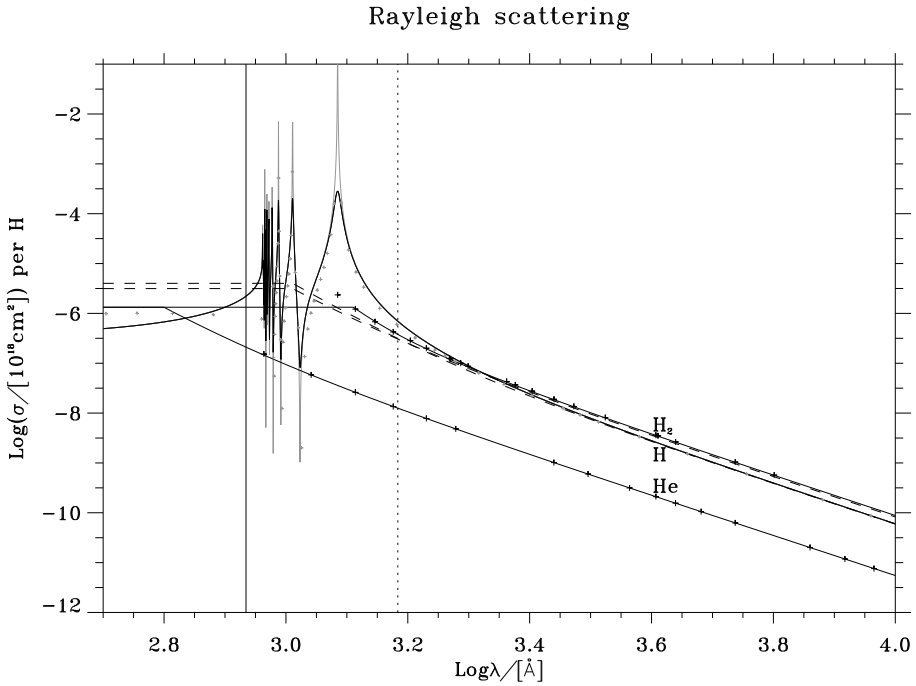

Fig. B.2: Comparison of the present and previous Rayleigh scattering contributions from H, H_2 and He. For H_2 and He, the presently used Rayleigh scattering is shown with solid lines and is evaluated using Eq. (3.35). The dashed lines show the old expressions for H and H_2 scattering by Gustafsson (1973). The crosses for He represents the calculations by Langhoff et al. (1974) and for H_2, the experimental results of Victor & Dalgarno (1969). For scattering by hydrogen I now use Eq. (B.5) (solid line), which is compared with the detailed quantum mechanical calculations of Gavrila (1967) (small crosses). Notice that the atomic and molecular scattering by hydrogen cross each other at about 2000Å.

Fortunately, the line width only alters the shape of (B.5) in the immediate vicinity of the line centre. Increasing the line width both broadens the resonance and shifts the weight from scattering to absorption in the line centre. The broader line has a smaller combined (scattering + absorption) amplitude in the line centre so the scattering part is in fact depressed in the line centre, making the scattering part a complicated and rapidly varying function of wavelength (*cf.* Fig. B.1 or B.2).

As the wavelength resolution in the continuous opacity calculation is limited (20-40 Å in the resonance region), it is not advisable to use such an rapidly changing function, so instead I use the sum $\sigma_{\rm Ray} + a_{\rm line}$ and a large damping constant; $5 \cdot 10^4 \gamma_i$ (see Fig. B.1), to suppress the very thin lines. There is no physical reasons for doing so, but it turns out to give features which can be resolved with the adopted wavelength grid. Without this enlarged damping constant, the lines rising a factor of 1000 above the "continuum" picked out with this prescription would contribute far too much to a mean opacity.

Appendix C

An IDL[1] interface to the averaged models

Convention for storing
Horizontally and Time Averaged Models of
Hydrodynamical simulations of stars

The mean models of stellar atmospheres, derived from hydrodynamical simulations carried out with the program by Åke Nordlund and Robert F. Stein (*e.g.* (Stein & Nordlund 1989; Nordlund & Stein 1990), have been stored to binary files, `'l2means.dat'` (the `'l'` standing for Lagrangian horizontal averages) or `'t2means.dat'` (where `'t'` stands for optical depth, τ-scale) in the following way:

The first line is in ASCII-format and contains `nz, nvar, g`, which is the number of z-points (I normally use `nz`=82), the number of stored variables (currently `nvar`=105) and `g` is the surface gravity. From UNIX it can be read by for example

```
head -1 l2means.dat,
      82      105      27395.9.
```

The surface gravity, as well as the effective temperature, can also be accessed from IDL

```
IDL> print, teff(), gsurf()
         5775.75        27395.9.
```

The `teff()` function calculates the $T_{\rm eff}$ from the time averaged total flux.

After this ASCII header the z-scale is stored in binary format; `nx*4` bytes, and then come all the data which are stored in a `nz*nvar*4` byte block. I would recommend to use my IDL-program, `mtdata`, for accessing the data. It assumes the file is called `'l2means.dat'` and uses the logical file unit number (LUN) 4. So being in a directory with a `'l2means.dat'`-file, you just type

```
IDL> Frad = mtdata('FRAD')
IDL> help, Frad
```

[1] IDL® is a registered trademark of Research Systems Inc., Boulder, Colorado, USA.

```
FRAD            FLOAT     = Array(82)
```

and you have the radiative flux at hand. The possible variable names are listed below. All of these, except the last two ($\langle F_{\rm rad}\rangle$ and z), can be extended with an `'up'` (lowercase!) or `'dn'` to get the average in the up- or down-flow only, *e.g.*

```
IDL> vort_dn = mtdata('Wdn')
```

to get the vorticity in the down-flow. A quantity at a specific timestep, say number 10, can be retrieved with the command

```
IDL> Frad = mdata(10,'FRAD')
IDL> help, Frad
FRAD            FLOAT     = Array(82),
```

And the whole timeseries can be retrieved by using

```
IDL> Frad = mdatat('FRAD')
IDL> help, Frad
FRAD            FLOAT     = Array(82,112)
```

if there are 112 timesteps in the file. There are 30 seconds between each timestep. When changing from one `'l2means.dat'`-file to another, just

```
IDL> close, 4
```

and change directory to where the other file is. The surface gravity can be found inside IDL by typing

```
IDL> nz = 0 & nvar = 0 & g = 0.0
IDL> point_LUN, 4, 0
IDL> readf, 4, nz, nvar, g
```

after the file has been opened with a previous `mtdata` call. With the `Frad` from above, the effective temperature can be found with

```
IDL> Teff = (Frad(0)/5.67051e-5)^.25
```

as $F = \sigma T_{\rm eff}^4$, and the z-scale is yours by typing

```
IDL> z = mtdata(-1)
```

All the horizontal averages are Lagrangian, *i.e.* performed on the same column density scale. First the column density

$$h(z_i) = \int_0^{z_i} \varrho(z_i)\mathrm{d}z_i$$

is calculated for the first timestep, lets call it h_0. The index i on the z's are just to remind us that z is a discrete array. For all the subsequent timesteps t, a new interpolated z_i-scale is calculated to have the same h-points by

$$z_{i,\rm new}(t) = h_t^{-1}(h_0(z_i))$$

All the variables are then, at each timestep, interpolated to these z-scales before summing up in the averaging. This Lagrangian averaging is performed to avoid

problems due to the excited p-modes: the averaging in this way does not smear out features and it is possible to obtain a fairly good average over a time shorter than one period. The files, though, have been averaged over the order of 10-20 periods.

The optical depth averages are evaluated on an equidistant $\log_{10}\tau$-scale, with `nz` points and ranging from -3 to 2. For each time step, I evaluate the iso-τ surfaces, interpolate the various variables onto these surfaces using cubic splines, and then average the variables on these iso-τ surfaces. These averages are also calculated for the up- and down-flows separately. The τ-averages comes in two versions: a Rosseland $\tau_{\rm Ross}$ average and a 5000 Å monochromatic τ_{5000}-average. The latter have filenames `'t2means.dat.5000'`.

The different pressures are written out explicitly to avoid confusion and $P_{\rm tot} = P_{\rm g} + P_{\rm turb}$. Also remember that $z = R - r$, meaning that z is pointed inward in the star. `FENT` is the Lagrangian part of the enthalpy flux, that is, a possible net mass flux has been removed. The same applies to `FKIN`, the kinetic energy flux. When calculating derivatives, I, among other things, use that

$$T\mathrm{d}S = \mathrm{d}U + P_{\rm g}\mathrm{d}V = \mathrm{d}\varepsilon - \frac{P_{\rm g}}{\varrho}\mathrm{d}\ln\varrho \qquad \Rightarrow \qquad \left(\frac{\partial\varepsilon}{\partial\ln\varrho}\right)_S = \frac{P_{\rm g}}{\varrho}.$$

The programs and data files are available upon requests (as long as the request is accompanied by a free cold draught beer :-)

Suggestions and questions are very welcome.

Good luck!

Regner Trampedach, March 18, 2000

$$
\begin{aligned}
\texttt{RHO} &= \langle\varrho\rangle = \bar{\varrho} \\
\texttt{E} &= \langle\varepsilon\rangle = \bar{\varepsilon} \\
\texttt{T} &= \langle T\rangle \\
\texttt{MT} &= \bar{T} = T(\bar{\varrho},\bar{\varepsilon}) \\
\texttt{PG} &= \langle P_{\rm g}\rangle \\
\texttt{MPG} &= \bar{P}_{\rm g} = P_{\rm g}(\bar{\varrho},\bar{\varepsilon}) \\
\texttt{CS} &= \langle c_{\rm s}\rangle = \left\langle\sqrt{\Gamma_1\frac{P_{\rm g}}{\varrho}}\right\rangle \\
\texttt{MCS} &= \bar{c}_{\rm s} = \sqrt{\bar{\Gamma}_1\frac{\bar{P}_{\rm g}}{\bar{\varrho}}} \\
\texttt{CP} &= \langle c_{P_{\rm g}}\rangle = \left\langle\left[1-\frac{P_{\rm g}}{\varrho}\left(\frac{\partial\ln\varrho}{\partial\varepsilon}\right)_{P_{\rm g}}\right]\left(\frac{\partial T}{\partial\varepsilon}\right)^{-1}_{P_{\rm g}}\right\rangle \\
\texttt{MCP} &= \bar{c}_{P_{\rm g}} = c_{P_{\rm g}}(\bar{\varrho},\bar{\varepsilon}) = \left[1-\frac{\bar{P}_{\rm g}}{\bar{\varrho}}\left(\frac{\partial\ln\varrho}{\partial\varepsilon}\right)_{P_{\rm g}}(\bar{\varrho},\bar{\varepsilon})\right]\left(\frac{\partial T}{\partial\varepsilon}\right)^{-1}_{P_{\rm g}}(\bar{\varrho},\bar{\varepsilon}) \\
\texttt{CV} &= \langle c_V\rangle = \left\langle\left(\frac{\partial T}{\partial\varepsilon}\right)^{-1}_{\varrho}\right\rangle \\
\texttt{MCV} &= \bar{c}_{\rm V} = c_{\rm V}(\bar{\varrho},\bar{\varepsilon}) = \left(\frac{\partial T}{\partial\varepsilon}\right)^{-1}_{\varrho}(\bar{\varrho},\bar{\varepsilon}) \\
\texttt{GAM1} &= \langle\Gamma_1\rangle = \left\langle\left(\frac{\partial\ln P_{\rm g}}{\partial\ln\varrho}\right)_{\varepsilon}+\frac{P_{\rm g}}{\varrho}\left(\frac{\partial\ln P_{\rm g}}{\partial\varepsilon}\right)_{\varrho}\right\rangle \\
\texttt{MGAM1} &= \bar{\Gamma}_1 = \Gamma_1(\bar{\varrho},\bar{\varepsilon}) = \left(\frac{\partial\ln P_{\rm g}}{\partial\ln\varrho}\right)_{\varepsilon}(\bar{\varrho},\bar{\varepsilon})+\frac{\bar{P}_{\rm g}}{\bar{\varrho}}\left(\frac{\partial\ln P_{\rm g}}{\partial\varepsilon}\right)_{\varrho}(\bar{\varrho},\bar{\varepsilon}) \\
\texttt{TAU} &= \langle\tau\rangle = \langle\int_{top}^{bottom}\kappa\,{\rm d}z\rangle \qquad \text{for horizontal mean} \\
\texttt{MTAU} &= \bar{\tau} = \tau(\bar{\varrho},\bar{\varepsilon}) = \int_{top}^{bottom}\kappa(\bar{\varrho},\bar{\varepsilon})\,{\rm d}z \qquad \text{for horizontal mean} \\
\texttt{Z} &= z/[{\rm Mm}] \qquad \text{for } \tau-\text{averages} \\
\texttt{DAD} &= \langle\nabla_{\rm ad}\rangle = \left\langle\frac{\Gamma_3-1}{\Gamma_1}\right\rangle, \qquad \Gamma_3-1 = \frac{P_{\rm g}}{\varrho}\left(\frac{\partial\ln P_{\rm g}}{\partial\varepsilon}\right)_{\varrho} \\
\texttt{MDAD} &= \bar{\nabla}_{\rm ad} = \nabla_{\rm ad}(\bar{\varrho},\bar{\varepsilon}) = \frac{\bar{\Gamma}_3-1}{\bar{\Gamma}_1}, \qquad \bar{\Gamma}_3-1 = \frac{\bar{P}_{\rm g}}{\bar{\varrho}}\left(\frac{\partial\ln P_{\rm g}}{\partial\varepsilon}\right)_{\varrho}(\bar{\varrho},\bar{\varepsilon}) \\
\texttt{DS} &= \langle\nabla_{\rm s}\rangle = \frac{\langle\partial\ln T/\partial z\rangle}{\langle\partial\ln P_{\rm g}/\partial z\rangle}-\langle\nabla_{\rm ad}\rangle \\
\texttt{MDS} &= \bar{\nabla}_{\rm s} = \nabla_{\rm s}(\bar{\varrho},\bar{\varepsilon}) = \frac{\partial\ln\bar{T}}{\partial\ln\bar{P}_{\rm g}}-\bar{\nabla}_{\rm ad} \\
\texttt{DSS} &= \langle\nabla_{\rm s}\rangle = \frac{\langle\partial S/\partial z\rangle}{\langle c_{P_{\rm g}}\partial\ln P_{\rm g}/\partial z\rangle}
\end{aligned}
$$

$$
\begin{aligned}
\texttt{MDSS} &= \bar{\nabla}_{\rm s} = \frac{1}{\bar{c}_{P_{\rm g}}} \frac{\partial \bar{S}}{\partial \ln \bar{P}_{\rm g}} \\
\texttt{S} &= \langle S \rangle \\
\texttt{MS} &= S(\bar{\varrho}, \bar{\varepsilon}) \\
\texttt{UR} &= \langle u_{\rm radial} \rangle = -\langle u_z \rangle \\
\texttt{UR2} &= \langle u^2_{\rm radial} \rangle = \langle u_z^2 \rangle \\
\texttt{W} &= \langle |\vec{\omega}| \rangle = \langle |\vec{\nabla} \times \vec{u}| \rangle \\
\texttt{PT} &= \langle P_{\rm turb} \rangle = \langle \varrho u_z^2 \rangle \\
\texttt{FENT} &= \langle F_H \rangle = \langle (\varepsilon \varrho + P_{\rm g}) u_r \rangle_{\rm L} = \langle (\varepsilon + P_{\rm g}/\varrho)(\varrho u_r - \langle \varrho u_r \rangle) \rangle \\
\texttt{FKIN} &= \langle F_{\rm kin} \rangle = \tfrac{1}{2} \langle \varrho u_r u^2 \rangle_{\rm L} = \tfrac{1}{2} \langle u^2 (\varrho u_r - \langle \varrho u_r \rangle) \rangle \\
\texttt{UH2} &= \langle u^2_{\rm horisontal} \rangle = \langle u_x^2 + u_y^2 \rangle \\
\texttt{PGAM} &= \langle \Gamma_1 P_{\rm g} \rangle \\
\texttt{FRAD} &= \langle F_{\rm rad} \rangle \\
\texttt{-1} &= \begin{cases} z/[{\rm Mm}] & \text{for horisontal mean} \\ \log \tau & \text{for } \tau\text{-averages.} \end{cases}
\end{aligned}
$$

Appendix D

Calibrating the mixing-length with 3D RHD simulations

To be submitted to Astronomy & Astrophysics

Appendix E

On using T-τ relations as outer boundary condition for stellar models

To be submitted to Astronomy & Astrophysics